

**LIQUID CRYSTAL ANCHORING CONTROL AND ITS APPLICATIONS IN
RESPONSIVE MATERIALS**

Yu Xia

A DISSERTATION

in

Material Science and Engineering

Presented to the Faculties of the University of Pennsylvania

in

Partial Fulfillment of the Requirements for the

Degree of Doctor of Philosophy

2016

Supervisor of Dissertation

Shu Yang, Professor, Materials Science and Engineering

Graduate Group Chairperson

Shu Yang, Professor, Materials Science and Engineering

Dissertation Committee

Russell J. Composto, Materials Science and Engineering

Randall D. Kamien, Physics and Astronomy

Kathleen J. Stebe, Chemical and Biomolecular Engineering

ACKNOWLEDGMENT

A PhD dissertation is a long and tough journey, and I could not come this far without the support and help from the people surrounding me. I would like to sincerely express my appreciation to all of my professors, colleagues, friends, collaborators and family, without who I could not have any accomplishment.

Foremost, I would like to especially thank for the association and supervision from my advisor, Professor Shu Yang. She has devoted much of her time and effort in the past few years to supervise me in science, and my writing and presentation skills. I'm sincerely grateful for the knowledge she shared with me, and the technical skills and scientific thinking she advised me during my dissertation. I also appreciate her patience and continuous encouragement when I was experiencing difficulties and failures in my researches. I truly believe the invaluable advice I received will continue to benefit me in the future of my career.

I also want to express my gratitude and appreciation to my thesis committee, Professor Russell Composto of the Department of Materials Science and Engineering, Professor Randall Kamien of the Department of Physics and Astronomy, and Professor Kathleen Stebe of the Department of Chemical and Biomolecular Engineering, for their supports and valuable suggestions for my researches in the past years.

I would like to appreciate the assistants and creative inputs from all of my collaborators, including Professor Nader Engheta, Professor Jan van der Spiegel, Dr. Milin Zhang, and Hongjie Zhu in the Department of Electrical and Systems Engineering, Professor Jenny Sabin and Andrew Lucia in the Department of Architecture, Art, and Planning at Cornell University, Professor Russell Composto and Dr. Robert Ferrier in the

Department of Materials Science and Engineering, Professor Randall Kamien, Dr. Daniel Beller, Dr. Daniel Sussman, Dr. Maxim Lavrentovich, Dr. Toen Castle, Dr. Hillel Aharoni, Zoey Davidson, Wei-Shao Wei and Dr. Ye Xu in the Department of Physics and Astronomy, Professor Kathleen Stebe, Lisa Tran, Iris Liu, Yimin Luo and Nate Bade in the Department of Chemical and Biomolecular Engineering, Professor Kaori Ihida-Stansbury and Mithil Chokshi in the Department of Pathology and Laboratory Medicine, and Professor Rudolf Zentel and Dr. Eva-Kristina Fleischmann at the Johannes Gutenberg-Universität Mainz.

I would like to thank all the Yang group members, past and present, for their warm and kind help through my dissertation, including Dr. Francesca Serra, Dr. Mohamed Amine Gharbi, Dr. Chi-mon Chen, Dr. Elaine Lee, Dr. Yigil Cho, Dr. Younghyun Cho, Dr. Dengteng Ge, Prof. Xiaomin Yang, Gerardo Cedillo, Minsik Jun, Dr. Apiradee Honglawan, Euiyeon Jung, Hye-Na Kim, Dr. Su Yeon Lee, Dr. Jie Li, Zhiwei Liao, Huseyin Kaya, Dr. Hyesung Cho, Dr. Yudi Rahmawan, Luke Shi, Chenbo Wang, Gaoxiang Wu, Dr. Lebo Xu, Professor Lili Yang, Professor Youfa Zhang, and Yongwei Zheng. I would like to especially thank Dr. Francesca Serra and Dr. Mohamed Amine Gharbi for sharing their knowledge in liquid crystal physics.

I would like to express my appreciation to Dr. Gerald Lopez, Dr. Jamie Ford, Dr. Matthew Brukman, Steve Szewczyk, Kyle Keenan, Hiromichi Yamamoto, and Eric Johnston for training me on various nanofabrication and characterization instruments and helpful discussions of these techniques. I would also like to thank Patricia Overend, Irene Clements, Vicky Lee, Raymond Hsiao, and Enrique Vargas for making my life easier in the department.

Finally, I want to dedicate my thesis to my parents Yixin Xia and Zhizhen Lin, my parents-in-law Jian Wang and Qiong Zheng, my wife Wenshan Wang, and my lovely daughter Emily Xia, for their unconditional love and support. I especially want to express sincere gratitude and love to my wife Wenshan, who gave up her promising career in China, crossed the continent, and started a new life with me. I'm truly grateful for her sacrifice and assistance, without which this dissertation could not have been possible.

ABSTRACT

LIQUID CRYSTAL ANCHORING CONTROL AND ITS APPLICATIONS IN RESPONSIVE MATERIALS

Yu Xia

Shu Yang

Liquid crystals (LCs), owing to their anisotropy in molecular ordering, are of interests not only in the display industry, but also in the soft matter community, e.g., to direct colloidal assembly and phase separation of surfactants, and to actuate two-dimensional (2D) sheets into three-dimension (3D). The functionality and performance of LC materials extensively rely on the molecular ordering and alignment of LCs, which are dictated by LC anchoring at various boundaries. Therefore, this thesis focuses on the study of LC anchoring from both small molecule LCs and liquid crystal monomers (LCMs), which in turn guides my design of surface topography and surface chemistry to control formation of uniform LC defect structures over cm^2 samples under complex boundary conditions. The ability to precisely embed defect structures in a LC material also allows me to exploit the responsiveness of LCs to create actuators and scaffolds to (dis)assemble nano- and micro-objects. Specifically, by exploiting the bulk disclinations formed in the nematic phase of 4-octyl-4'-cyanobiphenyl (8CB) surrounding the micropillar arrays, we demonstrate (dis)assembly of gold nano-rods (AuNRs) for dynamic tuning of surface plasmon resonance (SPR). Due to the highly temperature-sensitive elastic anisotropy of 8CB, the bulk disclinations and consequently the AuNR assemblies and SPR properties can be altered reversibly by heating and cooling the LC system. Then we design and synthesize a new type of nematic LCMs with a very large

nematic window. Therefore, they can be faithfully aligned at various boundary conditions, analogous to that of small molecule LCs. After crosslinking LCMs into liquid crystal polymers (LCPs), we are able to study the LC assembly, director field, and topological defects using scanning electronic microscopy (SEM) at the 100 nm resolution. We then turn our attention to direct LCM alignment through controlling of surface chemistry and topography. We demonstrate the essential role of surface chemistry in the fabrication of liquid crystal elastomer (LCE) micropillar arrays during soft lithography. A monodomain LCM alignment is achieved in a poly(2-hydroxyethyl methacrylate) coated polydimethylsiloxane (PDMS) mold. After crosslinking, the resultant LCE micropillars display a large radial strain (~30%) when heated across the nematic-isotropic phase transition temperature (T_{NI}). The understanding of surface alignment in LCMs is then transferred to LCEs with embedded topological defects. On micron-sized one-dimensional channels with planar surface chemistry, LCMs can be faithfully oriented along the local channel direction. After crosslinking, the 2D LCE sheets show pre-programmed shape transformation to complex 3D structures through bending and stretching of local directors when heated above T_{NI} . Last, we control LC alignment and defect formation on a flat surface simply by using chemical patterns. Planar anchored SU8 is photopatterned on homoerotically anchored dimethyloctadecyl[3-(trimethoxysilyl)propyl] ammonium chloride (DMOAP) coated glass. By exploiting the pattern geometry, thus, boundary conditions, in combination with anisotropy of LC elasticity, we show that LC orientation can be precisely controlled over a large area and various types of topological defects are generated. Such defect structures can be further used to trap micro- and nanoparticles.

TABLE OF CONTENTS

ABSTRACT	v
LIST OF TABLES	xi
LIST OF FIGURES	xii
CHAPTER 1: Introduction of Liquid Crystals and Liquid Crystal Polymers ..	1
1.1 Liquid Crystals.....	1
1.1.1 History of Liquid Crystals.....	1
1.1.2 Types of Liquid Crystals and Liquid Crystal Phases	2
1.2 Physical properties of liquid crystals	4
1.2.1 Anisotropy.....	4
1.2.2 Elastic distortion and elastic energy	4
1.2.3 Topological defects and core energy.....	6
1.2.4 Surface anchoring and surface anchoring energy.....	7
1.3 Anchoring control in nematic liquid crystals	10
1.3.1 Surface chemistry.....	10
1.3.2 Topology and topography.....	13
1.4 Anchoring control for nematic liquid crystal monomers/polymers	16
1.4.1 Rubbing	16
1.4.2 Mechanical stretching or shearing.....	17
1.4.3 Electric and magnetic fields.....	18
1.4.4 Photoalignment.....	19
1.5 Liquid crystal polymers.....	20
1.5.1 Types of liquid crystal polymer networks.....	20
1.5.2 Stimuli responsiveness of liquid crystal polymers	24
1.6 Thesis outline	28
1.7 References	32
CHAPTER 2: Fine Golden Rings: Tunable Surface Plasmon Resonance From Assembled Nanorods in Topological Defects of Liquid Crystals.....	38
2.1 Introduction.....	38
2.2 Experimental methods.....	40
2.2.1 Surface functionalization of gold nanorods with polystyrene.....	40
2.2.2 Micropillar fabrication.....	41
2.2.3 Substrate functionalization	41

2.2.4 Assembly of PS-AuNRs in LCs	42
2.2.5 Characterization	42
2.3 Optical properties of gold nanorods	42
2.4 Control of liquid crystal surface anchoring	43
2.5 Optical response of AuNRs	47
2.6 Conclusions	54
2.7 Contributions	55
2.8 References	56
CHAPTER 3: Direct Mapping of Local Director Field of Nematic Liquid Crystals at the Nanoscale.....	58
3.1 Introduction.....	58
3.2 Experimental methods.....	59
3.2.1 Materials	59
3.2.2 Synthesis of Liquid Crystal Monomers	60
3.2.3 Preparation of liquid crystal monomer solutions.....	63
3.2.4 Fabrication of patterned substrates	63
3.2.5 Preparation of substrates with desired LC anchoring.....	63
3.2.6 Liquid crystal cell preparation	65
3.2.7 UV Crosslinking	65
3.2.8 Characterization	66
3.2.9 Measurement of refractive index and birefringence	66
3.3 Design of stable nematic liquid crystal	67
3.4 Liquid crystal anchoring study	75
3.5 Direct mapping of liquid crystal local direct field.....	78
3.6 Estimation of the elastic constants of liquid crystal monomers	81
3.7 Direct mapping of liquid crystal defect structures	85
3.8 Conclusions	89
3.9 Contributions	90
3.10 References	90
CHAPTER 4: Better Actuation Through Chemistry: Using Surface Coatings to Create Uniform Director Fields in Nematic Liquid Crystal Elastomers ...	94
4.1 Introduction.....	94

4.2. Experiment methods	97
4.2.1 Materials	97
4.2.2 Preparation of PDMS molds	97
4.2.3 Preparation of PDMS molds with different surface chemistry	97
4.2.4 Preparation of DMOAP coated glass substrates	97
4.2.5 Preparation of 5CB in the PDMS mold	98
4.2.6 Fabrication of LCM4 pillars	98
4.2.7 Polarized optical microscopy	99
4.2.8 Water contact angle measurement.....	99
4.2.9 Landau-de Gennes numerical modeling.....	99
4.3 Landau-de Gennes numerical modeling	99
4.4 Control of liquid crystal surface anchoring	102
4.5 Actuation of cross-linked LCEs	107
4.6 Conclusions	110
4.7 Contributions	111
4.8 References	111
CHAPTER 5: Pre-programmed Folding of a 2D Nematic Liquid Crystal Elastomer Sheet into 3D by Directing Liquid Crystal Alignment in 1D Micro- channels	114
5.1 Introduction.....	114
5.2 Experimental methods.....	118
5.2.1 Materials	118
5.2.2 Characterization	118
5.2.3 Fabrication of 1D channel masters.....	118
5.2.4 Replica molding of epoxy alignment patterns.....	119
5.2.5 Preparation of DMOAP coated glass substrates.....	119
5.2.6 Preparation of liquid crystal cells.....	119
5.2.7 Preparation of NLCE sheets.....	120
5.2.8 Characterization of the NLCE sheets	120
5.3 Fabrication of patterned 1D channels	120
5.4 LC anchoring study	124
5.5 Folding of NLCE 2D Sheets	125
5.6 Conclusions.....	129
5.7 Contributions	131
5.8 References	131

CHAPTER 6: Alignment of Nematic Liquid Crystals on Chemically Patterned Surfaces: Precise Design of Topological Defects 135

6.1 Introduction..... 135

6.2 Experimental methods..... 139

 6.2.1 Materials. 139

 6.2.2 Characterization. 139

 6.2.3 Micro-contact printing of SAMs..... 140

 6.2.4 Photo-patterning of SU8 layer. 140

 6.2.5 DMOAP treatment 140

 6.2.6 Water contact angle measurement..... 141

 6.2.7 Preparation of liquid crystal cells 141

 6.2.8 Assembly of colloids with liquid crystals 141

6.3 Preparation of chemically patterned surfaces 142

6.4 LC anchoring study on chemical patterns 145

6.5 Trapping microparticles within LC topological defects 153

6.6 Conclusions 154

6.7 Contributions 155

6.8 References 156

CHAPTER 7: Summary and Outlook..... 159

7.1 Summary 159

 7.1.1 Control of molecular alignment and defect structures of small molecule liquid crystals for direct self-assembly of responsive materials 159

 7.1.2 Control of molecular alignment and defect structures of liquid crystal monomers for nano-scale imaging and actuation 160

7.2 Outlook 162

7.3 References 167

LIST OF TABLES

Table (1-1) Dependence of LC orientation on surface tensions.....	10
--	----

LIST OF FIGURES

Figure 1.1 Schematic representation of different LC phases. (a) Isotropic. (b) Nematic. (c) Smectic. (d) Cholesteric. The arrows indicate the local LC director.	3
Figure 1.2 Chemical structures of two commonly used LCs. (a) 5CB. (b) 8CB.	3
Figure 1.3 Schematic illustration of elastic distortions in a nematic LC. (a) Splay. (b) Twist. (c) Bend. Reproduced by permission from literature ⁷	5
Figure 1.4 Schematic of topological defects in a nematic LC. (a-d) Point defects: (a) +1, (b) -1, (c) $-1/2$, (d) $+1/2$. (e) $-1/2$ line defect. The blue lines represent LC director and the red dots and lines represent LC defects.	7
Figure 1.5 Schematic illustration of LC anchoring on a surface. (a) Homeotropic. (b) Planar. (c) Tilted. (d) Representation of LC anchoring on a surface determined by an azimuthal angle ϕ and a zenithal angle θ	9
Figure 1.6 Schematic illustration of LCs on a chemically patterned surface. The blue region indicates homeotropic anchoring for LC, and the green area is random planar anchoring.	13
Figure 1.7 Schematic of different types of liquid crystal polymers. (a) Main-chain LCP. (b) Side-chain LCP. (c) Mixed type. The purple rods represent LC mesogens.	21
Figure 1.8 Illustration of different responsive LCPs. (a) Thermo-sensitive LCP. A rectangular shaped nematic LCP changes dimensions from $x \times y$ to $x' \times y'$, when heating above nematic-isotropic phase transition temperature. (b) Light-sensitive LCP. Left panel shows the isomerization reaction of azobenzene, and right panel demonstrates the shape transformation of a thin LCP membrane under light irradiation. (c) Electro-sensitive LCP. The schematic demonstrates the shape transformation of a LCP film when switching the electric field.	23
Figure 2.1 (a) Schematic detailing the functionalization of AuNRs with polystyrene brushes. (b-c) Extinction spectra of (b) AuNRs in water and (b) PS-AuNRs in chloroform. (d) SEM image of PS-AuNRs.	43
Figure 2.2 (a) Schematic of the side view of the temperature sensitive disclination ring confined to a micropillar. The red solid line and blue dotted line represent the LC director field at high and low temperatures, respectively. The red and blue crosses illustrate the position of the defect at high and low temperatures, respectively. (b-f) Bright field images of 8CB in homeotropic pillar arrays in the nematic phase, at temperatures indicated at the top right corner of each image. The circles surrounding the micropillars originate from light scattering by LC bulk disclinations. Scale bar applies to all figures.	45

Figure 2.3 POM images of 8CB over homeotropic anchoring epoxy pillar arrays at various temperatures. Pillar dimensions are diameter = 10 μm , spacing = 10 μm , and aspect ratio (height/diameter) = 1.3. The temperature is indicated in the top right corner of each image. Scale bar applies to all figures. 46

Figure 2.4 Illustration of LC cell. (a) Schematic of the substrate functionalization; (b) Chemical structure and phase transition temperature of 8CB. 47

Figure 2.5 POM images of functionalized gold nanorods in 8CB over homeotropic anchoring epoxy pillar arrays at (a) 35°C (nematic) and (b) 30°C (smectic). White arrow indicates the assembly of gold nanorods. Pillar dimensions are diameter = 10 μm , spacing = 10 μm , and aspect ratio (height/diameter) = 1.3. Scale bar applies to all figures. (c) Extinction spectra of gold nanorods in 8CB over homeotropic anchoring epoxy pillars. The extinction is offset for clarity. Red, blue, and black colors indicate isotropic, nematic, and smectic phase, respectively. (d) Schematic of the gold nanorods assembled side-by-side (top) and end-to-end within the LC defect core. 48

Figure 2.6 The defect radius of 8CB in the nematic phase and TLSPR wavelength of the PS-AuNRs over epoxy pillars as a function of temperature. 51

Figure 2.7 POM images of functionalized gold nanorods in 8CB over planar anchoring epoxy pillar arrays at (a) 35°C (nematic) and (b) 30°C (smectic). Pillar dimensions are diameter = 10 μm , spacing = 10 μm , and aspect ratio (height/diameter) = 1.3. Scale bar applies to all figures. (c) Extinction spectra of gold nanorods in 8CB over planar anchoring epoxy pillars. The extinction is offset for clarity. Red, blue, and black colors indicate isotropic, nematic, and smectic phase, respectively. (d) The transverse (T) and longitudinal (L) localized surface plasmonic resonance peak (LSPR) position as a function of temperature for both homeotropic and planar cells. 52

Figure 2.8 (a) Extinction spectra of PS-AuNRs in 8CB sandwiched between two glass slides with homeotropic anchoring. The extinction is offset for clarity. Red, blue, and black colors indicate isotropic, nematic, and smectic phase, respectively. (b-e) POM images of PS-AuNRs in 8CB in a homeotropic flat cell; the sample is transitioning from the nematic to the smectic phase from b to e. 54

Figure 3.1 POM images of LCM_AZO [4-ethoxy-4'-(6-acryloyloxyhexyloxy) azobenzene] and RM257 on various patterned epoxy substrates coated with different surface chemistry. (A) LCM_AZO in PVA coated square array of pores. (B) LCM_AZO between PVA coated square array of pillars. (C) LCM_AZO in DMOAP coated square array of pores. (D) LCM_AZO between DMOAP coated square array of pillars. (E) RM257 in PVA coated square array of pores. (F) RM257 between PVA coated square array of pillars. (G) RM257 in DMOAP coated square array of pores. (H) RM257 between DMOAP coated square array of pillars. Pores in A, C, E, and G: diameter: 10 μm , pitch: 15 μm , depth: 20 μm . Pillar arrays in B, D, F, and H: diameter: 10 μm , pitch: 20 μm , height: 19 μm . Samples were cooled slowly (1 $^{\circ}\text{C}/\text{min}$) from isotropic phase (100

°C for LCM_AZO and 130 °C for RM257) to nematic phase (94 °C for LCM_AZO and 125 °C for RM257). Scale bar applied to all figures: 20 μm. 68

Figure 3.2 Schematic illustrations of (A) the chemical structures of various liquid crystal monomers, LCM_X1, LCM_X2 and LCM_X3 and (B) random intermolecular dipole-dipole interactions between nitro and carbonyl groups. Different colors represent different functional groups: red for nitro; blue for carbonyl..... 70

Figure 3.3 Schematic illustrations of the synthesis of the nematic liquid crystal monomers..... 71

Figure 3.4 ¹H-NMR spectrum of the liquid crystal monomers (A) LCM_X1; (B) LCM_X2; (C) LCM_X3..... 73

Figure 3.5 DSC curves of the LCMs. (A) LCM_X1. A nematic phase from 6.5 °C to 132 °C (heating) and 136 °C to 15 °C (cooling), respectively, was observed. (B) LCM_X2. A nematic phase was only observed upon cooling from 101 °C to 57 °C*. (C) LCM_X3. A nematic phase was shown from -9 °C to 72 °C (heating) and 77 °C to -4 °C (cooling), respectively. 74

Figure 3.6 POM and BF images of 5CB and LCM_X1. (A-C): POM and BF images of 5CB (top panels) and LCM_X1 (bottom panels) in (A) porous membranes (diameter: 10 μm, pitch: 15 μm, depth: 20 μm), (B) pillar arrays (diameter: 10 μm, pitch: 20 μm, height: 19 μm), and (C) square channels (width: 10 μm, pitch: 40 μm, depth: 20 μm) with homeotropic anchoring imposed at all surfaces. Insets in A: BF image of LCs in pores where the dark dots at the center showing possible defects; Insets in B: BF image with black circles showing possible bulk line defects circumscribing the pillars; Insets in C: BF image of a single ridge where the gray color indicates a distorted director field but no defect; (D-E) POM images of the schlieren texture of LCM_X1 before (D) and after (E) UV curing. The nearly identical nematic schlieren textures indicate that the LC director field is well-maintained during polymerization. Scale bars, 20 μm applicable to all panels. 76

Figure 3.7 POM images of various LCMs on patterned substrates with homeotropic anchoring at the boundaries. (A) LCM_X2 in the square array of pores. (B) LCM_X2 between the square array of pillars. (C) LCM_X3 in the square array of pores. Scale bars: 40μm. Insets: POM images with higher magnification. Scale bars: 10μm. Pores in A&C: diameter: 10 μm, pitch: 15 μm, depth: 20 μm. Pillar arrays in (B): diameter: 10 μm, pitch: 20 μm, height: 19 μm. Samples were fast cooled (~20 °C/min) from isotropic phase (LCM_X2, 110 °C; LCM_X3, 85 °C) to nematic phase (LCM_X2, 90 °C; LCM_X3, 70 °C). 77

Figure 3.8 UV-Vis spectra of LCM_X1 before and after UV curing. 79

Figure 3.9 SEM images show the fracture structure of LCP after polymerization in a 1-D microchannel (A), in a pore (B), and between two pillars (C). Escaping director field of

LC can be observed from the orientation of the fracture structures in all three structures; The red dotted lines in A-C represent local director field of LCM mirrored in the other half of images. Scale bars: A: 5 μm ; B and C: 2 μm 80

Figure 3.10 Director angle as a function of the radial coordinate r . The points are calculated from the escape configuration shown in the inset (scale bar, 5 μm). The line is calculated from Eq. (3-1). 82

Figure 3.11 SEM image of a hybrid wedge cell (left panel), with highlighted angles at the planar and homeotropic surface, and the corresponding measurements of the planar anchoring extrapolation length (right panel) taken from the cell at different cell thicknesses (indicated next to each data point, in microns). Scale bar in SEM image, 10 μm 84

Figure 3.12 SEM images of silica colloids suspended in LCP where either a point defect (A) or a line defect (B) was formed to screen the charge of the colloid. Insets: POM images of point (A) and line (B) defects circumscribing silica colloids. The director field of the LC is represented by the red dotted line and the red crosses show the position of defects. Scale bars: 2 μm 86

Figure 3.13 Metastable configurations. (A) POM image of silica colloids suspended in LCM resulting in coexistence of homeotropic and planar-like regions, where the metastable planar regions (blue color) are stabilized by silica colloids. (B, C, E) SEM images characterizing the local director field at different positions in (A) as indicated by the red dotted squares. (B) SEM image taken at the boundary between homeotropic and planar regions of LC, where a bright line in the middle of the image is shown, indicating the presence of a disclination line defect. (C) SEM image of a silica colloid sitting at the boundary. The bright line in the image shows a line defect in the bulk of LC that merged with the Saturn ring defect encircling the colloid. The silica colloid was trapped in the middle of the LC cell, and slightly sank downwards. (D) SEM image of fiber-like structure that shows a bulk disclination line pinned to the bottom surface, as indicated by the bending white line. (E) SEM image of local LC director field inside an escaped region. Horizontally aligned fiber-like fractures indicating planar alignment of LC director field were found in the middle of the image, where the bending fiber-like fractures from top and bottom boundaries merged. Scale bars: A: 20 μm ; B-E: 3 μm 88

Figure 3.14 Escaping behavior of LCs in a planar-like region. SEM images of LCP inside a planar region in a homeotropic LC cell. (A) The fracture structure shows stabilization of disclination lines with silica colloids sitting at the two ends of the planar region, and the escaping behavior of LC director from right to left. (B-C) A close look at the director field surrounding the colloid. Scale bars: 5 μm 89

Figure 4.1 Landau-de Gennes numerical modeling of 5CB in a PDMS mold with (a) homeotropic anchoring and (b) planar anchoring. 102

- Figure 4.2** (a) Schematic illustrations of the preparation of the PDMS molds with different surface chemistry and the fabrication of LCE pillar array. Pillar dimensions: diameter, 10 μm , pitch (center-to-center distance), 20 μm and height, 40 μm . (b) Chemical structures of LC systems used in the experiments. 103
- Figure 4.3** Average water contact angles on PHEMA coated PDMS exposed to different UV dosages. 104
- Figure 4.4** POM images of 5CB (a) and LCM4 (b) in a PHEMA porous mold with pore diameter 10 μm , pitch 15 μm , and depth 20 μm . Vertical alignments of LC molecules were observed in both LC systems. Scale bar: 20 μm 105
- Figure 4.5** (a) Schematic of the LC disclination line in a mold with homeotropic anchoring. The red dotted line indicates the escape of the LC director, while the red shaded region indicates the width of the escaping configuration, where the director field is uniformly vertical. (b-c) POM images of (b) 5CB and (c) LCM4 under homeotropic anchoring in the PDMS mold. Inset in (b): LC escaping domain indicated by the red circle under cross polarizers when observing the sample from the top under POM. (d) Schematic of the disclination line of 5CB in a PDMS mold treated with planar anchoring chemistry. (e-f) POM images of (e) 5CB and (f) LCM4 in a planar-anchored PDMS mold. 106
- Figure 4.6** POM image showing polydomain alignment of LCM4 in a non-treated PDMS porous mold. Scale bar: 20 μm 106
- Figure 4.7** (a-b) Cross-sectional views of POM images of LCM4 pillars after UV curing viewed at (a) 45° and (b) 0° polarization angles. (c-d) Cross-sectional views of BF images of LCM4 pillars at 50°C (c) and 110°C (d). (e) Top-view BF image of LCM4 pillars through a heating and cooling cycle. Blue and Red arrows in (c-e) indicate the position of pillars for measurement of diameter at 50 °C and 110 °C, respectively. Length of arrow: blue-8.6 μm , red-11.1 μm . Scale bar: 20 μm 109
- Figure 4.8** Landau-de Gennes numerical modeling of 5CB in a PDMS mold with planar anchoring strength of (a) $7.74 \times 10^{-5} \text{ J/m}^2$, (b) $7.74 \times 10^{-4} \text{ J/m}^2$, (c) $7.74 \times 10^{-3} \text{ J/m}^2$, and (d) $3.87 \times 10^{-2} \text{ J/m}^2$ 110
- Figure 5.1** Design of the 1D channels for LCM alignment. (a) Illustration of LCMs oriented in patterned 1D channels, where LC molecule follows the local orientation of the channel; (b) Representation of a LC molecule within the 1D channel in a Cartesian coordinate. Channel direction is along y-axis; (c) Schematic of the 1D channel fabrication process. A pattern master is first fabricated by photolithography, and then replicated twice to PDMS and epoxy resin (D.E.R. 354), respectively, by soft lithography. (d) Chemical structures of RM82 and epoxy resin (D.E.R. 354). 117
- Figure 5.2** SEM images of the different patterned 1D channels with the same depth of 1.5 μm . (a-b) “+1” defect structures from different channel width: (a) 1 μm and (b) 2

μm . (c) Channels with 2 μm channel width with a “-1” defect. Image is tilted at 45°. (d) Channels with 2 μm feature width with a “+1/2” defect. Scale bars: 5 μm 122

Figure 5.3 POM images of LC alignment on patterned 1D channels. Left panels: schematics of LCs aligning in different patterns with topological defects marked. Right panels: POM images of (a-b) 5CB and (c-d) RM82 on the corresponding patterned surfaces. Scale bars: (a,c), 200 μm , (b,d), 25 μm 125

Figure 5.4 Actuation of the NLCE film with “+1” and “-1” defect array. (a) Schematic of LC orientation in the LC cell. LC director is twisted by 90° from bottom to top. (b-c) POM images of the NLCE film with parallel (b) and cross (c) polarizers indicated by the arrows in the up right corner. (d-e) Optical images of the LCE films at (d) room temperature and (e) 200 °C. Scale bars: (b-c) 100 μm , (e) 1 mm. 127

Figure 5.5 Actuation of NLCE sheet with “+1/2” and “-1/2” defect array. (a) Schematic of LC orientation in the LC cell. LC director is parallel from bottom to top. (b-c) Optical images of the NLCE films at (b) room temperature and (c) 200 °C. 129

Figure 6.1 Schematic illustration of the design of the chemically patterned surface for controlled LC anchoring. (a) NLC at the boundaries of homeotropic and planar anchoring domains represented by different colors: blue – homeotropic, green – planar, purple rods – LC mesogens. The black arrow represents the LC director (\mathbf{n}). A twist configuration of LC alignment at the boundary of homeotropic and planar regions is illustrated. (b) Illustration of the patterned surface with isolated circles. (c) NLC director field on the circular pattern shown in (b). Purple rods represent local LC director and the red dot indicates the “+1” point defect. (d) Illustration of the sample preparation process. Different colors represent different materials: Blue – glass, green – SU8. 143

Figure 6.2 POM images of 5CB on chemical patterns prepared from micro-contact printing of SAMs with different DMOAP concentration: (a) 1vol%; (b) 3vol%; (c) 8vol%. Scale bar: 60 μm 144

Figure 6.3 Reaction kinetics of DMOAP with SU8 and glass based on the change of water contact angles over time. (a) Water contact angles of glass and SU8 after different DMOAP treatment time. Insets: optical microscopy (OM) images of water droplets on the sample surface. Green dotted line indicates the optimized DMOAP treatment time (2 min). (b) OM images of water droplets on SU8 (top panel) and glass (bottom panel) after 2 min DMOAP treatment. 145

Figure 6.4 5CB on an array of circular patterns. (a) Polarized optical microscopy (POM) image of 5CB on the circular patterns. “+1” defects were found on each individual circle. Scale bar: 50 μm . Inset: Bright field (BF) image showing the circular patterns with topological defects of 5CB (black dots). Scale bar: 20 μm . (b) AFM image of a single SU8 circle on glass. 147

Figure 6.5 5CB on various chemical patterns. Top panels: designs and SEM images of the patterns. Bottom panels: POM images of 5CB on chemical patterns with shape of (a) square, (b) triplet of circles and (c) quadruplet of circles. Scale bars: top panels – 2 μm , bottom panels – 10 μm 149

Figure 6.6 5CB on arrays of squared checkerboard and connecting rings. (a-b) POM images of 5CB on the squared checkerboard with 0° (a) and 45° (b) cross-polarizer angles, respectively. (c-d) POM images of 5CB on the square array of connecting rings with 45° (c) and 0° (d) cross-polarizer angles, respectively. Insets in (a) & (c) show the schematic of the arrays. Insets in (b) & (d) show the BF images of 5CB with no apparent defects in (b) but tilted defects in (d) appeared as black dots. (e) Schematic illustration of the LC director field surrounding a homeotropic domain. The black lines represent LC director field, and the red dot shows the “ $-\frac{1}{2}$ ” defect. The red and blue curves at the boundary of the chemical pattern illustrate two different LC anchoring configurations: the splay distortion and twist distortion shown in the schematics below. Scale bars: (a-b) 10 μm ; (c-d) 40 μm 152

Figure 6.7 (a) BF and (b) POM images of the assembly of silica colloids (diameter of 1 μm) within the topological defects created by 5CB on the square array of circular patterns. The red arrows indicate the trapped colloids by the topological defects of NLC. Scale bar: 20 μm 154

CHAPTER 1: Introduction of Liquid Crystals and Liquid Crystal Polymers

1.1 Liquid Crystals

1.1.1 History of Liquid Crystals

Liquid crystal displays (LCDs) are ubiquitous in our daily life. However, few know that liquid crystal (LC) phases were first discovered back in 1888, much earlier than the recognition of most nano-materials nowadays and the development of electronics. In the late 1800's, Friedrich Reinitzer first observed a liquid crystalline phase in cholesteryl benzoate that showed two melting points and a cloudy fluid phase while heated on a hot stage towards clearing temperature¹. Later in 1888, Otto Lehmann, a German physicist, concluded that the cloudy fluid phase discovered by Friedrich Reinitzer was indeed a new phase of matter, and designed it as liquid crystal². Nonetheless, research of LCs in the first decades after discovery was slow, in part because the new material was not well understood and characterized. Little interest was paid to the new LC material until the 1960's when the stable cyanobiphenyl LCs were discovered and the first optical LCDs were demonstrated³. The application of LCs in LCDs soon led to research in both the fundamental physics of LCs and the chemical synthesis of new types of LCs. Because of their anisotropy in geometric, thermal, optical, electrical, and magnetic properties, LCs have not only become the basis of a \$100 billion industry each year, but also intrigued great interests by physicists, chemists, and material scientists to create ever complex structures, to direct assembly of colloidal particles, quantum dots, and metallic nanorods,⁴⁻⁹ to create smart materials such as artificial muscles and sensors¹⁰⁻¹², and to advance optoelectronic devices¹³⁻¹⁶.

1.1.2 Types of Liquid Crystals and Liquid Crystal Phases

LCs can be considered anisotropic fluids made of rod-like mesogens aligned with long-range orientational orders. In general, LCs can be categorized as thermotropic and lyotropic LCs. The phase transition of lyotropic LCs is induced by the change of both concentration and temperature of LCs in a solvent (typically water), whereas that of thermotropic LCs is only dependent on temperature. Most contemporary LCDs use thermotropic LCs³. Figure 1.1 shows several typical LC phases depending on the ordering of the common orientational direction, called the director n . In the isotropic phase, LC molecules are randomly orientated without positional order or orientational order. In the nematic phase, LC molecules exhibit one dimensional ordering but no positional order, that is LC molecules can translate in any direction without additional free energy penalty as long as the long axis of LC molecules are roughly aligned parallel to the local director n . A commonly used nematic LC, 4-cyano-4'-pentylbiphenyl (5CB), is shown in Figure 1.2. Smectic and cholesteric phases have higher packing symmetries (see Figure 1.1c-d). LCs in a smectic phase have positional order with a well-defined layer structure. A classical smectic LC is 4-cyano-4'-octylbiphenyl (8CB). The cholesteric phase, also referred as the twisted nematic phase, has a continuous twisting of molecules perpendicular to n between layers. Chirality can be obtained by adding a small amount of chiral dopants into a normal nematic LC phase.

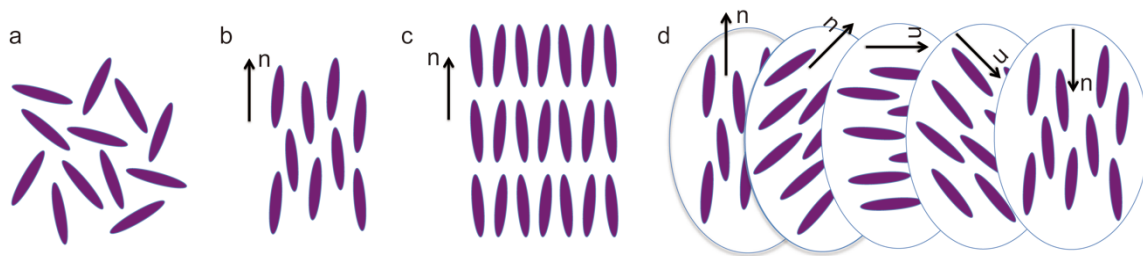


Figure 1.1 Schematic representation of different LC phases. (a) Isotropic. (b) Nematic. (c) Smectic. (d) Cholesteric. The arrows indicate the local LC director.

The degree of ordering of LC molecules is usually represented by a dimensionless factor, the so-called order parameter as

$$S = \frac{1}{2} \langle 3 \cos^2 \theta - 1 \rangle \quad (1-1)$$

where S is the order parameter, and θ is the angle between the orientation of LC molecule and the local director \mathbf{n} . From Eq. (1-1), one can see for arbitrary orientated molecules in isotropic phase, $S=0$, and for perfect alignment in crystals, $S=1$. In LC phases, $0 < S < 1$, with typical S in between 0.5-0.7 for low symmetry nematic LC phase, and 0.7-0.9 for high symmetry smectic phases.

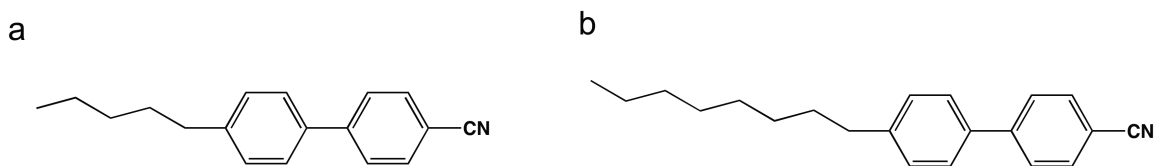


Figure 1.2 Chemical structures of two commonly used LCs. (a) 5CB. (b) 8CB.

1.2 Physical properties of liquid crystals

1.2.1 Anisotropy

Anisotropy is the most important and intrinsic properties of LCs. The chemical structures of LC molecules result in anisotropic intermolecular interactions, leading to LC phases of different ordering. For instance, the rod-like biphenyl group in 5CB (Figure 1.2) contributes to the shape anisotropy of the molecule. The biphenyl groups are energetically favored to align in parallel to maximize the translational entropy as a compensation of the loss of rotational entropy¹⁷. The short hydrocarbon tails in the 5CB disorder the packed biphenyl groups between molecules, thus, lowering the symmetry of the LC phase and preventing crystallization. The polar cyano group and biphenyl group in 5CB provide the anisotropic polarizability measured from the ordinary direction versus the extraordinary direction. Control of LC alignment or their anisotropy plays important roles in many LC applications. For example, anisotropic dielectric susceptibility of LCs makes them oriented under an electric field, a phenomenon that underlies the \$100 billion per year LCD industry³. Other anisotropic properties of LCs include birefringence, anisotropic magnetic susceptibility, anisotropic mechanical properties, viscosity, diffusion coefficients, and thermal expansion coefficients, leading to applications such as sensors, actuators, and optical devices¹⁸.

1.2.2 Elastic distortion and elastic energy

Naturally, when LC molecules assemble together, they align parallel to maximize the translational entropy. However, under many circumstances, it requires distortions in LC alignment to accommodate boundary conditions at interfaces, where LCs interact with a surface. There are three basic modes of elastic distortions in LC: splay, twist, and

bend as shown in Figure 1.3. The elastic energy associated with the elastic distortions is described as Frank-Oseen elastic energy density¹⁹

$$f = \frac{1}{2} \{K_1(\nabla \cdot \mathbf{n})^2 + K_2(\mathbf{n} \cdot \nabla \times \mathbf{n})^2 + K_3[(\mathbf{n} \cdot \nabla)\mathbf{n}]^2\} \quad (1-2)$$

where K_1 , K_2 , and K_3 are the splay, twist, and bend elastic constants, respectively. The free energy of local deformation of the director field is proportional to the Frank elastic constants and to the quadratic order of the appropriate spatial gradient of \mathbf{n} . Therefore, the free energy density of the director field can be described in a more fundamental way

$$f = \frac{1}{2} K_i (\partial \mathbf{n}_j / \partial \mathbf{s}_k)^2 \quad (1-3)$$

where $i=1, 2, 3$ for three elastic constants, respectively, and j and k are integers ranging from 1 to 3 for expression of the director \mathbf{n} in three dimensions.

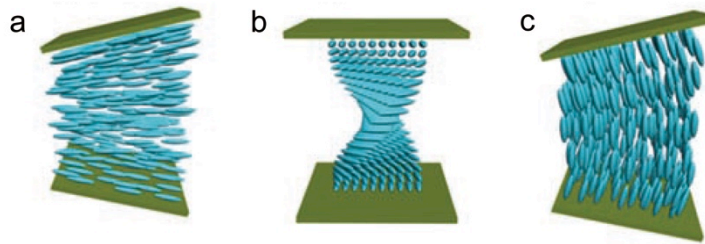


Figure 1.3 Schematic illustration of elastic distortions in a nematic LC. (a) Splay. (b) Twist. (c) Bend. Reproduced by permission from literature²⁰.

1.2.3 Topological defects and core energy

Topological defects occur when alignment of LC molecules come to a singularity, as shown in Figure 1.4. Within the topological defects, LC orientation is undefined and the phase is isotropic. The free energy associated with the topological defects is called core energy, which is introduced by Landau-de Gennes theory²¹. The mathematical expression of core energy in nematic LCs from q tensor Landau theory is

$$F_{core} = \int dV \left\{ \left[\frac{1}{2} A \text{tr}(Q^2) + \frac{1}{3} B \text{tr}(Q^3) + \frac{1}{4} C (\text{tr}(Q^2))^2 \right]^2 \right\} \quad (1-4)$$

where F_{core} is the core energy of defect, A , B and C are constants, and Q is a symmetric and traceless tensor representing LC molecule orientation. Core energy in the nematic phase is the free energy that stabilizes the nematic phase against the isotropic phase. So the physical meaning of core energy indicates the stability of nematic phase; with larger core energy, the nematic LC phase is more stable.

In a typical LC phase, such as the nematic phase of 5CB, the defect core is ~ 10 nm, comparable with the dimension of many nanomaterials, making it interesting, for example, to assemble nanoparticles and amphiphiles in the defect core^{6-9, 22}. There are two major categories of topological defects in the form of points and lines (or disclinations) shown in Figure 1.4. Depending on the different organizations of LC molecules surrounding the defect, defects can be divided into different types and characterized by a pseudo-topological charge number, the winding number. The winding number of a LC defect (W) is defined by the total number of times that LC director

travels counterclockwise around the defect

$$W = \frac{\theta}{2\pi} \quad (1-5)$$

where θ is the angle that the local director turns around the defect. There are four classical topological defects in LCs, including +1, -1, +1/2 and -1/2 defects shown in Figure 1.4.

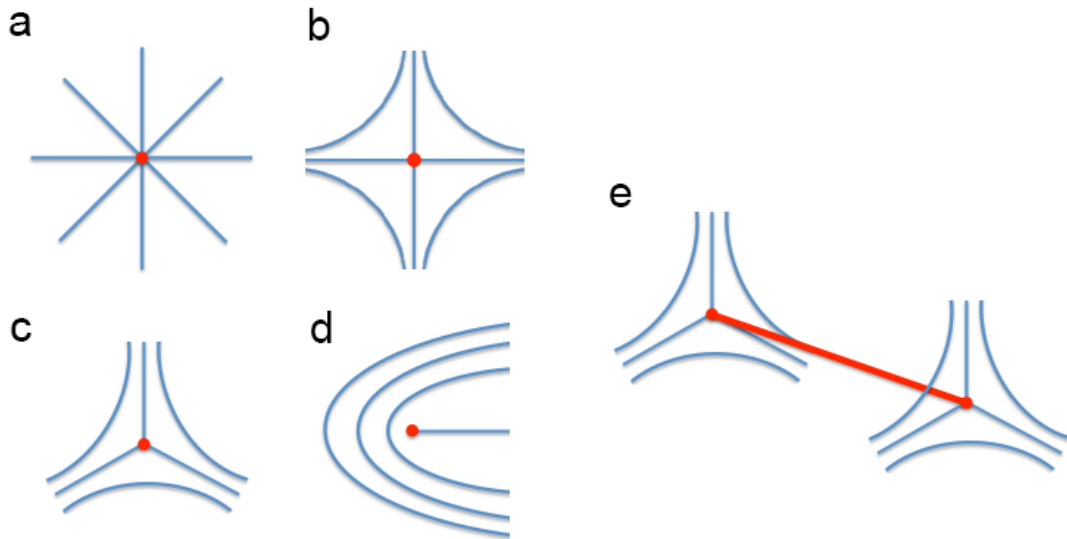


Figure 1.4 Schematic of topological defects in a nematic LC. (a-d) Point defects: (a) +1, (b) -1, (c) -1/2, (d) +1/2. (e) -1/2 line defect. The blue lines represent LC director and the red dots and lines represent LC defects.

1.2.4 Surface anchoring and surface anchoring energy

When LCs align on a surface, there is always a specific direction near the surface that the LC director \mathbf{n} follows, which propagates into the bulk to a certain distance, ranging from tens of nanometers to micrometers²³. As seen in Figure 1.5, there are three

types of alignment for the LC director on a surface: 1) homeotropic anchoring where LC director is perpendicular to the surface, 2) planar anchoring where LC director is parallel to the surface, and 3) tilted anchoring where LC director is tilted with a zenithal angle θ between 0° and 90° . The surface that contacts with the LC is usually considered flat at the microscopic scale, and the orientation of LC on the surface is defined by the azimuthal angle ϕ and zenithal angle θ (Figure 1.5). In the case of homeotropic anchoring, $\theta = 90^\circ$. For planar anchoring, there are homogenous alignment and heterogeneous (random or degenerated) alignment. Homogenous alignment is achieved when LC molecules orient uniformly in the plane of the surface with a fixed angle ϕ . Heterogeneous alignment occurs when LC orientation is not uniformly defined and angle ϕ has different values at different points on the surface. In a tilted anchoring, angle θ is constant and angle ϕ is arbitrary. The minimum free energy orientation direction of LC on a surface is usually called the “easy axis” of LC alignment. The surface anchoring energy that deviates from the minimum free energy state is expressed by²³

$$f_s = \frac{1}{2} [W_{\theta_0} \sin^2(\theta - \theta_0) + W_{\phi_0} \sin^2(\phi - \phi_0)] \quad (1-6)$$

where f_s is the surface anchoring energy, θ_0 and ϕ_0 are the zenithal angle and azimuthal angle of the “easy axis”, respectively, and W_{θ_0} and W_{ϕ_0} are zenithal and azimuthal anchoring coefficients, respectively, that represent the free energy required for the maximal deviation of LC director from the “easy axis”. The surface anchoring strength is

normally considered strong when f_s is on the order of 10^{-3} - 10^{-4} J/m², and weak for $f_s \sim 10^{-5}$ - 10^{-6} J/m². The alignment of LC molecules in a material is an energetic consequence of the competition between surface anchoring energy and elastic distortion energy. Extrapolation length λ is an important parameter to characterize the competition between surface anchoring energy and elastic energy for a LC confined on a surface,

$$\lambda = \frac{K}{W} \quad (1-7)$$

where K is the average elastic constant of LC, and W is the surface anchoring coefficient. The physical meaning of extrapolation length is the distance from the surface where LC director maintains orientation along the “easy axis”²³. In the case of strong anchoring, λ is typically in the range of 1-10 nm, indicating that LC director coincides with the “easy axis” close to the anchoring surface.

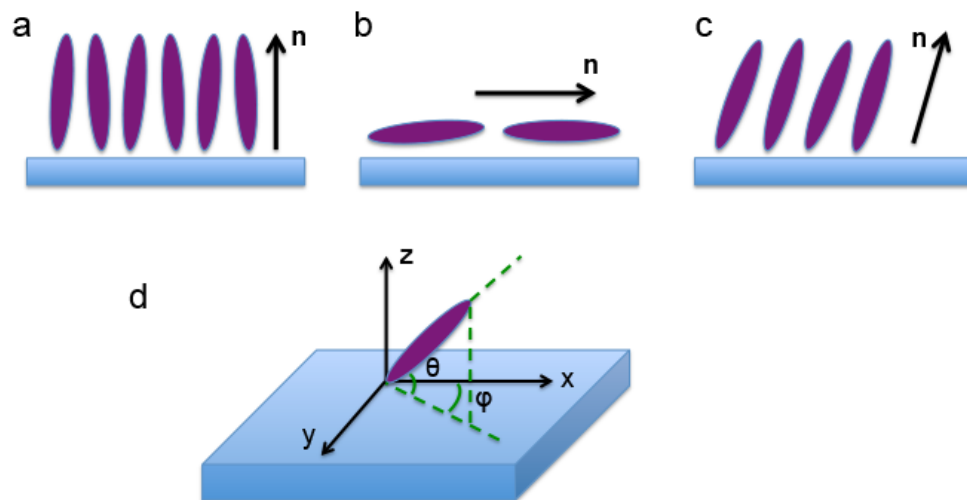


Figure 1.5 Schematic illustration of LC anchoring on a surface. (a) Homeotropic. (b) Planar. (c) Tilted. (d) Representation of LC anchoring on a surface determined by an azimuthal angle ϕ and a zenithal angle θ .

1.3 Anchoring control in nematic liquid crystals

As illustrated above, the molecular orientation and assembly of LC molecules plays a key role to control its function. For small molecule LCs (e.g. 5CB), the anchoring can be successfully regulated through various boundary conditions, including surface chemistry, topology, and topography. In this thesis, anchoring control of nematic LCs will be discussed in detail.

1.3.1 Surface chemistry

As discussed in Section 1.2.4, when LCs are brought in contact with a surface, the orientation of LC director near the surface can be aligned homeotropically, planarly or tilted, driven by the tendency to minimize the energy at the interface. The different orientational angle is dependent on the surface chemistry or the surface tension of the substrate, and the anisotropy of the surface tension of the LC²⁴. Simplified surface anchoring rules are summarized in Table (1-1).

Table (1-1) Dependence of LC orientation on surface tensions

	Surface tension	LC orientation
1	$\Delta \gamma > 0, \gamma_s < \gamma_{\perp};$ $\Delta \gamma < 0, \gamma_s > \gamma_{\perp};$	Homeotropic
2	$\Delta \gamma > 0, \gamma_s > \gamma_{\parallel};$ $\Delta \gamma < 0, \gamma_s < \gamma_{\parallel};$	Planar
3	$\gamma_s \in [\Delta \gamma]$	Tilted

* γ_{\parallel} and γ_{\perp} are surface tensions of LC parallel and perpendicular to the director, respectively. $\Delta \gamma = \gamma_{\parallel} - \gamma_{\perp}$ is the anisotropy of the surface tension of LC. And γ_s is the surface tension of the substrate. Reproduced by permission from literature²⁴.

Since different LCs have different surface tensions (γ_{\parallel} and γ_{\perp}) and surface tension anisotropy, LC anchoring on substrates of the same surface tension varies. In the case of 5CB, it aligns homeotropically on surfaces with low surface tensions, such as poly(dimethylsiloxane) (PDMS) and dimethyloctadecyl[3-(trimethoxysilyl)propyl] ammonium chloride (DMOAP) coated surfaces. Planar anchoring of 5CB is usually obtained on high surface tension substrates, for instance, silica and surfaces coated by poly(vinyl alcohol) (PVA). Nevertheless, the impact of surface chemistry on the anchoring of LCs at interfaces is much more complicated than the simplified rules summarized in Table (1-1). Anisotropic molecular interactions between the LC molecules and the molecules at the substrate surface is the main driving force to aligning LCs, and surface tension is simply an apparent parameter to control experimentally. Van de Waals force, electrostatic interaction, hydrogen bonding, and $\pi - \pi$ interaction at the interface can all contribute to the orientation of LC alignment on a substrate²³. So far, due to the complexity of LC system and the difficulty to precisely measure molecular interactions at the microscopic scale, only a few LC systems have clearly elucidated mechanisms on the role of surface chemistry to LC alignment²³.

Nevertheless, surface tension and textures are the most commonly used parameters to direct LC anchoring, and a few methods have been developed to control the “easy axis” of LCs at interfaces for fine-tuning both θ and ϕ . For example, rubbing a velvet cloth on a polymer surface (e.g. polyimide) produces 1D microgrooves to align LCs with constant ϕ .^{10, 11, 25} The polymer chains at the surface can be dragged and orientated along the rubbing direction, while the $\pi - \pi$ interactions between the aromatic

mesogens and the aromatic groups in polyimide further enhance anisotropic molecular interactions between LCs and the substrate. Scratching the surface using an atomic force microscopy (AFM) tip²⁶, mimicking the rubbing process, can also locally align LCs in microscale with arbitrary directions.

Photoalignment is another powerful technique to orient LC at interfaces^{16, 27, 28}. A thin photoalignment layer (typically consisting of azobenzene groups) is coated on the substrate, followed by exposure to the polarized UV light. Thus, the photosensitive groups in the photoalignment layer are reoriented either parallel or perpendicularly to the polarization direction of the UV light. When LCs of interests are cast on the photoalignment layer, their orientation follows the local orientation of the photoalignment layer.

Patterning surface chemistry with alternating homeotropic and planar anchoring regions is another effective method to align LCs²⁹⁻³¹ (see Figure 1.6). It allows for more complex director field patterns. The patterns can be created by top-down methods, including photo-patterning²⁹, micro-contact printing of self-assembled monolayers (SAMs)^{30, 31}, and nanoimprint lithography^{32, 33}. The director of LCs on the patterned surface follows the local surface chemistry and is also controlled by the boundary conditions created at the border between homeotropic and planar anchoring regions. This technique largely relies on spatially inhomogeneous surfaces in combination with LC elastic anisotropy to control the alignment of LCs. At the local region, patterned surfaces can be either isotropic, which provides an arbitrary ϕ for LC alignment^{29, 31}, or anisotropic with a locally fixed ϕ ³⁰. It should be noted that LCs on an isotropic surface

with patterned surface chemistry can still be aligned uniformly, due to the confinement at the boundaries and elastic anisotropy of LCs^{29,31}. As a result of elastic anisotropy in most nematic LCs, they prefer twist configurations at the boundary between the homeotropic and planar regions. Within each micro-scale domains, LC molecules are uniformly aligned. Since fabrication of micropatterns is readily accessible nowadays, chemical patterning has been considered a promising technique to be applied in practical applications, e.g., wide-viewing angle LCDs and hybrid diffractive-refractive devices^{29,31}.

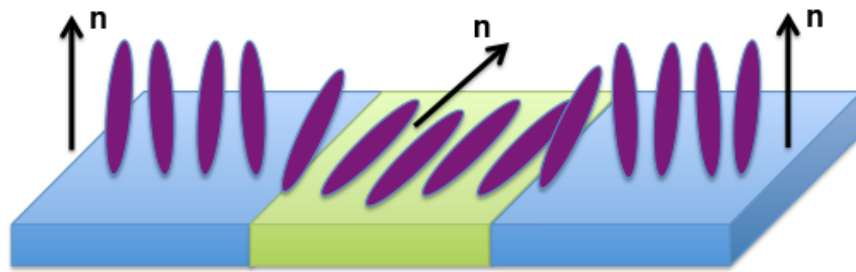


Figure 1.6 Schematic illustration of LCs on a chemically patterned surface. The blue region indicates homeotropic anchoring for LC, and the green area is random planar anchoring.

1.3.2 Topology and topography

Topology of an object is the intrinsic property of the object that is independent of its size or geometry. It can be preserved under continuous deformation of the object. Two objects can be considered as topologically equivalent when there is a way to transform from one to another without cutting or changing the number of holes and handles. For example, a coffee mug and a donut are topologically equivalent. Colloids in nematic LCs have been demonstrated to generate three-dimensional (3D) director fields of LCs, leading to different types of topological defects dictated by the topology of the colloids⁵.

³⁴⁻³⁶. Spherical colloids with homeotropic anchoring boundary condition are the most widely studied systems in nematic LC to introduce either “hedgehog” point defects or “Saturn ring” line defects surrounding the colloids. The resulting dipole and quadruple interactions are in turn used to assemble colloids.^{4,5} Other types of topological colloids of different genus have also been designed and investigated in nematic LCs to test the Gauss–Bonnet and Poincaré–Hopf index theorems³⁷⁻³⁹. Theoretically predicted topological charges carried by the topological defects that are induced by colloids have been experimentally confirmed as a function of the genus of the topological colloids^{35,36}.

As opposed to topology, topography of an object comprises surface shape and features related to size and geometry. It is certainly true that LC anchoring in the near field on a flat surface has been well understood and LC director field and topological defects induced by colloid topology have been extensively exploited in recent years. A comprehensive description of the LC anchoring behaviors on topographical surfaces remains a complicated matter, especially when the pattern size decreases to nanoscale.⁴⁰ Although rubbing to control LC alignment has been well adopted since 1960s, the fundamental mechanism remained unclear for decades²⁵. Berreman⁴¹ first established a theoretical model on LC anchoring on a topographical grooved surface and presented the resultant elastic distortion energy in 1972. Berreman’s work has since become the benchmark study of LC alignment guided by the underlying geometrical patterns. For a long time in experiments, micro- and nano-grooves have been found to show geometrical constraints on the alignment of nematic LCs^{10, 11, 25, 40}. LCs confined within the planar anchored grooves align parallel with the groove direction to minimize elastic distortion, and smaller sized grooves offer stronger alignment for LCs. Researchers have intended to

relate the observed LC anchoring to the microscopic topography of the interface and to understand the energetic origin responsible for the orientation of LC alignment. The surface anchoring energy density for a nematic LC on sinusoidal grooves is sensitive to both the size and geometry of the groove as ⁴¹

$$\rho_{max} = \frac{\pi^2 K A^2}{\lambda^3} \quad (1-8)$$

where ρ_{max} is the maximum free energy density for LCs aligned perpendicular to the groove direction, K is the average elastic constant of the LC, and A and λ are the amplitude and wavelength of the groove, respectively. Similarly, Eq. (1-8) can be used to estimate the free energy density of LCs on one-dimensional (1D) channels fabricated by top-down techniques.

Different from planar anchoring on a topographical surface, on a surface topography with homeotropic boundaries, LCs are guided by a “ π -like interaction”, and an anchoring flip of nematic LCs from homeotropic to planar anchoring on 1D nano-channels has been reported⁴²⁻⁴⁴. The anchoring flip⁴⁰ of LCs is induced by the competition between surface topography and chemistry in the alignment regions. When surface corrugation is small, surface chemistry effect is dominant, leading to homeotropic anchoring of LCs on the 1D channel. At a large surface corrugation, surface topography becomes dominant, leading to planar anchoring.

Nematic LCs in micro-pillar arrays with homeotropic anchoring have also been studied⁴. Attributed to the topography of the micropillars, stable bulk disclination rings

encircling the pillars are observed with their size and shape dictated by the micropillars. Notably, the formation of bulk disclination rings in the homeotropic pillar array is slightly energetically unfavorable in numerical simulation when compared to the states without bulk defects. Though the multistability in the micropillar system has not been clearly documented, those bulk defects have been demonstrated to remotely assemble microparticles at the LC-air interface through the balance of elastic energy and capillary energy⁴.

1.4 Anchoring control for nematic liquid crystal monomers/polymers

Nematic liquid crystal polymers (LCPs) polymerized from liquid crystal monomers (LCMs) bearing acrylate/methacrylate, alkene, or epoxy⁴⁵ are of interests for high-strength fibers, LC optical devices, actuators and sensors^{10, 45, 46}. The functionality of LCPs is closely related to their internal structures, thus the alignment of LC mesogens. LCMs often have weaker anchoring strength on surface in comparison with small molecule LCs. Here, we briefly discuss common techniques to align LCMs, many of which are different from that to align small molecule LCs.

1.4.1 Rubbing

Rubbing on a polymer surface, typically polyimide, is a classical approach to align nematic LCMs into monodomains^{10, 11}. Similar to the concept of aligning small molecule LCs on the rubbed polymer surface, the molecular orientation of LCMs follows the rubbing direction. However, this method is much more limited to align nematic LCMs since the driving force for the orientation is limited near the surface with a typical

distance smaller than 50 μ m.

1.4.2 Mechanical stretching or shearing

Mechanical stretching or shearing is commonly used to align LCMs macroscopically⁴⁷⁻⁵⁰. Mechanical stretching is typically accomplished in two steps. First, LCMs are slightly polymerized into LC oligomers or weakly crosslinked LCPs so that the sample is mechanically stable or highly viscous. Next, the bulk sample is mechanically stretched, typically uniaxially, to align the polymer chains against conformational entropy, followed by crosslinking to lock the alignment. Alternatively, LC fibers are drawn from a polymer melt^{51, 52}, or through a more sophisticated electrospinning process^{53, 54}, followed by immediate crosslinking. It should be noted, however, that LCPs fabricated by these methods often contain high residual internal stress since LCMs are partially polymerized in the first step. Consequently, the polymer chains in these LCPs cannot be interpreted as Gaussian chains, and the macroscopic shape of the crosslinked LCPs cannot be maintained over a long period of time. To solve the internal stress problem, a novel approach has been developed by taking advantage of exchangeable covalent bonds⁵⁵. In that particular system, the internal stress generated from the change of the conformational entropy of the polymer chains can be gradually reduced during the second step stretching, through the reformation of the crosslinking network with a new polymer chain conformation.

Mechanical shearing of LCMs using confined channels is another way to align LCMs since the early 1980s^{56, 57}. In the method of micro-molding in capillaries melted LCMs are drawn to 1D microchannels (5-20 μ m) by capillarity⁵⁸, generating mechanical shearing force at the LCM-channel interface, thus orienting LCMs in the flow direction.

Shortly after, LCMs are photocrosslinked under UV light. Likewise, LCMs can be aligned in a micro-fluidic device⁵⁹. By controlling the flow rate and channel size, a wide range of LCP particles with variable size and shape can be created, while LCPs made from a 1D channel are simply fibers. The major advantage of mechanical shearing methods, compared to mechanical stretching, is that the final LCPs have negligible internal stress, since pre-polymerization is no longer required, and LCMs can be directly crosslinked into LCPs.

1.4.3 Electric and magnetic fields

While mechanical stretching and shearing provide anisotropic environments for LCM alignment, they do not directly orient individual LC molecules. Electric and magnetic fields, however, can be used to explicitly align LC mesogens in the direction of the applied field by taking advantage of the electric and magnetic anisotropy of LC molecules.

Electric fields are primarily used for LCMs with strong dipole moments, such as ferroelectric LCs⁶⁰⁻⁶². Typically, LCMs with crosslinking groups are sandwiched between two indium tin oxide (ITO) glasses, separated by a spacer with a typical thickness of tens of micrometers. An alternating electric field is then applied to the ITO electrodes to align LCs until formation of a monodomain. Subsequently, they are UV crosslinked to lock the LC alignment while maintaining the electric field.

Strong magnetic field generated by an electromagnet or a rare-earth permanent magnet, however, is more commonly used to align nematic LCMs, especially in a microstructured mold⁶³⁻⁶⁵ due to their strong diamagnetism. The effect of a magnetic field can be quantified by the magnetic coherence length, ξ_H , the length scale over which the

LC director can orient and reorient along the field direction, given by

$$\xi_H = \sqrt{\frac{K_3}{\Delta\chi H^2}} \quad (1-9)$$

where K_3 is the bend elastic constant of LC, $\Delta\chi$ is the anisotropy of magnetic susceptibility, and H is the magnetic field strength. For a commonly used small molecule nematic LC such as 5CB, K_3 is on the order of 10^{-11} N and $\Delta\chi$ is typically on the order 10^{-7} .²¹ So with $H \sim 10^6$ A/m (~ 1 Tesla), 5CB with any boundary conditions can be reoriented on a length scale $\xi_H \sim 10$ nm. Therefore, a strong magnetic field could be quite effective in aligning 5CB molecules into monodomains within a mold used in soft lithography. However, a much larger magnetic field is required to fully orient LCMs within a confinement, which could be due to larger K_3 of LCMs or smaller $\Delta\chi$. Though the fundamental origin of this phenomenon has not been well-understood, LCPs with partial monodomain LC orientation have been successfully fabricated by aligning LCMs in the magnetic fields⁶³⁻⁶⁵.

1.4.4 Photoalignment

Though the photoalignment technique was developed in the early 1980s and it has since been successfully adopted by the LCD industry, its application to LCMs was realized only recently⁶⁶⁻⁶⁸. The manipulation of LCM alignment using photoalignment materials is non-trivial, and requires specific LCM systems to satisfy the sensitivity of material chemistry to the surface alignment layer. Hence, only a few LCM systems have been demonstrated to faithfully orient along with the photoalignment layer⁶⁶⁻⁶⁸.

Nevertheless, within the scope of the successful examples, LCPs have been programmed with desired shape change and actuation through the monolithic control of LCM director profiles with a variety of complexity⁶⁶⁻⁶⁸. To prepare spatially heterogeneous LCPs, a special optical setup needs to be established to control the local surface alignment of the photoalignment layer, from spot to spot with a pixel dimension in the range of 100 μm . After filling LCMs onto the alignment layer, LCMs follow the surface alignment layer and orient locally. Arbitrary and spatially complex patterns can be generated in LCMs, and the director field profile can be transferred into LCPs by *in situ* photocrosslinking. Besides expensive and specialized optical setups, and the photoaligning process is usually time-consuming, e.g. it takes 1-2 hours for a sample with an area $\sim 4 \text{ cm}^2$, thus its application has been limited⁶⁸.

1.5 Liquid crystal polymers

1.5.1 Types of liquid crystal polymer networks

A liquid crystal polymer network combines the elasticity of polymer network and the anisotropy of LCs. Depend on their architectures, LCPs can be categorized into three types: main-chain LCPs in which the mesogens are part of the polymer backbones, side-chain LCPs in which mesogens are attached to the polymer backbones via a flexible spacer, and mixed type LCPs in which mesogens are in both main- and side- part of the polymer (see Figure 1.7). Remarkably, main-chain LCPs can exhibit an actuation strain up to 400%^{10, 65} in response to external stimuli. But such materials usually have a rather high phase transition temperature, typically 150-200 $^{\circ}\text{C}$, thus, limits their fabrication and

application as actuators. In contrast, side-chain LCPs usually possess a strain of 10%-50%¹⁰. However, they have lower transition temperatures, due to the decoupling of the mesogenic characteristic of the LC from the motion of the polymer chains.

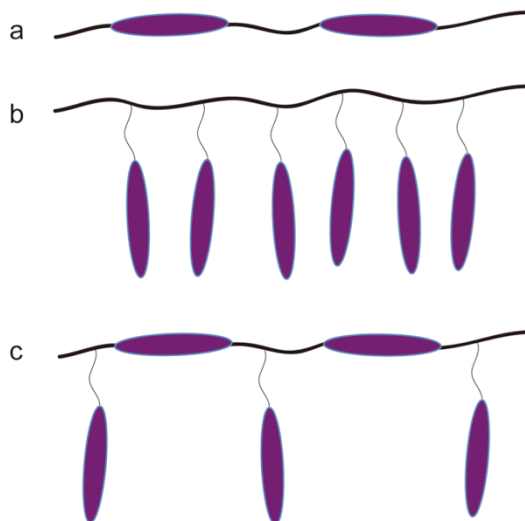


Figure 1.7 Schematic of different types of liquid crystal polymers. (a) Main-chain LCP. (b) Side-chain LCP. (c) Mixed type. The purple rods represent LC mesogens.

LCPs can also be categorized by their thermodynamic signatures. Rubbery LCPs are usually called liquid crystal elastomers (LCEs), while glassy LCPs are known as liquid crystal glasses (LCGs). LCEs are soft and more responsive to external stimuli, while LCGs are more mechanically stable but less responsive. Both LCEs and LCGs have been investigated for their applications in actuators, which will be discussed in the following section.

LCPs can also be identified based on their responsiveness to external stimuli. There are three major types of stimuli that have been used to trigger the deformation of LCPs: heat, light, and electric field. Accordingly, LCPs can be divided into thermo-responsive, light-responsive, and electro-responsive ones^{10, 11, 69, 70} (see Figure 1.8). Most

LCPs are thermo-responsive due to the fact that LCPs still possess the same mesophase characteristics of ordinary LCs after cross-linking, thereby retaining LC phase transitions in the polymer network. As shown in Figure 1.8a, heating across the phase transition temperature, e.g. the nematic-isotropic transition (T_{NI}), the reorientation of LC mesogens leads to a macroscopic shape change of the LCP, where the material contracts along the director and elongates perpendicular to the director. Since mesogens are confined by the crosslinked polymer network, the shape change of the LCP network is reversible.

Light-sensitive LCPs typically consist of light-sensitive functional groups⁶⁹, e.g. azobenzenes, as shown in Figure 1.8b. Isomerization of *cis*- and *trans*-azobenzenes occurs when the system is exposed to either UV light (*trans*- to *cis*-) or visible light (*cis*- to *trans*-). The molecule isomerization also induces the macroscopic shape change similar to that of the thermo-sensitive LCPs. In this case, the azobenzene moieties can either be covalently bonded to the LCP network, or physically absorbed into the network. It should be noted, however, that in the case of light-sensitive LCPs, light penetration depth is typically on the order of tens of micron. Thus, light-sensitive LCPs are usually thin, and the extent of isomerization gradually decreases along the sample thickness, leading to anisotropic bending toward the light (Figure 1.8b).

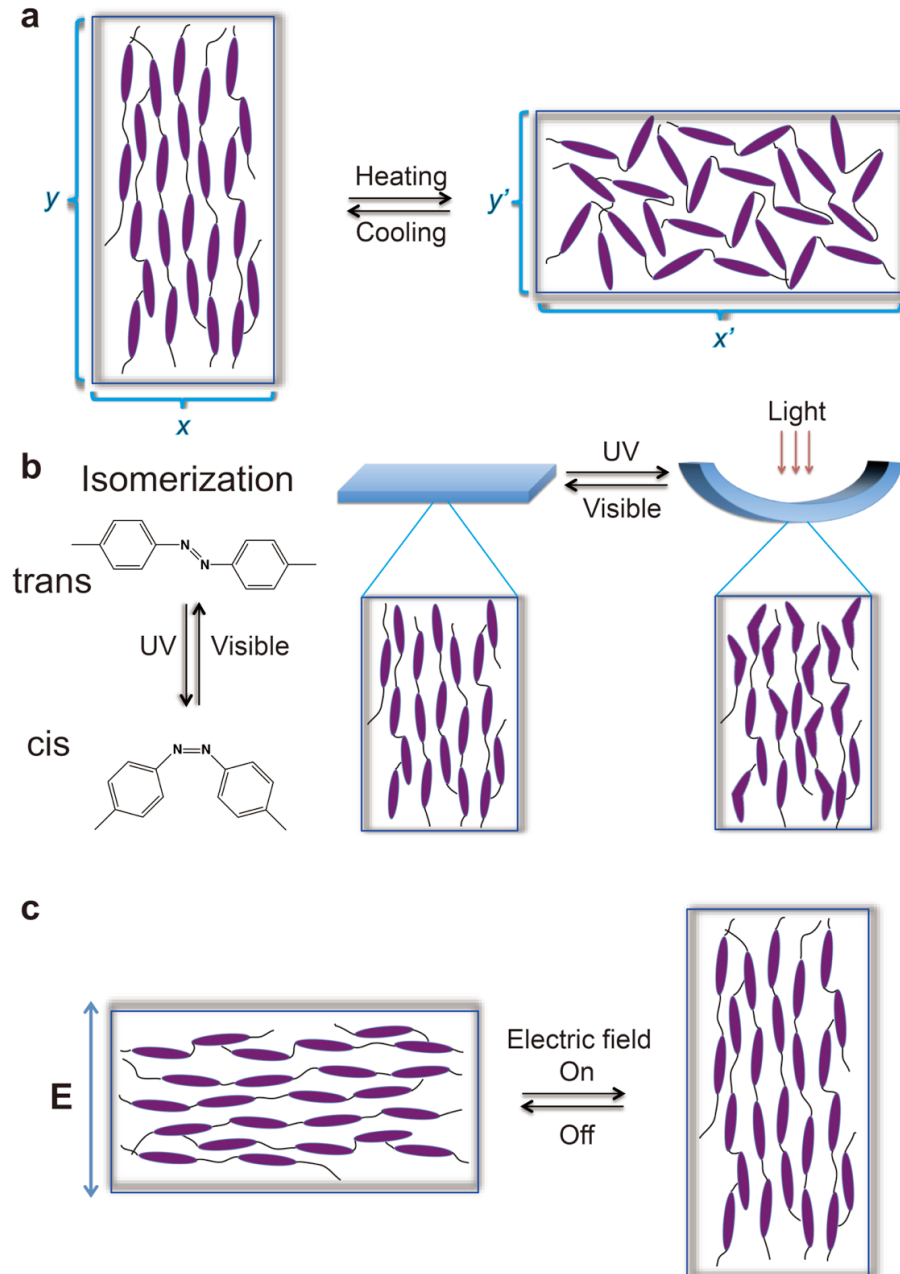


Figure 1.8 Illustration of different responsive LCPs. (a) Thermo-sensitive LCP. A rectangular shaped nematic LCP changes dimensions from $x \times y$ to $x' \times y'$, when heating above nematic-isotropic phase transition temperature. (b) Light-sensitive LCP. Left panel shows the isomerization reaction of azobenzene, and right panel demonstrates the shape transformation of a thin LCP membrane under light irradiation. (c) Electro-sensitive LCP. The schematic demonstrates the shape transformation of a LCP film when switching the electric field.

Electro-sensitive LCPs (Figure 1.8c)⁷⁰ are rather rare and most of them are swollen LC gels. When a strong electric field ($\sim 1\text{V}/\mu\text{m}$) is applied to an electro-responsive LCP, the mesogens reorient along the electric field due to their dielectric constant anisotropy, resulting in a shape change of the material. But the swollen LC gels are usually mechanically unstable and the electric field strength required to induce a deformation is typically high. Therefore, the study on electro-sensitive LCPs is very limited.

1.5.2 Stimuli responsiveness of liquid crystal polymers

Comparing to other responsive polymeric materials, such as hydrogels⁷¹⁻⁷⁴, semicrystalline polymers,^{75, 76} and electroactive polymers⁷⁷⁻⁷⁹, LCPs behave similarly in many aspects, for instance shape-fixity and shape-recovery (or shape memory effect) at the molecular level^{66, 68, 80, 81}. Due to internal strain in LCPs, the shape memory effect is two-way shape memory effect, that is it can reversibly change the shape between the original state and the temporary, deformed state while most of the shape memory polymers are one-way shape memory, which only remember the temporary shape. The reversible shape memory effect of LCPs has many potential applications, including soft robotics, biomedical devices, tunable optics, and surface morphing^{46, 82, 83}. Here, I will briefly review the actuation of LCPs from simple formats (e.g. thin films and fibers) to complex structures pre-programmed with embedded topological defects.

First, let me discuss approaches to trigger the actuation of LCPs in device applications other than *direct* heating, UV exposure, or application of an electric field to reorient LC mesogens. Although it is challenging to induce large deformation in non-swollen LCPs using an electric field, electricity can be alternatively used by transferring

electric energy into thermal energy and locally heat the LCP sample^{84, 85}. A successful approach is to incorporate thermoelectric materials, including conductive wires⁸⁵ and carbon nanoparticles⁸⁴, in LCP films to induce thermo-actuation. In this case, a relatively large longitudinal strain, ~20%, has been achieved in thin LCE films (50-100 μm thick) through resistive heating^{84, 85}. Likewise, carbon nanotubes (CNTs) have been integrated into the matrix of materials at a concentration as low as 0.1 wt%, which can induce a strain up to ~30% in LCE by irradiation in infrared (IR)⁸⁶. Magnetic actuation of LCPs has also been harnessed in both rubbery and glassy LCPs by incorporating magnetic nanoparticles⁸⁷ that vibrate and dissipate thermal energy through an electromagnetic field to heat the sample. Another aspect of CNTs is its dielectric anisotropy. Therefore, applying an electric field to the CNT/ LCE nanocomposite can reorient the CNTs and thus the LC mesogens, leading to mechanical deformation of the composite film⁸⁸.

Since De Gennes suggested the application of nematic LCEs as artificial muscles in 1975,⁸⁹ a variety of LCP devices with different compositions and shapes have been designed to couple the orientational order of LCs with the mechanical strain generated during phase transition, and to transduce chemical energy into mechanical energy. Simple mechanical deformation^{10, 11, 69, 90} was first realized in cilia-like fibers and flat thin films, in which mesogens are uniformly oriented. Actuation of such materials by heat or light usually results in a bending deformation of the fiber and flat film. Even though these mechanical deformations are macroscopic and simple, they can intrigue further miniaturization of LCP actuators. Bio-mimicking artificial cilia micro-actuators (~100 μm in diameter)⁹¹ have been fabricated by inkjet printing of LCMs to mimic the structure and motion of natural cilia. In this study, an array of cilia-like fibers composed with light-

sensitive LCPs are “printed” on a flat surface with one end of the cilia tightly bonded to the substrate while the rest keeps free-standing. When exposed to UV and visible light alternatively, the light-sensitive LCP cilia display fast bending and unbending movements in the time scale of a few seconds. It is envisioned that such micro-actuators can be used to create effective flow and mixing in an aqueous environment, similar to the behavior of natural microorganisms, e.g. paramecia. Thin films, on the other hand, have been used to construct light-sensitive LCE motors⁹² that can transfer light energy into continuous motion. In that case, a LCE ribbon (thickness $\sim 18 \mu\text{m}$) is placed encircling two pullers with one end of the puller exposed to an UV light, which contracts the ribbon, while the other end is irradiated by a visible light, leading to expansion of the ribbon. The contraction and expansion of the ribbon thus generate a constant rotational motion of the pullers, making them a LCE motor.

Micro-patterned LCE structures can also be fabricated by soft lithography techniques, such as micro-molding in capillaries⁵⁸ and replica molding using a PDMS mold^{63-65, 93}. LC orientation in these systems can be controlled either by shear induced alignment of LCMs in the 1D micro-channels for LCE fibers, or by applying a strong magnetic field across the PDMS mold, e.g. in the case of LCE micropillars. The resulting LCE microstructures usually display radial expansion and longitudinal contraction when triggered by an external stimulus. Change of surface contact area and thus water contact angle have been demonstrated during actuation of the LCE micropillar arrays, offering potential applications as tunable dry adhesives⁶³ and self-cleaning surfaces⁹³.

LCP actuators can also be applied to micro-electromechanical systems (MEMS)⁹⁴ due to their excellent electric isolation at high frequencies, mechanical flexibility, low

permeability to moisture and gases, low cost, and high dielectric constants. Typically, in the preparation of MEMS, LCEs are directly integrated into the fabrication process of the metal filaments to facilitate the contact between different materials. One successful example of LCE MEMS is a LCE-driven silicon gripper⁹⁴. The movement of the soft pincer jaw is triggered by the deformation of LCE components heated by the metal filaments.

Self-propulsion of LCEs, inspired by nature, has also been developed^{95,96}. A dye-doped LCE thin film that responds to light illumination is studied for swimming on a water surface⁸³. Triggered by UV light, the NLCE film bends at the water-air interface against capillary force, and move away from the light source, allowing them to be guided towards a desired direction. Inchworm-like motion of a LCE film is demonstrated⁸⁴, in which one edge of the film is made sharp while the other is round. Under irradiation of alternating UV and visible light, the two edges alternatively work as stationary points and the film exhibits forward movement.

Spatially more complex shape changes and surface variations have been realized in LCPs prepared with embedded complex LC director profile. The generation of complex shape transformation are of great interests in applications, including microfluidics^{81,91}, solar-energy harvesting⁹⁷⁻⁹⁹, and haptic displays^{67,100,101}. The ability of pre-programming local anisotropy with embedding topological defects makes this approach very attractive to control the actuation.

One approach to generate spatially oriented LC orientation in LCP is to pattern electrodes and applying alternating electric fields during LCM alignment^{67,72,102,103}. The resulting LCP materials, owing to the periodic variation of their director fields, have been

reported to tune surface roughness^{56, 61, 85} and create accordion-like actuation⁸⁶. Motivated by theoretical investigations¹⁰⁴⁻¹⁰⁸, LCPs with embedded topological defects have been fabricated through photoalignment with topological charges of +1, -1, +1/2 and -1/2, as well as high winding numbers up to +10 and -10^{66, 80}. Diverse surface features are generated upon heating above T_{NI} . Photoalignment has been recently extended to program LCEs with spatially controlled LC director field⁶⁸. With careful design of the director profile, giant strokes with conical deformations are shown in LCE membranes embedded with “+1” defects. Further, shape deployment is exploited with precisely controlled local director field, and a self-folding Miura-ori origami transformation is exhibited⁶⁸. The reconfigurability of the shape-programmable LCPs with locally controlled magnitude and directionality of the mechanical strain could extend our design of LCP actuators for a wide range of applications.

1.6 Thesis outline

The main focus of this thesis is to control LC anchoring and thus the formation of topological defects for both small molecule LCs and LCMs/LC polymers under a variety of boundary conditions. We then explore the use of topological defects to tailor assemblies of nano- and microparticles.

In Chapter 2, we exploit the bulk disclination rings formed in micro-pillar arrays to assemble gold nano-rods (AuNRs) for dynamic tuning of surface plasmon resonance. Directed by the homeotropic surface alignment and the topography of the pillars, topological defects encircling each micro-pillar can be formed precisely in the nematic

phase of 8CB. The size of the disclination ring can be fine-tuned by simply varying the temperature of the system. When AuNRs are present in the LC, they energetically favor migration to the LC defects. The assembly of the AuNRs and consequently the surface plasmon resonance peaks can thus be dynamically and reversibly tuned by varying the dimension of the disclination rings through heating and cooling the sample system across phase transitions. By carefully optimizing LC anchoring conditions with various surface chemistry and pillar dimension, the plasmon peak shift can be maximized. For homeotropic pillar arrays with pillar aspect ratio=1.3, the transverse and longitudinal plasmon peak shifts are ~ 100 and ~ 153 nm, respectively.

In Chapter 3, we introduce a new type of nematic LCM that can be faithfully aligned by surface alignment techniques, including surface chemistry, topography and topology, analogous to non-reactive LCs, e.g. 5CB. We design our LCMs based on strong intermolecular dipole-dipole interactions to increase the stability of nematic phase, and thus enhance the core energy of the nematic LC. Predicted from theory, higher core energy nematic LCs can more efficiently suppress spurious defects in the alignment, and more effectively lead to the energy ground state of LC anchoring. Our newly designed LCMs show alignment properties analogous to those of 5CB in various topographical patterns. With faithful control of LCM alignment, the system is then crosslinked into LCP via cationic polymerization. Upon photocrosslinking, the orientational order of mesogens is effectively locked, allowing for direct visualization of the LC director field and defect structures by Scanning Electronic Microscopy (SEM). We show our method is effective to study LC anchoring in a variety of settings from escaping LC configuration in 1D channels, pores and between micro-pillars, to complex director field with topological

defects and even metastable configurations. Our method affords a resolution of 100nm, which is much smaller compared to that of typical polarized optical microscopy. Further, we use SEM imaging to calculate the extrapolation length of the LCM for planar and homeotropic anchoring.

In Chapter 4, we show LCM anchoring control in a micro-pillar actuator system of nematic LCEs (NLCEs) fabricated from replica molding by PDMS molds. LCM alignment control in micro-pillars plays a vital role in manipulating the actuation behavior of NLCE pillars. Specifically, monodomain alignment of LCMs with vertical orientation is desired to maximize the shape change and mechanical strain of the NLCE actuator. Such anchoring configuration is first illustrated by Landau-De Gennes numerical modeling in the cylindrical pores with planar anchoring. Following the simulation, we achieve planar anchoring of LCM by coating a thin layer of poly(2-hydroxyethyl methacrylate) (PHEMA) to the surface of the PDMS mold, prior to the replica molding process of LCMs. After crosslinking, the resulting NLCE pillars show a large radial strain ($\sim 30\%$) upon actuation by heating the sample across the nematic-isotropic phase transition, which is reversible upon cooling.

In Chapter 5, We develop a new technique to direct LCM alignment on patterned 1D channels and to program LCE actuation. Complex LCM director profiles embedded with topological defects are essential to realize controllable and programmable shape change of LCEs. By exploiting the confinement of the topographical 1D channels, nematic LCMs can be faithfully oriented with the local channel direction. Strong anchoring at the surface can be achieved by optimizing the surface chemistry and surface topography of the channel. We demonstrate that epoxy 1D channels with channel width

2 μm , spacing 2 μm and depth 1.5 μm can provide faithful alignment of complex LCM director profiles, while affording simplicity, low cost and easy access for the fabrication process. The resulting LCE membranes show shape transformation from 2D flat-sheets to complex 3D objects through controllable bending and stretching. LCE membrane embedded with “+1” and “-1” defect arrays displays a 3D “cone” array when actuated by heating. And the sample with “+1/2” and “-1/2” defect arrays shows a 3D “wrinkle-like” deformation upon actuation.

In Chapter 6, we further explore nematic LC anchoring control and defect formation on chemically patterned surfaces. We prepare planar anchoring SU8 micropatterns on homeotropic DMOAP coated glass substrates. By exploiting the geometry of the boundaries of the chemical patterns in combination with anisotropic LC elasticity, we show that LC orientation can be precisely controlled and various topological defects can be formed. On the isolated SU8 patterns, including circles, squares, triplet and quadruplet of circles, “+1” defects are formed regardless of the pattern geometry. On the connecting patterns, including squared checkerboard and arrays of touching rings, LC anchoring is highly dependent on the pattern geometry: no topological defect is observed on the checkerboard pattern while the “-1/2” defect array is observed on the array of rings. Furthermore, we demonstrate preliminary results of trapping silica colloidal particles by topological defects generated from the chemical patterns of a circular array. Further studies will be carried out using silica colloids with different surface treatments and sizes.

In Chapter 7, I summarize the dissertation and discuss the outlook and extensions of the work presented in this thesis.

1.7 References

1. Reinitzer F (1888) Beiträge zur Kenntniss des Cholesterins. *Monatshefte für Chemie* 9(1):421-441.
2. Lehmann O (1889) Über fließende Krystalle. *Z. Phys. Chem.* 4:462-472.
3. Castellano JA (2005) *Liquid Gold: The Story of Liquid Crystal Displays and the Creation of an Industry* (World Scientific Publishing, Singapore).
4. Cavallaro M, *et al.* (2013) Exploiting imperfections in the bulk to direct assembly of surface colloids. *Proc. Natl. Acad. Sci.* 110(47):18804-18808.
5. Muševič I, Škarabot M, Tkalec U, Ravnik M, & Žumer S (2006) Two-Dimensional Nematic Colloidal Crystals Self-Assembled by Topological Defects. *Science (New York, N.Y.)* 313(5789):954-958.
6. Rahimi M, *et al.* (2015) Nanoparticle self-assembly at the interface of liquid crystal droplets. *Proc. Natl. Acad. Sci.* 112(17):5297-5302.
7. Honglawan A, *et al.* (2015) Synergistic assembly of nanoparticles in smectic liquid crystals. *Soft Matter* 11(37):7367-7375.
8. Rodarte AL, *et al.* (2015) Self-assembled nanoparticle micro-shells templated by liquid crystal sorting. *Soft Matter* 11(9):1701-1707.
9. Milette J, *et al.* (2012) Reversible long-range patterning of gold nanoparticles by smectic liquid crystals. *Soft Matter* 8(24):6593-6598.
10. Ohm C, Brehmer M, & Zentel R (2010) Liquid Crystalline Elastomers as Actuators and Sensors. *Adv. Mater.* 22(31):3366-3387.
11. Yu Y & Ikeda T (2006) Soft Actuators Based on Liquid-Crystalline Elastomers. *Angew. Chem. Int. Ed.* 45(33):5416-5418.
12. White TJ & Broer DJ (2015) Programmable and adaptive mechanics with liquid crystal polymer networks and elastomers. *Nat. Mater.* 14(11):1087-1098.
13. Serra F, *et al.* (2013) Nematic Liquid Crystals Embedded in Cubic Microlattices: Memory Effects and Bistable Pixels. *Adv. Funct. Mater.* 23(32):3990-3994.
14. Musevic I & Zumer S (2011) Liquid crystals: Maximizing memory. *Nat. Mater.* 10(4):266-268.
15. Serra F, *et al.* (2011) Topological defects of nematic liquid crystals confined in porous networks. *Soft Matter* 7(22):10945-10950.
16. Schadt M, Seiberle H, & Schuster A (1996) Optical patterning of multi-domain liquid-crystal displays with wide viewing angles. *Nature* 381(6579):212-215.
17. Onsager L (1949) The Effects of Shape on the Interaction of Colloidal Particles. *Annals of the New York Academy of Sciences* 51(4):627-659.
18. Peter J. Collings JSP (1997) *Handbook of liquid crystal research* (Oxford university press, New York).
19. Frank FC (1958) I. Liquid crystals. On the theory of liquid crystals. *Discuss. Faraday Soc.* 25(0):19-28.
20. Kim YH, Yoon DK, Jeong HS, Lavrentovich OD, & Jung H-T (2011) Smectic Liquid Crystal Defects for Self-Assembling of Building Blocks and Their Lithographic Applications. *Adv. Funct. Mater.* 21(4):610-627.
21. Gennes P-Gd (1974) *The physics of liquid crystals* (Oxford, Clarendon).

22. Wang X, Miller DS, Bukusoglu E, de Pablo JJ, & Abbott NL (2016) Topological defects in liquid crystals as templates for molecular self-assembly. *Nat. Mater.* 15(1):106-112.
23. Theo Rasing IM (2004) *Surfaces and Interfaces of Liquid Crystals* (Springer, Berlin).
24. Warenghem M (1982) A Test for Surface Energy Anisotropy Sign Determination. *Mol. Cryst. Liq. Cryst.* 89(1-4):15-21.
25. Abbott NL (1997) Surface effects on orientation of liquid crystals. *Curr. Opin. Colloid Interface Sci.* 2(1):76-82.
26. Kim J-H, Yoneya M, & Yokoyama H (2002) Tristable nematic liquid-crystal device using micropatterned surface alignment. *Nature* 420(6912):159-162.
27. Martin S, Klaus S, Vladimir K, & Vladimir C (1992) Surface-Induced Parallel Alignment of Liquid Crystals by Linearly Polymerized Photopolymers. *Jpn. J. Appl. Phys.* 31(7R):2155.
28. Martin S, Hubert S, Andreas S, & Stephen MK (1995) Photo-Generation of Linearly Polymerized Liquid Crystal Aligning Layers Comprising Novel, Integrated Optically Patterned Retarders and Color Filters. *Jpn. J. Appl. Phys.* 34(6R):3240.
29. Lee B-w & Clark NA (2001) Alignment of Liquid Crystals with Patterned Isotropic Surfaces. *Science (New York, N.Y.)* 291(5513):2576-2580.
30. Gupta VK & Abbott NL (1997) Design of Surfaces for Patterned Alignment of Liquid Crystals on Planar and Curved Substrates. *Science (New York, N.Y.)* 276(5318):1533-1536.
31. Son J-H, Zin W-C, Takezoe H, & Song J-K (2012) Alignment of Liquid Crystals Using a Molecular Layer with Patterned Molecular Density. *Adv. Mater.* 24(45):6105-6110.
32. Park S, Padeste C, Schiff H, Gobrecht J, & Scharf T (2005) Chemical Nanopatterns via Nanoimprint Lithography for Simultaneous Control over Azimuthal and Polar Alignment of Liquid Crystals. *Adv. Mater.* 17(11):1398-1401.
33. Scharf T, *et al.* (2005) Liquid Crystal Alignment on Chemical Nanopatterns: Control over Azimuthal and Polar Alignment. *Mol. Cryst. Liq. Cryst.* 438(1):55/[1619]-1665/[1629].
34. Lapointe CP, Mason TG, & Smalyukh II (2009) Shape-Controlled Colloidal Interactions in Nematic Liquid Crystals. *Science (New York, N.Y.)* 326(5956):1083-1086.
35. Poulin P, Stark H, Lubensky TC, & Weitz DA (1997) Novel Colloidal Interactions in Anisotropic Fluids. *Science (New York, N.Y.)* 275(5307):1770-1773.
36. Senyuk B, *et al.* (2013) Topological colloids. *Nature* 493(7431):200-205.
37. Sebastián Montiel AR (2009) *Graduate Studies in Mathematics* (American Mathematical Society).
38. Milnor JW (1965) *Topology from the Differentiable Viewpoint* (The University Press of Virginia, Charlottesville).
39. Hopf H (1927) Vektorfelder in n -dimensionalen Mannigfaltigkeiten. *Math. Ann.*

- 96(1):225-249.
40. Cattaneo L, Zhang J, Zuiddam M, Savoini M, & Rasing T (2014) Gaining Control through Frustration: Two-Fold Approach for Liquid Crystal Three-Dimensional Command Layers. *Nano Lett.* 14(7):3903-3907.
 41. Berreman DW (1972) Solid Surface Shape and the Alignment of an Adjacent Nematic Liquid Crystal. *Phys. Rev. Lett.* 28(26):1683-1686.
 42. Stöhr J, *et al.* (2001) Liquid Crystal Alignment on Carbonaceous Surfaces with Orientational Order. *Science (New York, N.Y.)* 292(5525):2299-2302.
 43. Stöhr J, *et al.* (1998) Microscopic Origin of Liquid Crystal Alignment on Rubbed Polymer Surfaces. *Macromolecules* 31(6):1942-1946.
 44. Stöhr J & Samant MG (1999) Liquid crystal alignment by rubbed polymer surfaces: a microscopic bond orientation model. *J. Electron. Spectrosc. Relat. Phenom.* 98-99:189-207.
 45. J. BD, P. CG, & S. Z (2011) *Cross-Linked Liquid Crystalline Systems: From Rigid Polymer Networks to Elastomers* (CRC Press, New York).
 46. de Haan LT, Schenning APHJ, & Broer DJ (2014) Programmed morphing of liquid crystal networks. *Polymer* 55(23):5885-5896.
 47. Küpfer J & Finkelmann H (1991) Nematic liquid single crystal elastomers. *Makromol. Chem. Rapid. Commun.* 12(12):717-726.
 48. Ohm C, Fleischmann E-K, Kraus I, Serra C, & Zentel R (2010) Control of the Properties of Micrometer-Sized Actuators from Liquid Crystalline Elastomers Prepared in a Microfluidic Setup. *Adv. Funct. Mater.* 20(24):4314-4322.
 49. Disch S, Schmidt C, & Finkelmann H (1994) Nematic elastomers beyond the critical point. *Macromol. Rapid Commun.* 15(4):303-310.
 50. Cordoyiannis G, *et al.* (2009) Controlling the Critical Behavior of Paranematic to Nematic Transition in Main-Chain Liquid Single-Crystal Elastomers. *Macromolecules* 42(6):2069-2073.
 51. Naciri J, *et al.* (2003) Nematic Elastomer Fiber Actuator. *Macromolecules* 36(22):8499-8505.
 52. Beyer P, Braun L, & Zentel R (2007) (Photo)crosslinkable Smectic LC Main-Chain Polymers. *Macromol. Chem. Phys.* 208(22):2439-2448.
 53. Krause S, Dersch R, Wendorff JH, & Finkelmann H (2007) Photocrosslinkable Liquid Crystal Main-Chain Polymers: Thin Films and Electrospinning. *Macromol. Rapid Commun.* 28(21):2062-2068.
 54. Ahir SV, Tajbakhsh AR, & Terentjev EM (2006) Self-Assembled Shape-Memory Fibers of Triblock Liquid-Crystal Polymers. *Adv. Funct. Mater.* 16(4):556-560.
 55. Pei Z, *et al.* (2014) Mouldable liquid-crystalline elastomer actuators with exchangeable covalent bonds. *Nat. Mater.* 13(1):36-41.
 56. Mitchell GR & Windle AH (1982) Structural analysis of an oriented liquid crystalline copolyester. *Polymer* 23(9):1269-1272.
 57. Donald AM, Viney C, & Windle AH (1983) Banded structures in oriented thermotropic polymers. *Polymer* 24(2):155-159.
 58. Wei R, He Y, Wang X, & Keller P (2013) Nematic Liquid Crystalline Elastomer Grating and Microwire Fabricated by Micro-Molding in Capillaries. *Macromol.*

- Rapid Commun.* 34(4):330-334.
59. Ohm C, Serra C, & Zentel R (2009) A Continuous Flow Synthesis of Micrometer-Sized Actuators from Liquid Crystalline Elastomers. *Adv. Mater.* 21(47):4859-4862.
 60. Gebhard E & Zentel R (2000) Ferroelectric liquid crystalline elastomers, 1. Variation of network topology and orientation. *Macromol. Chem. Phys.* 201(8):902-910.
 61. Gebhard E & Zentel R (2000) Ferroelectric liquid crystalline elastomers, 2. Variation of mesogens and network density. *Macromol. Chem. Phys.* 201(8):911-922.
 62. Brehmer M, Zentel R, Wagenblast G, & Siemensmeyer K (1994) Ferroelectric liquid-crystalline elastomers. *Macromol. Chem. Phys.* 195(6):1891-1904.
 63. Cui J, *et al.* (2012) Bioinspired Actuated Adhesive Patterns of Liquid Crystalline Elastomers. *Adv. Mater.* 24(34):4601-4604.
 64. Buguin A, Li M-H, Silberzan P, Ladoux B, & Keller P (2006) Micro-Actuators: When Artificial Muscles Made of Nematic Liquid Crystal Elastomers Meet Soft Lithography. *J. Am. Chem. Soc.* 128(4):1088-1089.
 65. Yang H, *et al.* (2009) Micron-Sized Main-Chain Liquid Crystalline Elastomer Actuators with Ultralarge Amplitude Contractions. *J. Am. Chem. Soc.* 131(41):15000-15004.
 66. McConney ME, *et al.* (2013) Topography from Topology: Photoinduced Surface Features Generated in Liquid Crystal Polymer Networks. *Adv. Mater.* 25(41):5880-5885.
 67. Liu D & Broer DJ (2014) Self-assembled Dynamic 3D Fingerprints in Liquid-Crystal Coatings Towards Controllable Friction and Adhesion. *Angew. Chem.* 126(18):4630-4634.
 68. Ware TH, McConney ME, Wie JJ, Tondiglia VP, & White TJ (2015) Voxelated liquid crystal elastomers. *Science (New York, N.Y.)* 347(6225):982-984.
 69. Yu Y, Nakano M, & Ikeda T (2003) Photomechanics: Directed bending of a polymer film by light. *Nature* 425(6954):145-145.
 70. Urayama K, Honda S, & Takigawa T (2006) Deformation Coupled to Director Rotation in Swollen Nematic Elastomers under Electric Fields. *Macromolecules* 39(5):1943-1949.
 71. Zhou Y, *et al.* (2012) Hierarchically Structured Free-Standing Hydrogels with Liquid Crystalline Domains and Magnetic Nanoparticles as Dual Physical Cross-Linkers. *J. Am. Chem. Soc.* 134(3):1630-1641.
 72. Liu D, Bastiaansen CWM, den Toonder JMJ, & Broer DJ (2013) (Photo-)Thermally Induced Formation of Dynamic Surface Topographies in Polymer Hydrogel Networks. *Langmuir* 29(18):5622-5629.
 73. Palleau E, Morales D, Dickey MD, & Velev OD (2013) Reversible patterning and actuation of hydrogels by electrically assisted ionoprinting. *Nat. Commun.* 4.
 74. Kim J, Hanna JA, Byun M, Santangelo CD, & Hayward RC (2012) Designing Responsive Buckled Surfaces by Halftone Gel Lithography. *Science (New York, N.Y.)* 335(6073):1201-1205.

75. Behl M, Kratz K, Noechel U, Sauter T, & Lendlein A (2013) Temperature-memory polymer actuators. *Proc. Natl. Acad. Sci.* 110(31):12555-12559.
76. Pandini S, *et al.* (2015) The two-way shape memory behaviour of crosslinked poly(ϵ -caprolactone) systems with largely varied network density. *J. Intell. Mater. Syst. Struct.*
77. Li J, *et al.* (2011) Superfast-Response and Ultrahigh-Power-Density Electromechanical Actuators Based on Hierarchical Carbon Nanotube Electrodes and Chitosan. *Nano Lett.* 11(11):4636-4641.
78. Li Q, *et al.* (2015) Large-Strain, Multiform Movements from Designable Electrothermal Actuators Based on Large Highly Anisotropic Carbon Nanotube Sheets. *ACS Nano* 9(1):409-418.
79. Kong L & Chen W (2014) Carbon Nanotube and Graphene-based Bioinspired Electrochemical Actuators. *Adv. Mater.* 26(7):1025-1043.
80. de Haan LT, Sánchez-Somolinos C, Bastiaansen CMW, Schenning APHJ, & Broer DJ (2012) Engineering of Complex Order and the Macroscopic Deformation of Liquid Crystal Polymer Networks. *Angew. Chem.* 124(50):12637-12640.
81. Chen M, *et al.* (2011) Photodeformable CLCP material: study on photo-activated microvalve applications. *Appl. Phys. A* 102(3):667-672.
82. Liu C, Qin H, & Mather PT (2007) Review of progress in shape-memory polymers. *J. Mater. Chem.* 17(16):1543-1558.
83. De Gennes P-G, Hébert M, & Kant R (1997) Artificial muscles based on nematic gels. *Macromol. Symp.* 113(1):39-49.
84. Chambers M, *et al.* (2009) Liquid crystal elastomer-nanoparticle systems for actuation. *J. Mater. Chem.* 19(11):1524-1531.
85. Spillmann CM, *et al.* (2007) Stacking nematic elastomers for artificial muscle applications. *Sensors Actuators A: Phys.* 133(2):500-505.
86. Yang L, Setyowati K, Li A, Gong S, & Chen J (2008) Reversible Infrared Actuation of Carbon Nanotube-Liquid Crystalline Elastomer Nanocomposites. *Adv. Mater.* 20(12):2271-2275.
87. Kaiser A, Winkler M, Krause S, Finkelmann H, & Schmidt AM (2009) Magnetoactive liquid crystal elastomer nanocomposites. *J. Mater. Chem.* 19(4):538-543.
88. Courty S, Mine J, Tajbakhsh AR, & Terentjev EM (2003) Nematic elastomers with aligned carbon nanotubes: New electromechanical actuators. *EPL (Europhysics Letters)* 64(5):654.
89. De Gennes P-G (1975) Réflexions sur un type de polymères nématiques. *CR Acad Sci II B* 281:101-103.
90. Lee KM, Koerner H, Vaia RA, Bunning TJ, & White TJ (2010) Relationship between the Photomechanical Response and the Thermomechanical Properties of Azobenzene Liquid Crystalline Polymer Networks. *Macromolecules* 43(19):8185-8190.
91. van Oosten CL, Bastiaansen CWM, & Broer DJ (2009) Printed artificial cilia from liquid-crystal network actuators modularly driven by light. *Nat. Mater.*

- 8(8):677-682.
92. Yamada M, *et al.* (2008) Photomobile Polymer Materials: Towards Light-Driven Plastic Motors. *Angew. Chem. Int. Ed.* 47(27):4986-4988.
 93. Yang Z, *et al.* (2006) Thermal and UV Shape Shifting of Surface Topography. *J. Am. Chem. Soc.* 128(4):1074-1075.
 94. Sánchez-Ferrer A, *et al.* (2009) Photo-Crosslinked Side-Chain Liquid-Crystalline Elastomers for Microsystems. *Macromol. Chem. Phys.* 210(20):1671-1677.
 95. Camacho-Lopez M, Finkelmann H, Palffy-Muhoray P, & Shelley M (2004) Fast liquid-crystal elastomer swims into the dark. *Nat. Mater.* 3(5):307-310.
 96. Yamada M, *et al.* (2009) Photomobile polymer materials-various three-dimensional movements. *J. Mater. Chem.* 19(1):60-62.
 97. Hiscock T, Warner M, & Palffy-Muhoray P (2011) Solar to electrical conversion via liquid crystal elastomers. *J. Appl. Phys.* 109(10):104506.
 98. Li C, Liu Y, Huang X, & Jiang H (2012) Direct Sun-Driven Artificial Heliotropism for Solar Energy Harvesting Based on a Photo-Thermomechanical Liquid-Crystal Elastomer Nanocomposite. *Adv. Funct. Mater.* 22(24):5166-5174.
 99. Yin R, *et al.* (2009) Can sunlight drive the photoinduced bending of polymer films? *J. Mater. Chem.* 19(20):3141-3143.
 100. Camargo CJ, *et al.* (2012) Batch fabrication of optical actuators using nanotube-elastomer composites towards refreshable Braille displays. *J. Micromech. Microeng.* 22(7):075009.
 101. Torras N, *et al.* (2014) Tactile device based on opto-mechanical actuation of liquid crystal elastomers. *Sensors Actuators A: Phys.* 208:104-112.
 102. Liu D, Bastiaansen CWM, den Toonder JMJ, & Broer DJ (2012) Photo-Switchable Surface Topologies in Chiral Nematic Coatings. *Angew. Chem. Int. Ed.* 51(4):892-896.
 103. de Haan LT, *et al.* (2014) Accordion-like Actuators of Multiple 3D Patterned Liquid Crystal Polymer Films. *Adv. Funct. Mater.* 24(9):1251-1258.
 104. Modes CD & Warner M (2011) Blueprinting nematic glass: Systematically constructing and combining active points of curvature for emergent morphology. *Phys. Rev. E* 84(2):021711.
 105. Modes CD, Bhattacharya K, & Warner M (2010) Disclination-mediated thermo-optical response in nematic glass sheets. *Phys. Rev. E* 81(6):060701.
 106. Modes CD & Warner M (2012) The activated morphology of grain boundaries in nematic solid sheets. *Proc. SPIE*, pp 82790Q82791-82798.
 107. Modes CD & Warner M (2012) Responsive nematic solid shells: Topology, compatibility, and shape. *EPL (Europhysics Letters)* 97(3):36007.
 108. Modes CD, Warner M, Sánchez-Somolinos C, de Haan LT, & Broer D (2012) Mechanical frustration and spontaneous polygonal folding in active nematic sheets. *Phys. Rev. E* 86(6):060701.

CHAPTER 2: Fine Golden Rings: Tunable Surface Plasmon Resonance From

Assembled Nanorods in Topological Defects of Liquid Crystals

Elaine Lee, † Yu Xia, † Robert C. Ferrier, Jr., † Hye-Na Kim, Mohamed A. Gharbi, Kathleen J. Stebe, Randall D. Kamien, Russell J. Composto, and Shu Yang, manuscript accepted by Adv. Mater. (2016)

(† These authors contributed equally to this work.)

2.1 Introduction

Control over the assembly of functional, nanostructured materials is an essential ingredient in creating novel, responsive nanodevices. Efforts have focused on the assembly of metal nanoparticles due to their applications in energy harvesting,¹ sensing,² metamaterials,³ and catalysis.⁴ However, because of challenges in achieving dynamic assembly and disassembly of metal nanoparticles on cue through a specific stimulus, the full potential of responsive metal nanoparticle-based devices has yet to be realized. Here, we present a method to direct the assembly of gold nanorods (AuNRs) in liquid crystals (LCs) confined within micropillar arrays by controlling the LC director field to achieve tunable localized surface plasmon resonance (LSPR) properties. The peak absorbance wavelength can be reversibly shifted over a range exceeding 100 nm by varying temperature, an order of magnitude greater than the values reported in literature for AuNR/LC systems. The use of ordered LC disclinations to direct the (dis)assembly of metal nanoparticles, and thus optical properties, offers a new route in the quest for active and highly sensitive plasmonic devices.

Collective oscillations of electrons at the surface of metal nanoparticles interact with light to cause strong resonances in the optical region of the electromagnetic spectrum, known as LSPR. Owing to their shape, AuNRs have two such absorbance bands, a transverse mode (TLSPR) and a longitudinal mode (LLSPR) that depend on the diameter and length of the AuNR, respectively. Furthermore, AuNRs have significantly enhanced electric fields near their tips, making them attractive for use as a sensing platform based on surface enhanced Raman spectroscopy.^{5,6} However, in order to exploit these properties in optical devices, it is essential to control the optical properties of AuNRs, which depend strongly on their assembly. Due to plasmonic coupling, the absorbance of AuNRs significantly changes when they are close to their neighbors. For instance, when two AuNRs align side-by-side, the absorbance band undergoes a blue (hypsochromic) shift, whereas when AuNRs align end-to-end, the absorbance band undergoes a red (bathochromic) shift.⁷ Prior work has investigated controlled assembly of AuNRs in solutions⁸⁻¹⁰ and polymer matrices,^{11, 12} however, these matrices are either unsuitable for devices or cannot be tuned, respectively. Therefore, a more dynamic approach, where reversible assembly and disassembly of AuNRs can be triggered by a specific stimulus, is attractive to realize the full potentials of AuNR-based nanodevices.

LC, an anisotropic soft material, is a promising matrix for the reversible tuning of the AuNR assemblies. The coupling of the optical properties of AuNRs with the spontaneous order-disorder transitions of LCs upon application of external stimuli such as heat, light, and electrical fields will enable the creation of active plasmonic devices. While previous studies have addressed the co-assembly of AuNRs and LCs,¹³⁻²⁰ none have demonstrated direct manipulation of the optical responses of AuNRs by LC phase

transitions or the reversible clustering of nanoparticle ensembles to tune the plasmonic resonance. We have previously shown that stable topological line defects (disclinations) can be formed in nematic LCs (NLCs), such as 4'-n-pentyl-4-cyano-biphenyl (5CB), and used to assemble surface colloids.²¹ In this work, we create disclinations in 4'-n-octyl-4-cyano-biphenyl (8CB) confined between micropillar arrays with tunable size and spacing by precisely controlling the competition between the bend and splay elastic energy, which can be fine-tuned by temperature.²² These disclinations are exploited as elastic scaffolds to sequester AuNRs. The dimensions of the defect structure and consequently, the nanorod assembly can be altered by heating and cooling the LC system, thereby modulating the plasmonic resonance peak. Within arrays of epoxy micropillars with homeotropic anchoring and aspect ratio ($AR = \text{height} / \text{diameter}$) = 1.3, the TLSPR and LLSPR peak shift of PS-functionalized AuNRs (PS-AuNRs) (length = 31 ± 4 nm and diameter = 11.3 ± 1.5 nm) in 8CB are ~ 100 and ~ 150 nm, respectively.

2.2 Experimental methods

2.2.1 Surface functionalization of gold nanorods with polystyrene

Three 40 mL solutions of cetyltrimethylammonium bromide (CTAB, Sigma Aldrich) coated AuNRs in deionized (DI) water were synthesized by a seed-mediated growth method as outlined elsewhere.^{11, 23, 24} Excess CTAB was removed through two washing cycles consisting of centrifugation (20 min at 8,000 RPM, Eppendorf 5804), followed by replacement of the supernatant with approximately 40 mL of Milli-Q water. Following the washing steps, the three AuNR solutions were combined and concentrated in 40 mL of water, providing a stock solution of concentrated AuNRs.

The stock solution of AuNRs (9 mL, 0.4 nM) in DI water was centrifuged (20 min at 8,500 RPM, Eppendorf 5804) and the supernatant was removed so that there was only a small aliquot of concentrated AuNR solution. 30 mg of 5,300 g/mol thiol-terminated polystyrene (HSPS) (Polymer Source) was added to a solution of 10 mL THF until dissolved. Next, the AuNR aliquot was added to the THF/HSPS solution under stirring. The solution was stirred overnight and then solvent exchanged to chloroform twice to remove free HSPS. Finally, AuNRs were suspended in 1 mL of chloroform.

2.2.2 Micropillar fabrication

The epoxy micropillar array was replica molded from a PDMS membrane. Briefly, epoxy precursor (D.E.R. 354, Dow Chemical) was mixed with 3 wt% photoinitiator (Cycracure UVI 6976, Dow Chemical) and cured under UV light (365 nm, Hg lamp) at a dosage of 15,000 mJ/cm². The PDMS mold was then carefully peeled to obtain the epoxy pillars.

2.2.3 Substrate functionalization

To achieve planar anchoring, the epoxy pillars and glass cover slips were treated with UV-ozone Jelight, model 144AX) for 1 h and used immediately. For homeotropic anchoring (i.e., LC molecules vertically aligned to the substrate), silicon tetrachloride (Sigma Aldrich) was evaporated onto the epoxy pillars and glass cover slips in a vacuum dessicator for 10 min following a modified procedure from previously reported literature.²⁵ Then, the substrates were placed into a 65 °C oven with water vapor for 10 min, forming a thin silica film of thickness on the order of tens of Angstroms.²⁵ The substrates were then immersed into a 3 wt% ethanol solution of dimethyloctadecyl[3-(trimethoxysilyl)propyl]ammonium chloride (DMOAP, Sigma Aldrich) for 1 h. They were then washed with DI water 3 times and dried in a 100°C oven.

2.2.4 Assembly of PS-AuNRs in LCs

4'-n-octyl-4-cyano-biphenyl (8CB) (Kingston Chemicals) was added to the chloroform solution of PS-AuNR and ultra-sonicated for dispersion. The chloroform was then evaporated using a vacuum oven at room temperature. The suspension was heated to 45 °C (above the nematic-isotropic transition temperature, T_{NI}) and drop cast over the surface-treated epoxy pillars. A surface-treated glass cover slip was used to close the LC cell with no spacer. The cell thickness is the height of the micropillars (13 μm).

2.2.5 Characterization

Transmittance of the AuNR and PS-AuNR suspensions as synthesized were measured using the Cary 5000 UV-Vis-NIR spectrophotometer (Agilent Technologies). The LC cell was mounted on a Mettler FP82 hot stage equipped with FP 90 controller and heated at 45 °C for 5 min to reach the isotropic phase. It is then cooled down to 25°C at a rate of 10 °C min^{-1} to form the smectic-A (SmA) phase. In parallel to the heating and cooling cycle, the LC textures were observed under the Olympus BX61 motorized optical microscope with crossed polarizers using CellSens software. Alternatively, the transmission of the LC cell was measured using a custom-built spectrophotometer with a fiber-coupled tungsten-halogen light source and a USB4000 detector (Ocean Optics).

2.3 Optical properties of gold nanorods

The functionalization of the AuNRs with PS is detailed in Figure 2.1. As-synthesized PS-AuNRs displayed two characteristic extinction bands at 512 nm (transverse band) and 727 nm (longitudinal band) in water, as can be seen in Figure 2.1b. The longitudinal band underwent a slight bathochromic (red) shift to 742 nm after

AuNRs are functionalized with HSPS and solvent exchanged to chloroform, as seen in Figure 2.1c. Finally, PS-AuNRs were characterized via SEM (Figure 2.1d) with length of 314 nm and diameter of 11.3 ± 1.5 nm.

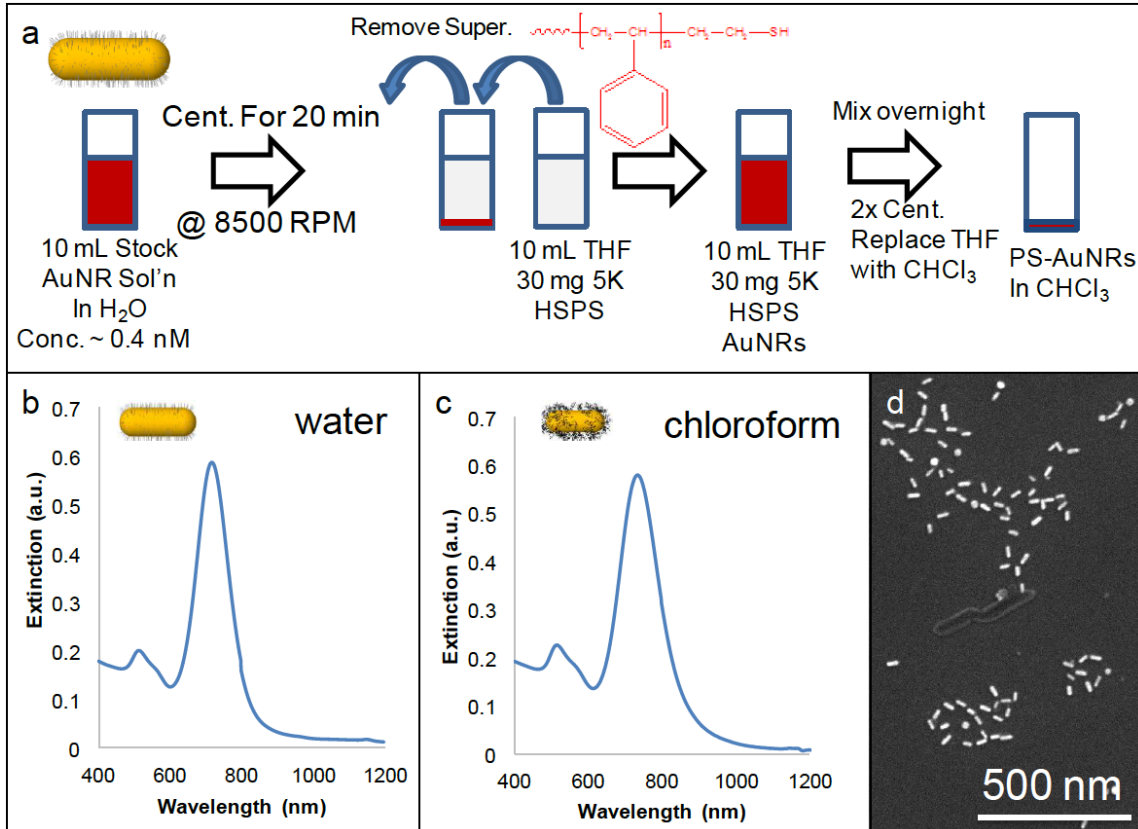


Figure 2.1 (a) Schematic detailing the functionalization of AuNRs with polystyrene brushes. (b-c) Extinction spectra of (b) AuNRs in water and (c) PS-AuNRs in chloroform. (d) SEM image of PS-AuNRs.

2.4 Control of liquid crystal surface anchoring

NLCs in homeotropic anchoring micropillar arrays orientate in a pure splay and bend configuration with no twist distortions.²¹ The elastic energy of distortions in an LC system is given by the Frank-Oseen free energy density:

$$f = \frac{1}{2} \{ K_1 (\nabla \cdot \mathbf{n})^2 + K_2 (\mathbf{n} \cdot \nabla \times \mathbf{n})^2 + K_3 [(\mathbf{n} \cdot \nabla) \mathbf{n}]^2 \} \quad (2-1)$$

where K_1 , K_2 , and K_3 are the splay, twist, and bend elastic constants and \mathbf{n} is the LC director. Therefore, the positions of the defects with respect to the micropillars, *i.e.* the defect sizes, are dictated by the elastic energy of the splay and bend configurations, as quantified by K_1 and K_3 , respectively.²² Here, we choose 8CB, which displays a nematic phase from 33.5°C to 40.5°C and a smectic phase from 21.5°C to 33.5°C, over conventional NLCs such as 5CB as the LC matrix because its elastic constants are more temperature sensitive than those of 5CB.²² With decreasing temperature, K_3 of 8CB increases faster than the K_1 such that K_3/K_1 approaches ∞ as T approaches the nematic-smectic phase transition temperature (T_{NS}). Thus, in order to balance the elastic energy of the system, LC molecules prefer to splay rather than bend at a lower temperature, leading to a larger defect ring size (Figure 2.2a). The defect radius increased from $6.5 \pm 0.1 \mu\text{m}$ at 38 °C (Figure 2.2b) to a maximum of $11.3 \pm 0.2 \mu\text{m}$ at 34 °C (Figure 2.2f), at which the neighboring defects compress against each other, forming an array of square rings surrounding the pillars.

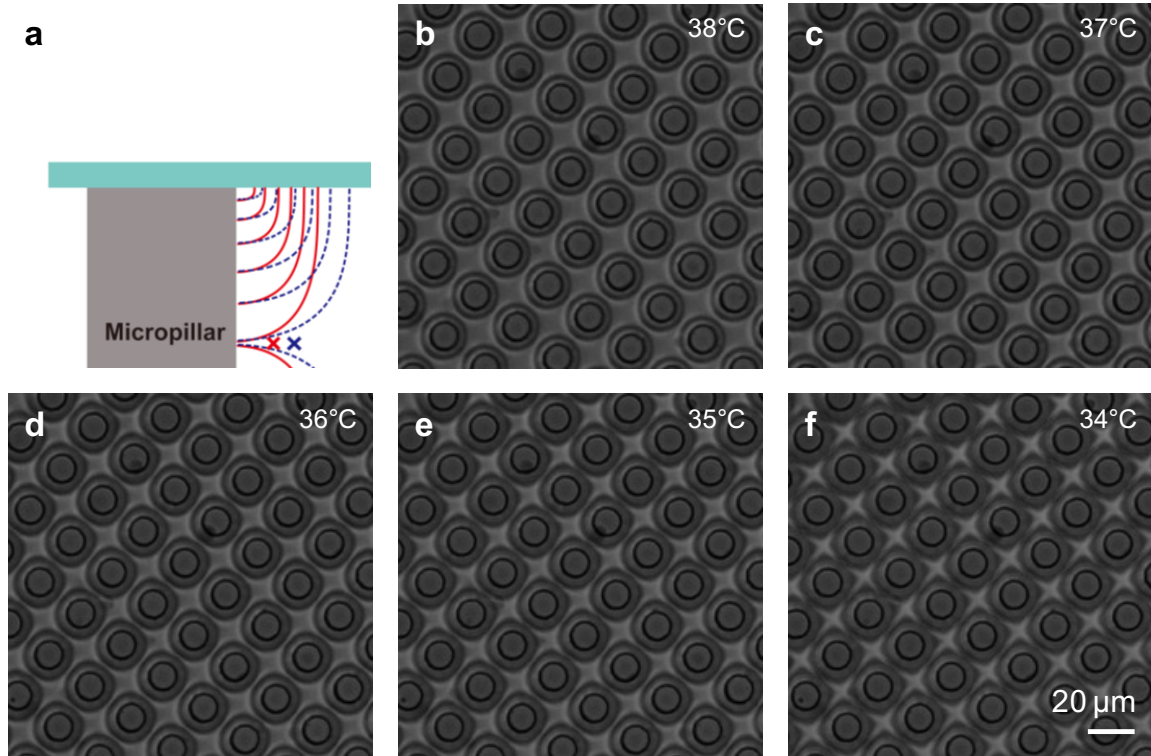


Figure 2.2 (a) Schematic of the side view of the temperature sensitive disclination ring confined to a micropillar. The red solid line and blue dotted line represent the LC director field at high and low temperatures, respectively. The red and blue crosses illustrate the position of the defect at high and low temperatures, respectively. (b-f) Bright field images of 8CB in homeotropic pillar arrays in the nematic phase, at temperatures indicated at the top right corner of each image. The circles surrounding the micropillars originate from light scattering by LC bulk disclinations. Scale bar applies to all figures.

The disclinations appeared in the form of bright lines encircling the micropillars when observed under crossed polarizers (Figure 2.3a-f). Outside these bright lines, the entire region was dark even under sample rotation due to complete homeotropic anchoring on all surfaces. As the sample was further cooled, 8CB transitioned into the smectic phase at ~ 33.5 °C. 8CB appeared dark between the nearest neighboring micropillars with Maltese cross patterns between the next-nearest neighboring pillars under polarized optical microscopy (POM) (Figure 2.3g-h).

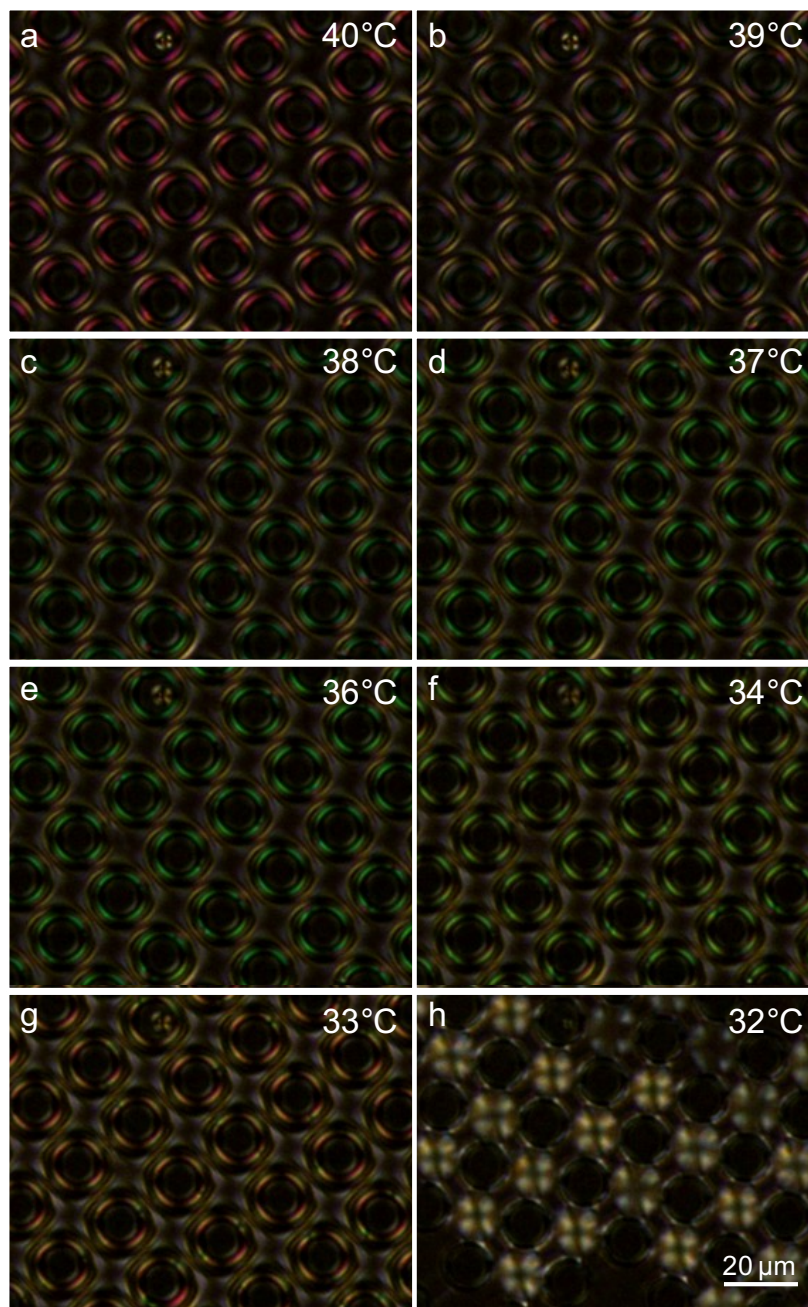


Figure 2.3 POM images of 8CB over homeotropic anchoring epoxy pillar arrays at various temperatures. Pillar dimensions are diameter = 10 μm , spacing = 10 μm , and aspect ratio (height/diameter) = 1.3. The temperature is indicated in the top right corner of each image. Scale bar applies to all figures.

2.5 Optical response of AuNRs

Armed with the understanding of the temperature-sensitive disclinations in 8CB, PS-functionalized AuNRs (PS-AuNRs) were added to the LC system (See Experimental methods). Homeotropic or planar anchoring was imposed on all surfaces of the fabricated epoxy micropillars (diameter = 10 μ m, pitch = 20 μ m, AR = 1.3) as well as the glass cover slip. PS-AuNRs dispersed in 8CB, were sandwiched between the surface-functionalized pillars and a glass cover slip to form a LC cell (Figure 2.4). The cell was heated to 45°C, above the clearing temperature 40.5°C, to the isotropic phase and subsequently cooled to the nematic phase. At least two heating and cooling cycles were performed to clear the thermal history.

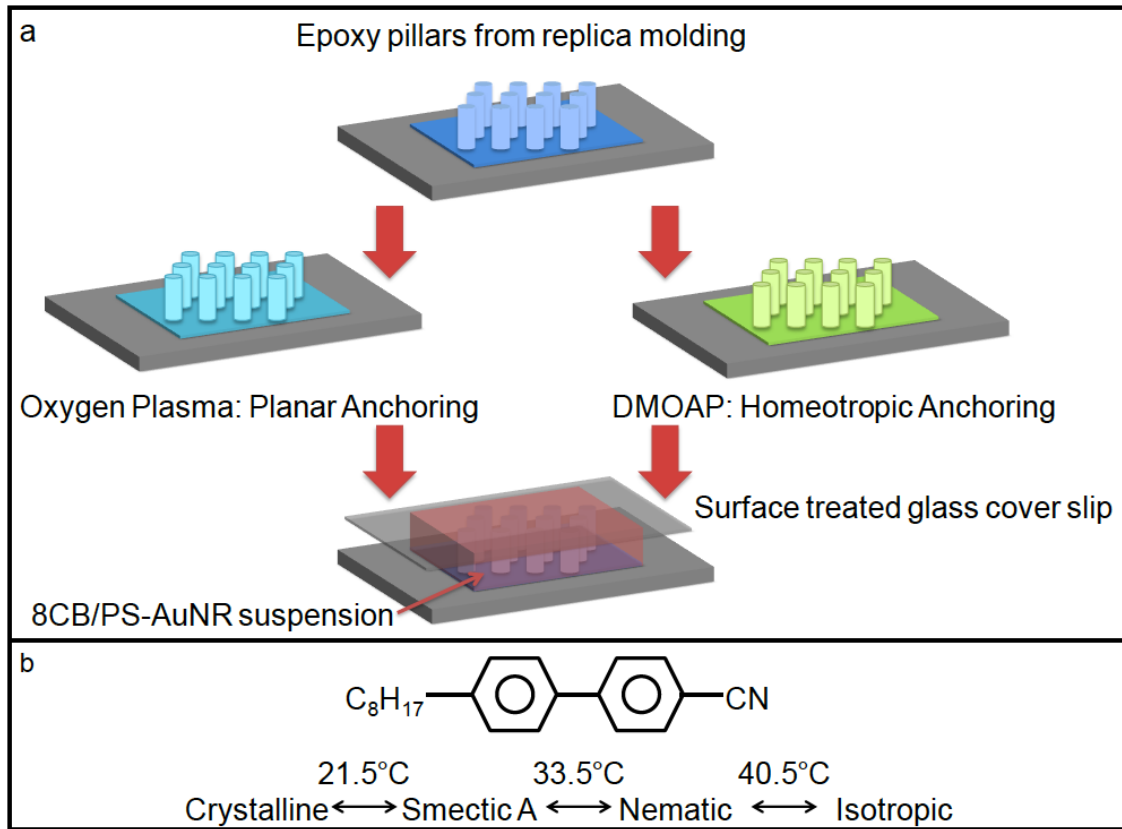


Figure 2.4 Illustration of LC cell. (a) Schematic of the substrate functionalization; (b) Chemical structure and phase transition temperature of 8CB.

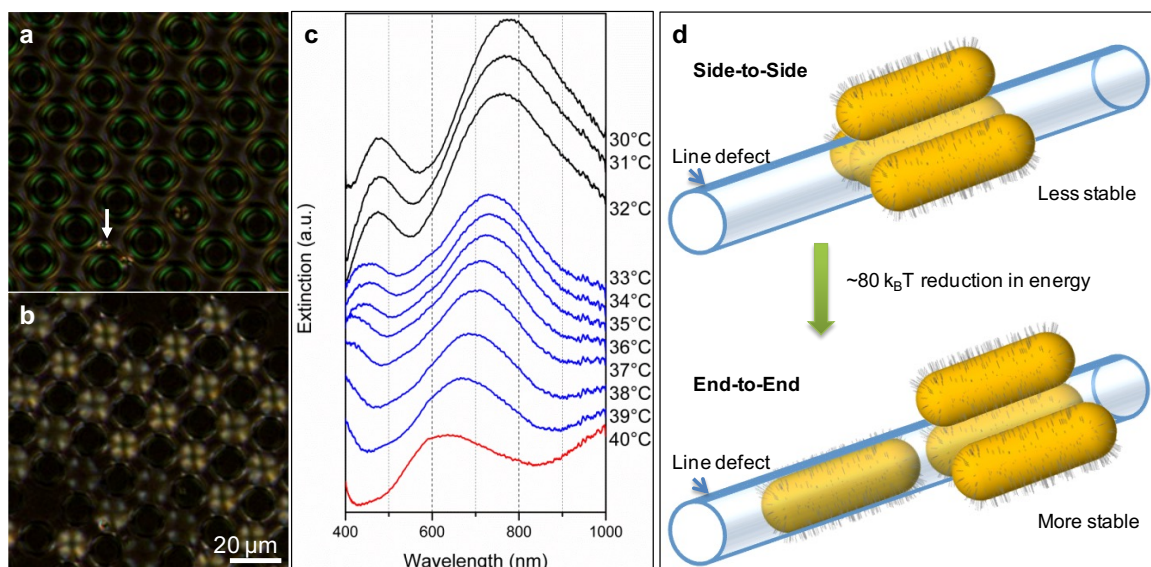


Figure 2.5 POM images of functionalized gold nanorods in 8CB over homeotropic anchoring epoxy pillar arrays at (a) 35°C (nematic) and (b) 30°C (smectic). White arrow indicates the assembly of gold nanorods. Pillar dimensions are diameter = 10 μm , spacing = 10 μm , and aspect ratio (height/diameter) = 1.3. Scale bar applies to all figures. (c) Extinction spectra of gold nanorods in 8CB over homeotropic anchoring epoxy pillars. The extinction is offset for clarity. Red, blue, and black colors indicate isotropic, nematic, and smectic phase, respectively. (d) Schematic of the gold nanorods assembled side-by-side (top) and end-to-end within the LC defect core.

The transmission of PS-AuNRs in 8CB between micropillars with homeotropic anchoring was measured as the sample was cooled from the isotropic phase. The spectra were normalized and subtracted from 1 to calculate extinction and offset for visualization (Figure 2.5c). At $\sim 40^\circ\text{C}$, 8CB was in the isotropic phase and an absorbance peak attributed to the PS-AuNRs could be observed at $\sim 636\text{ nm}$. We hypothesize that this peak is the LLSPR, which has blue-shifted ($\sim 110\text{ nm}$) compared to PS-AuNRs in chloroform. This indicates that the rods are compressed side-to-side by the phase boundaries during the multiple heating and cooling cycles. Due to their anisotropic shapes, rods under compression favor side-to-side to maximize translational entropy at the loss of rotational

entropy. Such packing behavior has been theoretically predicted by Onsager's theory of nematic ordering²⁶, and experimentally confirmed in many rod-like systems.^{8, 27-29}

At 38°C, 8CB is in the nematic phase and the LLSPR red shifted to ~683 nm. The red shifting of plasmon peaks observed in the system is believed to be closely related to the change of the coupling effect between neighboring PS-AuNRs during the cooling process. As the system is cooled from the isotropic to the nematic phase, the PS-AuNRs are swept into the first-order isotropic-nematic phase transition boundaries, which evolve into defect lines in the nematic system.³⁰ Such sweeping behavior has been previously reported for micro- and nanoparticles in LCs.^{21, 30} PS-AuNRs in the nematic phase prefer to migrate to the disclinations to minimize the free energy of the LC system by replacing the energetically costly regions of the distorted director field and the “melted” isotropic defect cores in the disclinations.¹⁷ The total energy of a $-1/2$ disclination can be expressed as eq. (2-2)

$$W = \frac{\pi}{4} K L \ln\left(\frac{R}{r_{dc}}\right) + \gamma V_r \quad (2-2)$$

where $K = 10$ pN is the average elastic constant, L is the disclination length, R is the characteristic dimension of the considered system, $r_{dc} \sim 10$ nm is the size of the defect core, $\gamma \approx 10^5$ J/m³ is the core energy density, and V_r is the volume of the defect core.³¹ Accordingly, we estimate the chemical potential of each PS-AuNRs to be ~100 k_BT, a large driving force for PS-AuNR trapping. The PS-AuNR is considered fully trapped in the defect core since the size of the PS-AuNR is similar to r_{dc} and, once trapped, PS-AuNRs tend to align with the direction of the disclination to maximize the displaced

volume of the defect core. However, to determine whether the PS-AuNR ensembles align end-to-end or side-to side, we need to consider the contribution of elastic energy from the LCs since the cluster size is much greater than the defect core size.

As mentioned above, the PS-AuNRs are compressed side-to-side in the isotropic phase. When these compressed clusters are trapped in the disclinations in the nematic phase, their chemical potential becomes a function of the size of the clusters, *i.e.* the number of PS-AuNRs in the cluster, n . If the number of the PS-AuNRs in the cluster is greater than 2, only one PS-AuNR can be effectively trapped in the defect core, while others will replace the distorted director field near the defect core (Figure 2.5d, top). The elastic energy of the distorted field of LC that is replaced by PS-AuNRs, W_{el} , can be estimated by

$$W_{el} \sim nKR_{eq} \quad (2-3)$$

where R_{eq} is the “equivalent” radius of a sphere that has the same volume of a single NR, ~ 8 nm in our system. Therefore, the replacement energy of the distorted director field is ~ 20 $k_B T$ for each PS-AuNR. This energy is much smaller than the replacement energy of the defect core (~ 100 $k_B T$); it will be energetically favorable for the side-to-side aligned PS-AuNR clusters to disassemble into single rods and align end-to-end in the defect core to maximize their occupancy in the defect core of the disclination (Figure 2.5d, bottom) as the system enters the nematic phase. As the defect rings increase in size when temperature is decreased, more PS-AuNR clusters decompress, resulting in a continuing red-shift in the plasmon resonance peak (Figure 2.5c and 2.6). At 36°C, two peaks could

be observed at ~ 414 nm and 712 nm, corresponding to the transverse LSPR (TLSPR) and longitudinal LSPR (LLSPR), respectively. As the sample was further cooled through the nematic phase to 33°C , the TLSPR and LLSPR peaks further red shifted to 453 nm and 729 nm, respectively. The latter is close to the LLSPR of the PS-AuNRs in chloroform (742 nm), indicating a similar loose dispersion within the defect core.

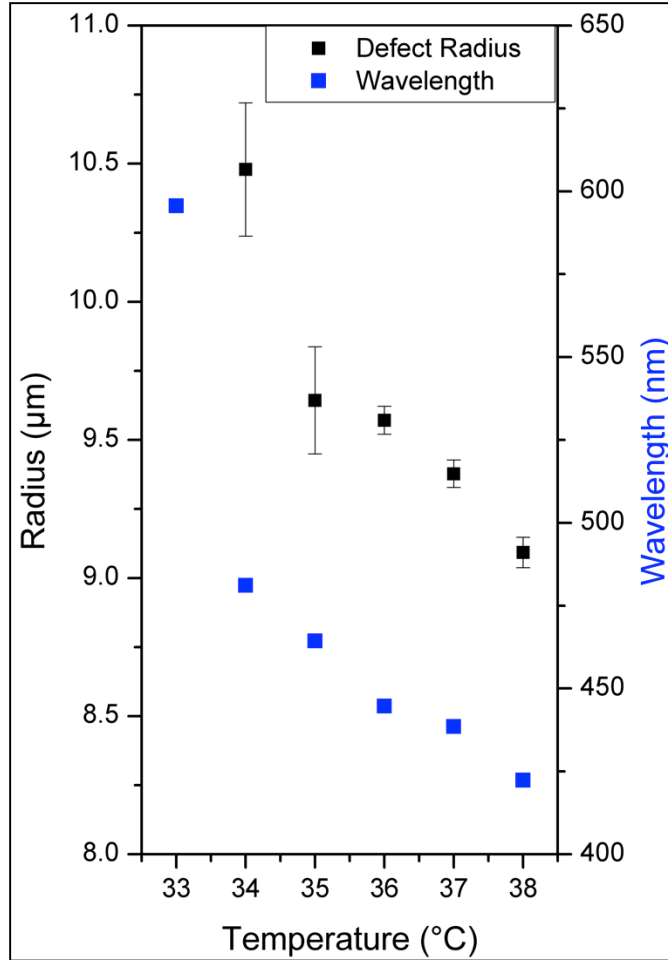


Figure 2.6 The defect radius of 8CB in the nematic phase and TLSPR wavelength of the PS-AuNRs over epoxy pillars as a function of temperature.

As the sample transitioned to the smectic phase at 32°C , the plasmon peaks further red shifted to 483 nm and 789 nm, respectively, but minimal shift was observed as the sample was cooled through the smectic phase to room temperature. Transitioning

from the nematic to the smectic, the rods were attracted to and eventually trapped by the defect cores of the focal conic domains (FCDs) at the center-point between four pillars. We have reported such interactions of nanoparticles within FCDs previously.³² Cooling from $\sim 40^\circ\text{C}$ to $\sim 30^\circ\text{C}$, the overall peak shifts for the TLSPR and LLSPR are 101 and 153 nm, respectively, which is one order of magnitude higher than those reported in literature, typically on the order of 10 nm based on the refractive index change of LC over metal nanoparticle arrays deposited on a surface.^{13-15, 33} We attribute the significant plasmonic peak shift to the dynamic interaction between the PS-AuNRs and the highly ordered LC defect structures. We note that it is reversible during heating/cooling cycles.

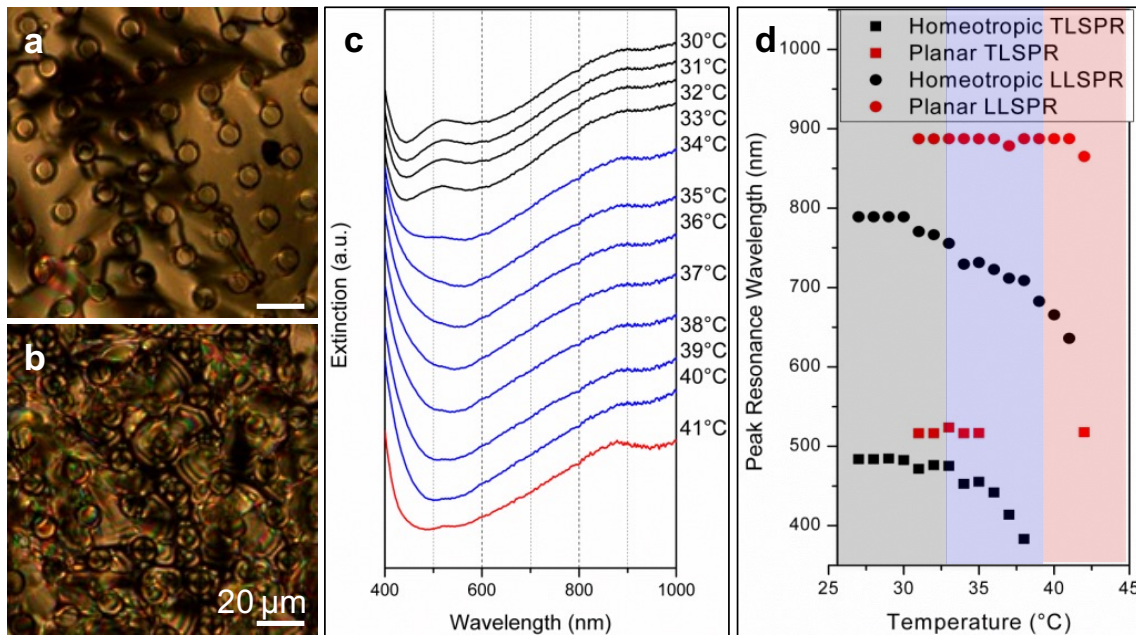


Figure 2.7 POM images of functionalized gold nanorods in 8CB over planar anchoring epoxy pillar arrays at (a) 35°C (nematic) and (b) 30°C (smectic). Pillar dimensions are diameter = $10\ \mu\text{m}$, spacing = $10\ \mu\text{m}$, and aspect ratio (height/diameter) = 1.3. Scale bar applies to all figures. (c) Extinction spectra of gold nanorods in 8CB over planar anchoring epoxy pillars. The extinction is offset for clarity. Red, blue, and black colors indicate isotropic, nematic, and smectic phase, respectively. (d) The transverse (T) and longitudinal (L) localized surface plasmonic resonance peak (LSPR) position as a function of temperature for both homeotropic and planar cells.

Homeotropic anchoring of 8CB on the pillars and on the top and bottom LC cell surfaces is critical to the LC disclination ring formation and thus, the giant peak shift of LSPR. Supporting this, we found the defects between micropillar arrays with planar anchoring were highly disordered in both the nematic and smectic phases (Figure 2.7a-b). In this setting, when 8CB was in the isotropic phase at 40°C, weak extinction peaks were observed at ~516 and 887 nm (Figure 2.7c). These peaks correspond to the TLSPR and LLSPR of the PS-AuNRs, respectively, which showed insignificant peak shifts upon cooling to the nematic phase. Since no bulk disclinations are topologically required in the planar cell, we attribute this weak response to the disordered defect structure of the planar cell, which can cause random distribution of the PS-AuNRs within the LC structure. Nanorod aggregation, as evidenced by the broadening of the LSPR peaks, during the isotropic-nematic phase transition may also play a role. Such aggregation is different from the clustering in the homeotropic cell, as bulk disclinations in the planar cell are unstable so they tend to be released and diminished from the NLC. These diminishing disclinations can sweep nanorods into a higher-density aggregation (Figure 2.7a-b). In the smectic phase, peaks remained at the same positions with slightly higher intensity, which could be attributed to the higher order of the smectic phase. These results from the planar cell were in sharp contrast to those from the homeotropic anchoring cell (Figure 2.7d). This result underscores the importance of well-controlled anchoring conditions of all the boundary surfaces of the LC to direct the assembly and optical response of PS-AuNRs in the LC defect structures.

To further demonstrate the importance of the defect ring structure surrounding the micropillar array in assembling the PS-AuNRs, we fabricated a LC cell consisting of two

flat glass slides treated with homeotropic anchoring. In Figure 2.8, no plasmon peaks were observed when dispersing PS-AuNRs into the LC cell. In POM images, aggregation of the rods was observed when cooling the sample from the isotropic phase to the nematic phase transition, which could again be attributed to the diminishing disclinations during the isotropic to nematic phase transition.

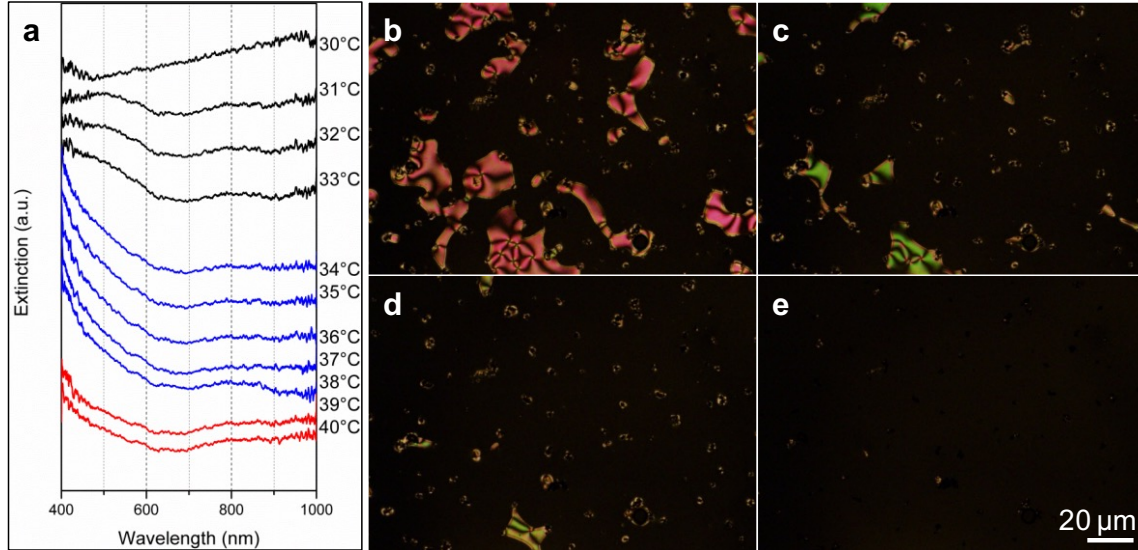


Figure 2.8 (a) Extinction spectra of PS-AuNRs in 8CB sandwiched between two glass slides with homeotropic anchoring. The extinction is offset for clarity. Red, blue, and black colors indicate isotropic, nematic, and smectic phase, respectively. (b-e) POM images of PS-AuNRs in 8CB in a homeotropic flat cell; the sample is transitioning from the nematic to the smectic phase from b to e.

2.6 Conclusions

In summary, PS-AuNRs were trapped into the LC defect cores of 8CB on surface-treated epoxy pillar arrays. Comparison of different surface treatments showed that homeotropic anchoring induces a red plasmon peak shift as the sample was cooled and the LC transitioned from the isotropic to the nematic to the smectic phase sequentially. We attribute this much enhanced shift to the formation of well-ordered distortions and defects surrounding the pillars. In contrast, random defect structures were formed

surrounding planar anchored pillars, resulting in indistinguishable plasmon peaks with no peak shift as the sample is cooled. Dispersing PS-AuNRs in LCs in a flat homeotropic cell induced rod aggregation and a suppression of the plasmon resonance response. The assembly and actuation of PS-AuNRs demonstrated is achieved through several factors, including 1) the surface functionalization of AuNRs with PS brushes, which allowed for nanorod dispersion in 8CB without aggregation, 2) the periodic arrangement of the surface topography at the microscale, 3) the manipulation of LC surface anchoring through surface functionalization and geometry to form well-ordered defect structures, and 4) the reversible compression/relaxation of the LC director field tuned by temperature. Here, we have demonstrated unprecedented, *reversible*, and *dynamic control* over the assembly of AuNRs, leading to very large shift of absorbance peak, an order of magnitude greater than any previous work with AuNR composites. Importantly, we show that the LC director field is dynamically tuned in the nanoscale using microscale confinement through the interplay of elastic energy of the splay and bend configurations in LC at different temperatures, thus, fine-tuning its core replacement energy to reversibly sequester nanoscale inclusions at the microscale. We believe the use of an anisotropic soft matter such as LC and insights into the manipulation of their defect structures will open doors to direct the (dis)assembly of nano-objects for unique optical and thermal properties.

2.7 Contributions

E.L., Y.X., and S.Y. conceived the idea of studying AuNR assemblies in the LC defect rings. Y.X. and M.A.G. designed the experiments and performed simulation of LC assemblies in micropillar arrays. E.L. and H.K. performed PS-AuNR assemblies in

LC/micropillar experiments. R.C.F. performed gold nanorod synthesis and functionalization. R.D.K., K.J.S., R.J.C., and S.Y. supervised the work. E.L., Y.X., R.C.F., R.D.K., K.J.S., R.J.C., and S.Y. wrote the paper. All the authors commented on the paper.

2.8 References

1. Karker N, Dharmalingam G, & Carpenter MA (2014) Thermal Energy Harvesting Plasmonic Based Chemical Sensors. *ACS Nano* 8(10):10953-10962.
2. Gormley AJ, Chapman R, & Stevens MM (2014) Polymerization amplified detection for nanoparticle-based biosensing. *Nano Lett.* 14(11):6368-6373.
3. Young KL, *et al.* (2014) Using DNA to Design Plasmonic Metamaterials with Tunable Optical Properties. *Adv. Mater.* 26(4):653-659.
4. Zhou J, *et al.* (2014) Interfacial Assembly of Mussel-Inspired Au@Ag@Polydopamine Core–Shell Nanoparticles for Recyclable Nanocatalysts. *Adv. Mater.* 26(5):701-705.
5. Nikoobakht B & El-Sayed MA (2003) Surface-Enhanced Raman Scattering Studies on Aggregated Gold Nanorods†. *J. Phys. Chem. A* 107(18):3372-3378.
6. Qian X, Li J, & Nie S (2009) Stimuli-Responsive SERS Nanoparticles: Conformational Control of Plasmonic Coupling and Surface Raman Enhancement. *J. Am. Chem. Soc.* 131(22):7540-7541.
7. Funston AM, Novo C, Davis TJ, & Mulvaney P (2009) Plasmon Coupling of Gold Nanorods at Short Distances and in Different Geometries. *Nano Lett.* 9(4):1651-1658.
8. Nie Z, *et al.* (2007) Self-assembly of metal-polymer analogues of amphiphilic triblock copolymers. *Nat. Mater.* 6(8):609-614.
9. Sethi M, Joung G, & Knecht MR (2009) Linear Assembly of Au Nanorods Using Biomimetic Ligands. *Langmuir* 25(3):1572-1581.
10. Zhao D, Zhang Z, Wen Y, Zhang X, & Song Y (2013) Reversible gold nanorod assembly triggered by pH-responsive DNA nanomachine. *Appl. Phys. Lett.* 102(12):123101.
11. Ferrier RC, Jr., *et al.* (2014) Gold nanorod linking to control plasmonic properties in solution and polymer nanocomposites. *Langmuir* 30(7):1906-1914.
12. Hore MJA & Composto RJ (2010) Nanorod Self-Assembly for Tuning Optical Absorption. *ACS Nano* 4(11):6941-6949.
13. De Sio L, *et al.* (2012) Double active control of the plasmonic resonance of a gold nanoparticle array. *Nanoscale* 4(24):7619-7623.
14. De Sio L, *et al.* (2013) All-optical control of localized plasmonic resonance realized by photoalignment of liquid crystals. *J. Mater. Chem. C* 1(45):7483-7487.
15. Hsiao VK, Zheng YB, Juluri BK, & Huang TJ (2008) Light - driven plasmonic switches based on Au nanodisk arrays and photoresponsive liquid crystals. *Adv. Mater.* 20(18):3528-3532.

16. Liu Q, *et al.* (2010) Self-Alignment of Plasmonic Gold Nanorods in Reconfigurable Anisotropic Fluids for Tunable Bulk Metamaterial Applications. *Nano Lett.* 10(4):1347-1353.
17. Senyuk B, *et al.* (2012) Shape-Dependent Oriented Trapping and Scaffolding of Plasmonic Nanoparticles by Topological Defects for Self-Assembly of Colloidal Dimers in Liquid Crystals. *Nano Lett.* 12(2):955-963.
18. Umadevi S, Feng X, & Hegmann T (2013) Large Area Self-Assembly of Nematic Liquid-Crystal-Functionalized Gold Nanorods. *Adv. Funct. Mater.* 23(11):1393-1403.
19. Liu Q, *et al.* (2014) Shape-dependent dispersion and alignment of nonaggregating plasmonic gold nanoparticles in lyotropic and thermotropic liquid crystals. *Phys. Rev. E* 89(5):052505.
20. Liu Q, Yuan Y, & Smalyukh II (2014) Electrically and Optically Tunable Plasmonic Guest-Host Liquid Crystals with Long-Range Ordered Nanoparticles. *Nano Lett.* 14(7):4071-4077.
21. Cavallaro M, *et al.* (2013) Exploiting imperfections in the bulk to direct assembly of surface colloids. *Proc. Nat. Acad. Sci. U. S. A.* 110(47):18804-18808.
22. Lopez-Leon T, Fernandez-Nieves A, Nobili M, & Blanc C (2011) Nematic-Smectic Transition in Spherical Shells. *Phys. Rev. Lett.* 106(24):247802.
23. Nikoobakht B & El-Sayed MA (2003) Preparation and Growth Mechanism of Gold Nanorods (NRs) Using Seed-Mediated Growth Method. *Chem. Mater.* 15(10):1957-1962.
24. Sau TK & Murphy CJ (2004) Seeded High Yield Synthesis of Short Au Nanorods in Aqueous Solution. *Langmuir* 20(15):6414-6420.
25. Klaus JW & George SM (2000) SiO₂ Chemical Vapor Deposition at Room Temperature Using SiCl₄ and H₂O with an NH₃ Catalyst. *J. Electrochem. Soc.* 147(7):2658-2664.
26. Onsager L (1949) THE EFFECTS OF SHAPE ON THE INTERACTION OF COLLOIDAL PARTICLES. *Ann. N. Y. Acad. Sci.* 51(4):627-659.
27. Lekkerkerker HNW & Vroege GJ (2013) Liquid crystal phase transitions in suspensions of mineral colloids: new life from old roots. *Phil. Trans. R. Soc. London A* 371(1988):20120263.
28. Chen H, Shao L, Li Q, & Wang J (2013) Gold nanorods and their plasmonic properties. *Chem. Soc. Rev.* 42(7):2679-2724.
29. Zhang S-Y, Regulacio MD, & Han M-Y (2014) Self-assembly of colloidal one-dimensional nanocrystals. *Chem. Soc. Rev.* 43(7):2301-2323.
30. Rodarte AL, *et al.* (2015) Self-assembled nanoparticle micro-shells templated by liquid crystal sorting. *Soft Matter* 11(9):1701-1707.
31. Lubensky TC, Pettey D, Currier N, & Stark H (1998) Topological defects and interactions in nematic emulsions. *Phys. Rev. E* 57(1):610-625.
32. Honglawan A, *et al.* (2015) Synergistic assembly of nanoparticles in smectic liquid crystals. *Soft Matter* 11(37):7367-7375.
33. Dickson W, Wurtz GA, Evans PR, Pollard RJ, & Zayats AV (2008) Electronically Controlled Surface Plasmon Dispersion and Optical Transmission through Metallic Hole Arrays Using Liquid Crystal. *Nano Lett.* 8(1):281-286.

CHAPTER 3: Direct Mapping of Local Director Field of Nematic Liquid Crystals at the Nanoscale

Adapted from:

Xia, Y., Serra, F., Kamien, R. D., Stebe, K. J., and Yang, S., (2015), Direct mapping of local director field of nematic liquid crystals at the nanoscale. *Proc. Nat. Acad. Sci. USA*, PNAS 2015 112 (50) 15291-15296, doi: 10.1073/pnas.1513348112. Reproduced with permission.

3.1 Introduction

Ubiquitous as they are, it sometimes escapes our attention that liquid crystals (LCs) are the original nanomaterial. The manipulation of these nanometer-size molecules into coherent, centimeter-scale structures is now routine. Though we have become adept at deducing textures indirectly through optical microscopies¹⁻⁵, probing the molecular-scale organization requires either a glassy material or rapid cooling of samples providing metastable states that can be directly visualized through scanning electron microscopy (SEM), transmission electron microscopy (TEM), and atomic force microscopy (AFM)⁶⁻⁸. Although these techniques are effective to study a variety of more complex LC phases including smectic LCs^{6,7,9}, cholesteric and blue phases¹⁰, and biological LC polymers^{11,12}, non-glassy, low molecular weight nematic LCs (NLCs) reorient during fast freezing. Polymer nematics can be quenched into metastable states but organization of static configurations through surface alignment is difficult. Flow alignment can be employed

but that often precludes complex, molecular scale patterning of the boundary conditions, essential for controlling and manipulating topological defects^{13, 14}. While an undesired nuisance in NLC displays, topological defects mediate many of the rich interactions between colloids in NLCs¹⁵. The defects, bearing quantized topological charge, resemble the defects in superconductors¹⁶, soft ferromagnets¹⁷, and even cosmic strings and monopoles¹⁸. The fluidity of the phase and the weakly first-order nematic-isotropic phase transition allows for direct visualization of the creation/annihilation of defects *via* the Kibble-Zurek mechanism¹⁹. Further, defects in a flat sheet of nematic gel or glass can be utilized to bend or twist local directors, inducing three-dimensional shapes^{20, 21}. It is therefore critical to be able to characterize the defect structures at the nanoscale in a variety of settings. Here, we report the design and synthesis of a nematic liquid crystal monomer (LCM) system that has strong homeotropic anchoring on silica surfaces and does not reorient its director field during polymerization. Thus, the optical signatures remain unchanged in the liquid crystal polymers (LCPs), allowing for direct visualization of the defect structures by SEM in real-space with 100 nm resolution. Using this technique, we study the nematic textures in more complex LC/colloidal systems and estimate the ratio between elastic and anchoring constant, i.e. the extrapolation length, of LCM.

3.2 Experimental methods

3.2.1 Materials

All chemicals were used without further purification. Dimethylformamide (DMF), dichloromethane (DCM), potassium hydroxide (KOH), sodium thiosulfate pentahydrate,

and hydrochloric acid (HCl) were purchased from Fisher Scientific. Thionyl chloride (SOCl₂), 4-dimethylaminopyridine (DMAP), 2-nitroterephthalic acid, 4-hydroxybenzoic acid, meta-chloroperoxybenzoic acid (MCPBA), (3-Aminopropyl) triethoxysilane (APTES), allyl alcohol and (±)-glycidol were purchased from Sigma Aldrich. 4-Cyano-4'-pentylbiphenyl (5CB) was purchased from Kingston Chemicals Limited. Polyimide (Durimide 32A) was purchased from Arch Chemicals, Inc. Liquid crystal monomers, 4-ethoxy-4'-(6-acryloyloxyhexyloxy) azobenzene (LCM_AZO) was kindly provided by U.S. Air Force Research Laboratory, and RM257 was obtained from Merck.

3.2.2 Synthesis of Liquid Crystal Monomers

Chemical structures are illustrated in Figure 3.3, and ¹H-NMR spectra are shown in Figure 3.4.

2-Nitro terephthaloyl dichloride(1). 4.22 g 2-nitroterephthalic acid (20 mmol) was mixed with 20 mL thionyl chloride under stirring. Two drops of DMF were added as catalyst. The mixture was heated to 75°C and refluxed until no bubbles were generated from the solution. The reaction mixture was then cooled down to room temperature, and excess thionyl chloride was removed *in vacuo*. The crude 2-nitro terephthaloyl dichloride was obtained as an orange oil and used in the next step without further purification.

2-Nitro, 1,4-benzenedicarboxylic acid, 1,4-bis(4-carboxyphenyl) ester(2). 3.45 g 4-hydroxybenzoic acid (25 mmol) was gradually dissolved into 2.8g KOH (50 mmol) aqueous solution (100 mL), and the solution was cooled in an ice water bath. 2.48 g of (1) (10 mmol) was dissolved in 15 mL ethyl acetate and added dropwise into the above prepared aqueous solution under vigorous stirring. After 30 min, the reaction was stopped and the mixture was neutralized by diluted HCl (5 vol%) aqueous solution to pH=7. The

resulting precipitate was then filtered off by vacuum filtration, and washed with ethanol to obtain 4.28 g product (2)(9.5 mmol, 95% yield) as a white solid. ¹H-NMR (360MHz, DMSO-d₆): δ (ppm)= 7.41 (m, 4H, ArH of d), 8.02 (m, 4H, ArH of e), 8.36 (d, 1H, ArH of c), 8.65 (d, 1H, ArH of b), 8.79 (s, 1H, ArH of a).

2-Nitro, 1,4-benzenedicarboxylic acid, 1,4-bis[4-(chlorocarbonyl)phenyl] ester(3). 4.06 g of (2) (9 mmol) was mixed with 15 mL thionyl chloride under stirring. Two drops of DMF were added as catalyst. The mixture was heated to 75 °C and refluxed until no bubbles were generated from the solution. The reaction mixture was then cooled down to room temperature, and the excess thionyl chloride was removed *in vacuo*. The crude product (3) was obtained as a white solid and used in the next step without further purification.

2-Nitro, 1,4-benzenedicarboxylic acid, 1,4-bis[4-[(2-oxiranylmethoxy)carbonyl]phenyl] ester(4, LCM_X1). 1.3 g (±)-glycidol (17.6 mmol) and 3.90 g of (3) (8 mmol) were dissolved in 30 mL DCM, and the solution was cooled in an ice water bath at 0 °C. 2.15 g DMAP (17.6 mmol) in 20 mL DCM was added dropwise into the above prepared solution under stirring. The reaction mixture was then gradually warmed up to room temperature, and kept for another 6 h. The completion of the reaction was monitored with thin layer chromatography (TLC) until the reactant (3) was completely consumed. The mixture was then filtered through a celite pad, and the solvent was removed *in vacuo*. The resulting oil was purified by column chromatography (silica gel; eluent: DCM, followed by ethyl acetate: DCM=1:15 v/v. R_f ≈ 0.4) to obtain 3.06 g (4) (68% yield) as a white solid. ¹H-NMR (360MHz, CDCl₃): δ (ppm)= 2.75 (dd, 2H, -(O)COCH₂CHCH₂O), 2.93 (dd, 2H, -(O)COCH₂CHCH₂O), 3.36 (m, 2H, -(O)COCH₂CHCH₂O), 4.20 (dd, 2H, -

(O)COCH₂CHCH₂O), 4.71 (dd, 2H, -(O)COCH₂CHCH₂O), 7.38 (m, 4H, ArH of d), 8.04 (d, 1H, ArH of c), 8.20 (m, 4H, ArH of e), 8.59 (d, 1H, ArH of b), 8.88 (s, 1H, ArH of a). *2-Nitro, 1,4-benzenedicarboxylic acid, 1,4-bis[4-[(2-propen-1-yloxy)carbonyl]phenyl] ester*(5, LCM_X2). 1.02 g allyl alcohol (17.6 mmol) and 3.90 g of (3) (8 mmol) were dissolved in 30 mL DCM, and the solution was cooled in an ice water bath at 0 °C. 2.15 g DMAP (17.6 mmol) in 20 mL DCM was added dropwise into the above prepared solution under stirring. The reaction mixture was then gradually warmed up to room temperature, and kept for another 6 h. The completion of the reaction was monitored with thin layer chromatography (TLC) until the reactant (3) was completely consumed. The mixture was then filtered through a celite pad, and the solvent was removed *in vacuo*. The resulting oil was purified by column chromatography (silica gel; eluent: DCM, followed by ethyl acetate: DCM=1:30 v/v) to obtain 2.83 g (5) (66.5% yield) as a white solid. ¹H-NMR (360MHz, CDCl₃): δ (ppm)= 4.87 (dd, 4H, -(O)COCH₂CHCH₂), 5.32 (d, 2H, -(O)COCH₂CHCH₂), 5.44 (d, 2H, -(O)COCH₂CHCH₂), 6.06 (m, 2H, -(O)COCH₂CHCH₂), 7.37 (m, 4H, ArH of d'), 8.04 (d, 1H, ArH of c'), 8.20 (m, 4H, ArH of e'), 8.60 (d, 1H, ArH of b'), 8.88 (s, 1H, ArH of a').

4-(4-(((Oxiran-2-yl)methoxy)carbonyl)phenyl) 1-(4-((allyloxy)carbonyl)phenyl) 2-nitrobenzene -1,4-dioate (6, LCM_X3) 6.8g (12.8mmol) was dissolved in 30 mL DCM at 0 °C. 3.31g MCPBA (20mmol) was gradually added to the solution. The reaction mixture was then warmed up to room temperature and allowed to stir for additional 48 h. After reaction, the white precipitate was filtered off and the resulting solution was washed twice with sodium thiosulfate pentahydrate aqueous solution, followed by wash twice

with brine. The solution was then dried with MgSO_4 and the solvent was removed *in vacuo*. The crude solid was purified by column chromatography (silica gel; eluent, DCM, followed by ethyl acetate: DCM=1:30 v/v) to obtain 2.1g (6) (30% yield). $^1\text{H-NMR}$ (360MHz, CDCl_3): δ (ppm)= 2.75 (dd, 1H, $-(\text{O})\text{COCH}_2\text{CHCH}_2\text{O}$), 2.93 (dd, 1H, $-(\text{O})\text{COCH}_2\text{CHCH}_2\text{O}$), 3.36 (m, 1H, $-(\text{O})\text{COCH}_2\text{CHCH}_2\text{O}$), 4.20 (dd, 1H, $-(\text{O})\text{COCH}_2\text{CHCH}_2\text{O}$), 4.71 (dd, 1H, $-(\text{O})\text{COCH}_2\text{CHCH}_2\text{O}$), 4.87 (dd, 2H, $-(\text{O})\text{COCH}_2\text{CHCH}_2$), 5.32 (d, 1H, $-(\text{O})\text{COCH}_2\text{CHCH}_2$), 5.44 (d, 1H, $-(\text{O})\text{COCH}_2\text{CHCH}_2$), 6.06 (m, 1H, $-(\text{O})\text{COCH}_2\text{CHCH}_2$), 7.38 (m, 4H, ArH of d''), 8.04 (d, 1H, ArH of c''), 8.20 (m, 4H, ArH of e''), 8.59 (d, 1H, ArH of b''), 8.88 (s, 1H, ArH of a'').

3.2.3 Preparation of liquid crystal monomer solutions

200 mg liquid crystal monomer (4, LCM_X1) and 4 mg Iragcure 261 (2wt%, Ciba Specialty Chemicals) as photoacid generator (PAG) were dissolved in 10 g DCM, and kept in a cool and dark place before use.

3.2.4 Fabrication of patterned substrates

All the patterned substrates were fabricated by replica molding from commercially available epoxy (D.E.R. 354, Dow Chemical) on glass slides using PDMS molds, following the procedure reported in the literature²².

3.2.5 Preparation of substrates with desired LC anchoring

(1) Homeotropic anchoring of LCs on flat substrates, porous membranes, and square channels. The anchoring type of the LC (homeotropic or planar) largely depends on the surface energy of the interface.²³ For many types of LCMs, hydrophilic surfaces with high surface energy usually give homeotropic anchoring. In our system, all liquid crystal monomers, LCM_X1, X2, X3, were found to have homeotropic anchoring on SiO_2

surface. Here, we used pre-cleaned glass slides as the flat substrates or coated patterned polymer substrates with a thin layer of SiO₂ through a chemical vapor deposition (CVD) process according to the literature²⁴. In brief, patterned substrates kept in a desiccator under vacuum were first exposed to chemical vapors of silicon tetrachloride (SiCl₄, 0.2 mL) for 10-15 min. Then the samples were exposed to a humidity chamber (humidity ~ 90%) for 10 min, followed by immersion in a pyridine aq. solution (3 vol%) for 5 to 10 min. The final substrates were obtained by washing with ethanol and DI water, respectively, for three times, followed by drying by an air gun and baking at 100 °C in a convection oven for 15 min to 1h.

(2) Strong homeotropic anchoring of LCM_X1 on micropillar arrays. To achieve high homeotropic anchoring energy on micropillar arrays, we first treated pillars based on step (1), followed by functionalization of the SiO₂ surface with APTES. Due to the Michael-addition reactions between the amino groups in APTES and epoxy groups in LCM_X1, the newly formed surface anchored LCM_X1, where the mesogenic groups were orientated perpendicularly to the interface. As a result, the interaction between the interface and LCM molecules was substantially increased, showing stronger homeotropic anchoring than SiO₂ coated surface. In details, the sample consisting of the micropillar array was immersed in a solution of 1 vol% APTES in ethanol/water mixture (90:10 v/v) for ~10 min, followed by rinse with ethanol and DI water three times and dried by air gun. Finally, the sample was baked in a convection oven at 100 °C for 15 min to 1h.

(3) Planar anchoring. To create planar anchoring for LCMs, a glass substrate was spin-coated with a thin layer of polyimide from its xylene solution at 5000 rpm for 30s,

followed by baking at 130 °C for 20 min. A uniform planar anchoring sample was obtained by rubbing the polyimide coated substrate with a velvet cloth.

3.2.6 Liquid crystal cell preparation

(1) On patterned substrates. ~20-40 μL LCM_X1/DCM solution was placed on the patterned substrate, and solvent DCM was evaporated at 130 °C for at least 10 min. Then the LCM_X1 liquid was sandwiched between the substrate and another cover glass (treat if needed) at 130 °C. The sample was then cooled down to the desired temperature (cooling rate not critical here) to align LC.

(2) With silica colloids. 5 μm diameter silica colloids (Sigma Aldrich) were dispersed in a LCM_X1/DCM solution (Note, a high concentration of ~20 wt% was preferred), and the mixture was sonicated for at least 15 min to obtain a homogeneous suspension. To prepare LC cell with silica colloids, several drops (~20-40 μL) of the suspension were placed on a clean glass slide, and solvent was evaporated at 130 °C for at least 10 min. Then another pre-cleaned glass slide was placed on top to make a LC cell. The thickness of the LC cell was roughly controlled as ~10 μm . The sample was then cooled down from 130 °C to the desired temperature (cooling rate not critical here) to align the LC.

3.2.7 UV Crosslinking

To prevent the re-orientation of the directors of LCM_X1 during photopolymerization, UV curing was carefully performed in three steps, including

- (1) Samples were slowly cooling down at 1 °C/min to room temperature (~25°C);
- (2) Sample was exposed to a low UV power (~2 mw/cm^2 at 365 nm, Hg lamp), overnight.

(3) After UV exposure, samples were slowly heated up to 100 °C at a ramping rate of 1°C/min on a Mettler FP82 and FP90 thermo-system hot stage in ambient air, followed by baking at 120 °C for another 1-2 h to completely cure the epoxy groups.

3.2.8 Characterization

Chemical structures of the synthesized chemicals were confirmed with ¹H-NMR performed on a Bruker Advance DMX 360 (360 MHz) spectrometer at 25°C and analyzed with TOPSPIN software. Thermo analysis of the synthesized LCs was performed on a differential scanning calorimetry (DSC) Q2000 (TA instrument). Samples were heated and cooled under nitrogen with a ramping rate of 10°C /min for three cycles. Data from the 2nd cycle was reported. Liquid crystal phases and alignments were observed under an Olympus BX61 motorized optical microscope with crossed polarizers using CellSens software. Liquid crystal polymer samples were manually broken into pieces or cut with a razor blade. The cross-section was coated with a 4 nm iridium layer for Scanning Electron Microscopy (SEM). Imaging was performed on a dual beam FEI Strata DB 235 Focused Ion Beam (FIB)/ SEM instrument with 5KV electron-beam.

3.2.9 Measurement of refractive index and birefringence

We used Snell's law to estimate the refractive indices of LCM_X1 by comparing the apparent thickness of LC cell, D_{LC} , with the actual cell thickness without LC, D_0 , that is, $n_{e,o} = D_0 / D_{LC}$. We prepared a uniform planar cell in the way same as described earlier. D_0 and D_{LC} were measured before and after LC was infiltrated, respectively. Accordingly, we obtained the extraordinary refractive index, $n_e \sim 1.67 \pm 0.02$ and ordinary refractive index, $n_o \sim 1.5 \pm 0.02$ of LC when the polarized light was parallel and perpendicular to the LC director, respectively. The birefringence of LCM_X1 was estimated ~ 0.17 . We also

estimated birefringence of LCM_X1 from a wedge cell using the Michael-Levy chart before and after UV curing as 0.16 ± 0.02 , in good agreement with that measured from optical microscopy. Again, the consistent birefringence before and after polymerization as shown in Figure 3D-E clearly indicates that polymerization did not affect the nematic order parameter.

3.3 Design of stable nematic liquid crystal

Visualization of topological defects has been achieved by dispersing polymer fibers in pre-aligned, low-molecular weight NLC^{25, 26}. However, the polymer fibers, fabricated *in situ via* polymerization of LCMs, often phase-separate from the nematic host; thus maintaining the LC director field in a non-glassy nematic host for direct visualization is thwarted. Moreover the fibers themselves can perturb the nematic phase, inducing artifacts and spurious defects. Of course, to visualize the native director field responding to geometric surface cues we must employ molecules that can be aligned reliably at interfaces of different topology, topography, and surface chemistry. Typically, the alignment of LCMs is controlled *via* mechanical rubbing of a polymer layer, use of a photo-alignment layer²¹, mechanical stretching, or application of magnetic fields²⁷⁻³¹. However, these techniques are limited in their spatial resolution, especially in comparison to the highly refined ability to impart chemical anchoring on boundaries with complex topography and topology at the micro- and nanoscales, and which also require high uniformity across the large sample areas. Though functional LCMs have been employed for decades in conjunction with LCPs as actuators and sensors²⁷⁻³². It remains challenging to achieve faithful anchoring control at the level of the old stalwart, 5CB (4-cyano-4'-

pentylbiphenyl). Meanwhile, slow relaxation of the bulk director field will lead to spurious defects in LCMs (or polydomain configurations) as shown in Figure 3.1 from widely used LCM's in literature; this inherent obstacle becomes increasingly obvious under complex confinement.

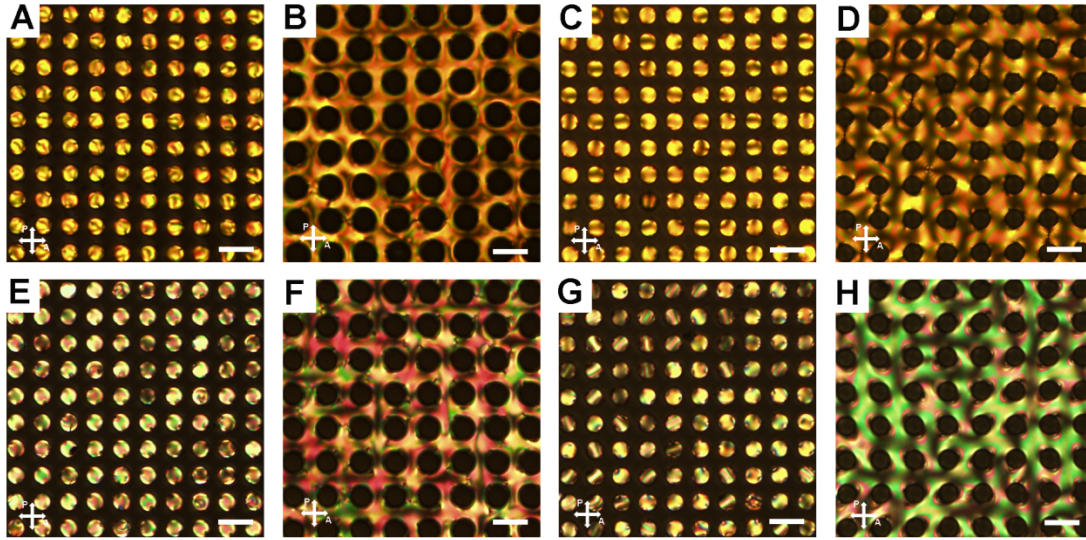


Figure 3.1 POM images of LCM_AZO [4-ethoxy-4'-(6-acryloyloxyhexyloxy) azobenzene] and RM257 on various patterned epoxy substrates coated with different surface chemistry. (A) LCM_AZO in PVA coated square array of pores. (B) LCM_AZO between PVA coated square array of pillars. (C) LCM_AZO in DMOAP coated square array of pores. (D) LCM_AZO between DMOAP coated square array of pillars. (E) RM257 in PVA coated square array of pores. (F) RM257 between PVA coated square array of pillars. (G) RM257 in DMOAP coated square array of pores. (H) RM257 between DMOAP coated square array of pillars. Pores in A, C, E, and G: diameter: 10 μm , pitch: 15 μm , depth: 20 μm . Pillar arrays in B, D, F, and H: diameter: 10 μm , pitch: 20 μm , height: 19 μm . Samples were cooled slowly (1 $^{\circ}\text{C}/\text{min}$) from isotropic phase (100 $^{\circ}\text{C}$ for LCM_AZO and 130 $^{\circ}\text{C}$ for RM257) to nematic phase (94 $^{\circ}\text{C}$ for LCM_AZO and 125 $^{\circ}\text{C}$ for RM257). Scale bar applied to all figures: 20 μm .

Since the surface energy of the boundary determines the anchoring behavior of liquid crystal molecules (homeotropic or planar)²³, we prepared patterned surfaces with both high (PVA) and low (DMOAP) surface energy. However, as seen from Figure 3.1, it is clear that both LCM_AZO and RM257 fail to align uniformly on patterned surfaces

regardless of the surface energy of the coatings and surface geometry. They mostly show polydomains with disclination lines either in the bulk or pinned to the boundaries. Although this non-equilibrium alignment can be improved by carefully annealing the sample through the nematic-isotropic phase transition, it is non-trivial to achieve the ideal equilibrium state with monodomains.

To address this, we specially designed and synthesized a series of LCMs (LCM_X1, X2, X3, see Figure 3.2&3.3) with both strong surface anchoring and highly stable nematic phases. These LCMs suppress spurious defects, leaving only those required energetically and topologically. The monomers all have the same aromatic ester-based mesogenic group, both common and inexpensive to synthesize, with an *ortho*-substituted nitro group but different terminal groups, epoxy and alkene, both of which are readily photocrosslinkable at ambient conditions *via* photoacids and “click” chemistry, respectively. We confirmed the chemical structures *via* ¹HNMR (Figure 3.4). Similar LCMs terminated with epoxy or alkene groups have been reported with nematic phases in the literature³³ although they typically have very high phase transition temperatures, making it difficult to maintain the director field during polymerization due to the relatively low viscosity of the LCMs in the nematic phase. In addition, their anchoring properties have not been well characterized.

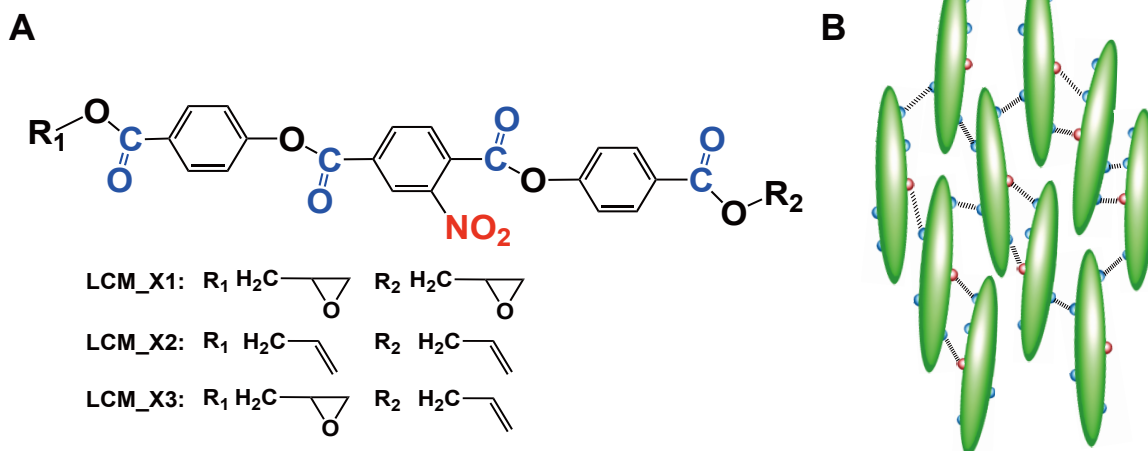


Figure 3.2 Schematic illustrations of (A) the chemical structures of various liquid crystal monomers, LCM_X1, LCM_X2 and LCM_X3 and (B) random intermolecular dipole-dipole interactions between nitro and carbonyl groups. Different colors represent different functional groups: red for nitro; blue for carbonyl.

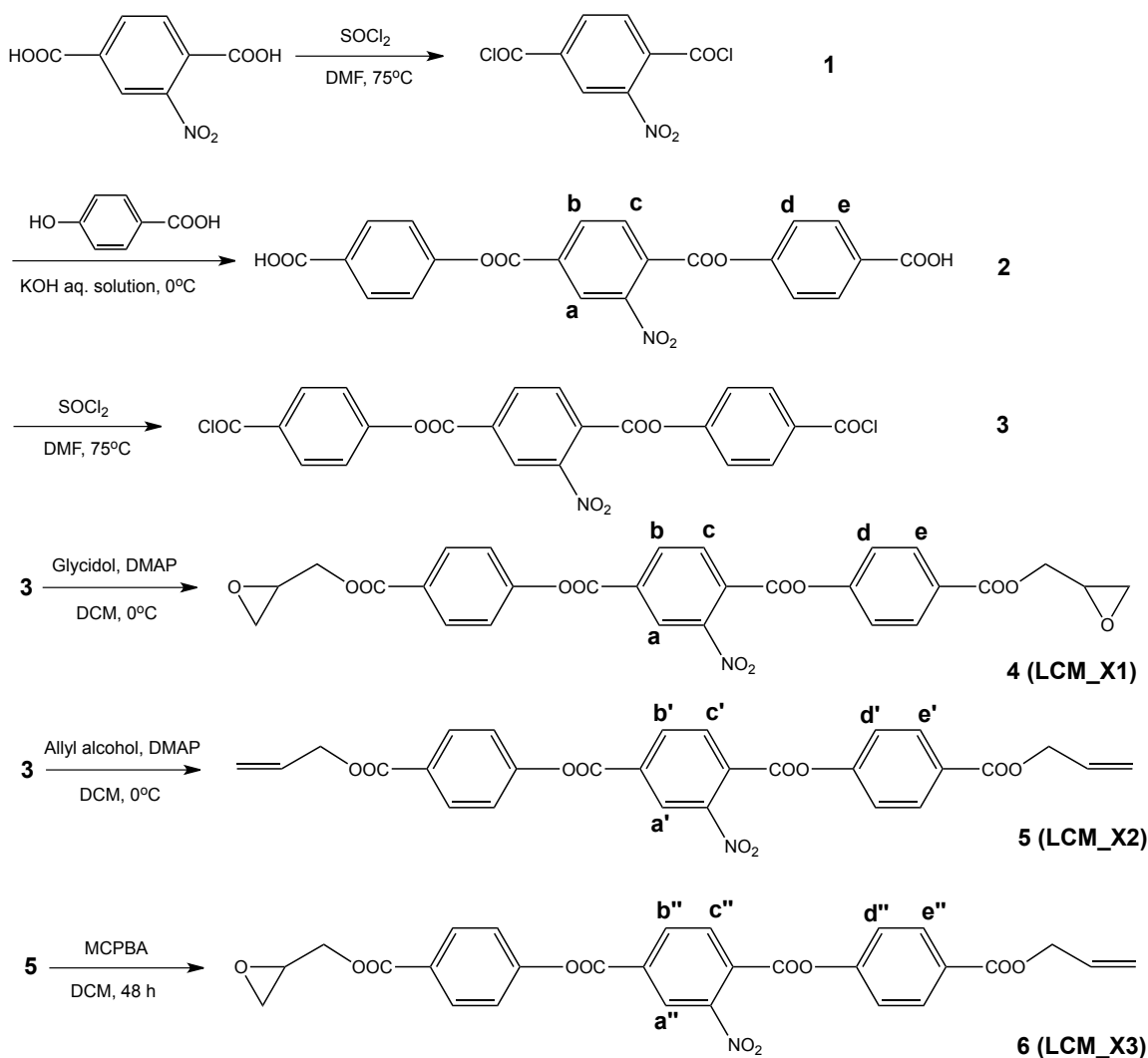


Figure 3.3 Schematic illustrations of the synthesis of the nematic liquid crystal monomers.

We introduced a pendant nitro group on the aromatic ring because it has been suggested that i) LCs with a nitro group at the *ortho*-position to a linkage ester group typically form a nematic phase with a relatively low phase transition temperature³⁴ and, more importantly, ii) the introduction of a polar (e.g., nitro) or polarizable group into the chemical structure often results in an increase of molecular polarity, affecting molecular packing and, in turn, the phase stability of LCs³⁴. In particular, aromatic ester-based

mesogens could achieve a stable nematic phase through strong intermolecular dipole-dipole interactions between carbonyl groups of adjacent molecules, an effect that increases with the strength of the molecular interaction^{35, 36}. In our system, we expect strong dipole-dipole interactions between carbonyl groups (dipole moment $\mu=2.4\text{D}$)³⁷ that are evenly distributed along the molecule and a more polar nitro group ($\mu=4.01\text{D}$)³⁷ in the middle of the molecule. Because each nitro group bonds randomly to one of the four sites from the adjacent LC molecule, crystallization is suppressed, as seen in analogous systems^{33, 36, 38}, leading to a highly stable nematic phase (see Figure 3.5) with strong surface anchoring properties for all LCMs we synthesized (see Figure 3.6&3.7). Here, we focused our study on LCM_X1 because it has both a large nematic window ($> 100\text{K}$) with the nematic phase starting slightly above its glassy transition temperature ($\sim 10\text{ }^\circ\text{C}$) and the terminal epoxy groups could be rapidly and locally crosslinked by photoacids without large volume change – effectively locking the orientational order of mesogens for later SEM imaging.

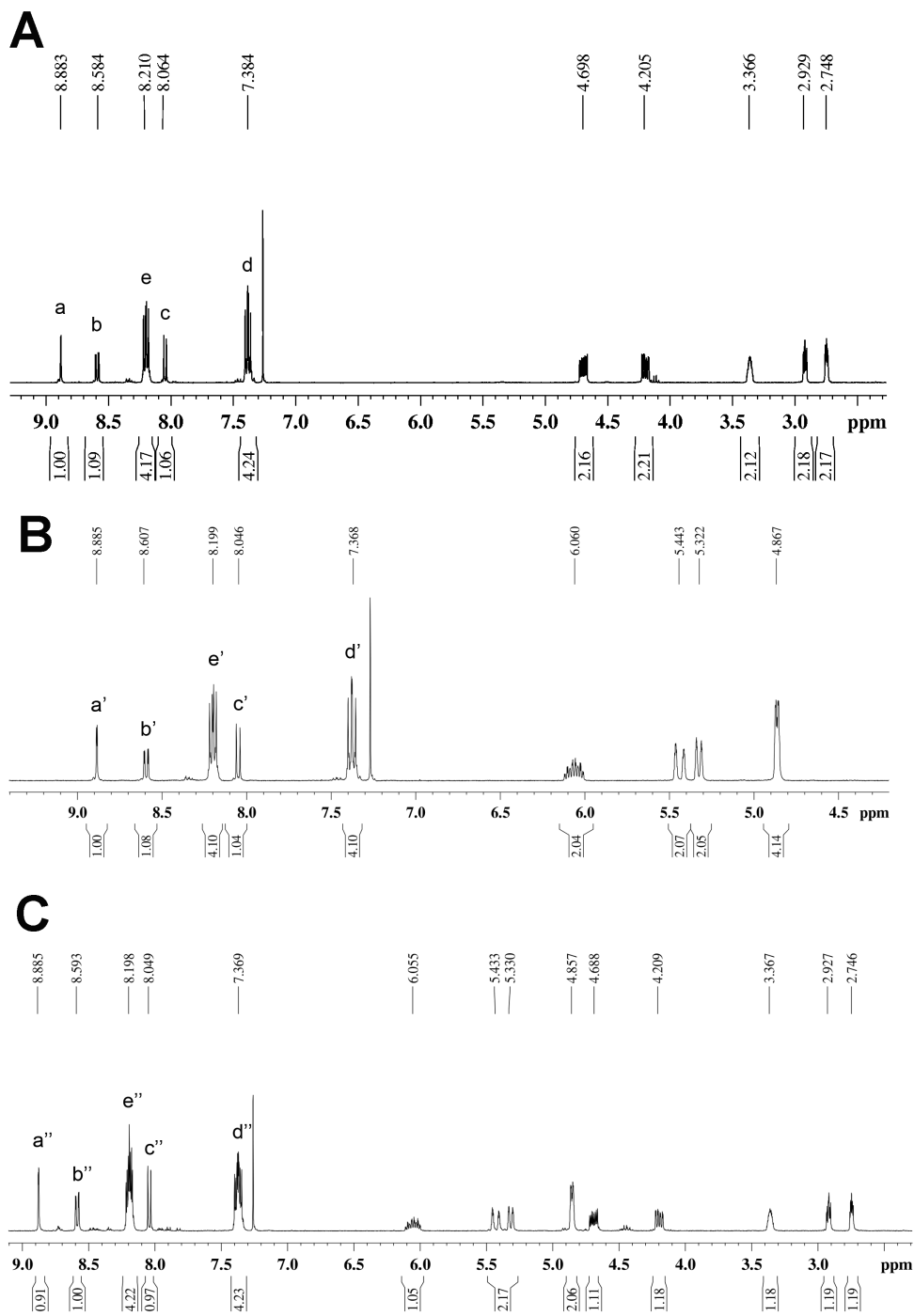


Figure 3.4 $^1\text{H-NMR}$ spectrum of the liquid crystal monomers (A) LCM_X1; (B) LCM_X2; (C) LCM_X3.

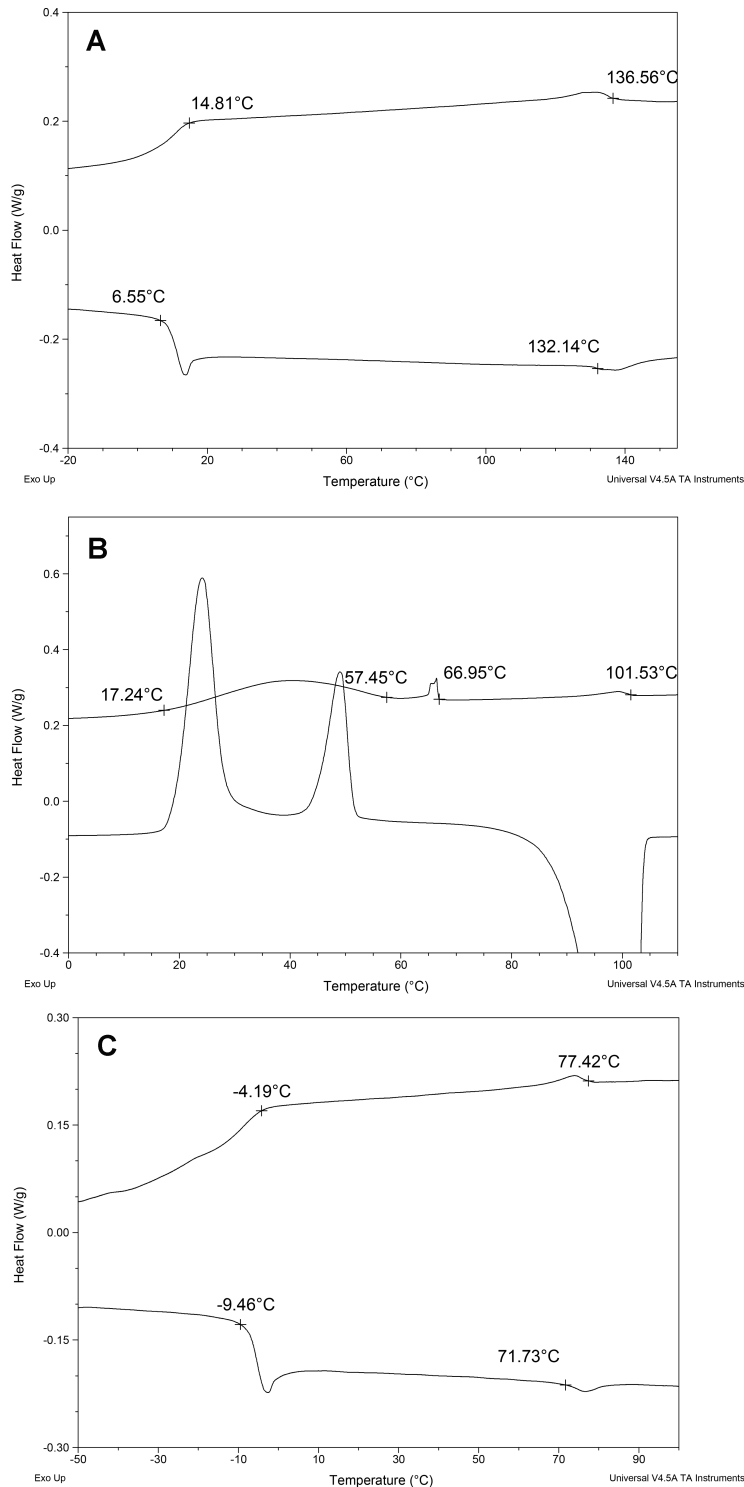


Figure 3.5 DSC curves of the LCMs. (A) LCM_X1. A nematic phase from 6.5 °C to 132 °C (heating) and 136 °C to 15 °C (cooling), respectively, was observed. (B) LCM_X2. A nematic phase was only observed upon cooling from 101 °C to 57 °C*. (C) LCM_X3. A nematic phase was shown from -9 °C to 72 °C (heating) and 77 °C to -4 °C (cooling), respectively.

3.4 Liquid crystal anchoring study

We employed patterned substrates that were well-characterized in our labs, including membranes with cylindrical pores, micropillar arrays, and square-shaped one-dimensional (1-D) microchannels with strong homeotropic anchoring (see details in Materials and Methods) to study the alignment of newly synthesized LCMs in comparison with small molecule NLC, 5CB. As seen from the polarized optical microscopy (POM) and bright field (BF) images shown in Figure 3.6A-C, both molecules are readily aligned with nearly identical director configurations on all patterned substrates despite the difference in surface treatments to align LCM_X1 vs. 5CB. Similar anchoring configurations are also observed for LCM_X2 and X3 (see Figure 3.7). For LCM_X1, homeotropic anchoring was achieved on silica coated surfaces while planar anchoring was achieved on polyimide treated surfaces. This is in sharp contrast to the behavior of commonly used LCMs, RM257 and LCM_AZO, which exhibit polydomains on the same substrates regardless of surface treatment (see Figure 3.1).

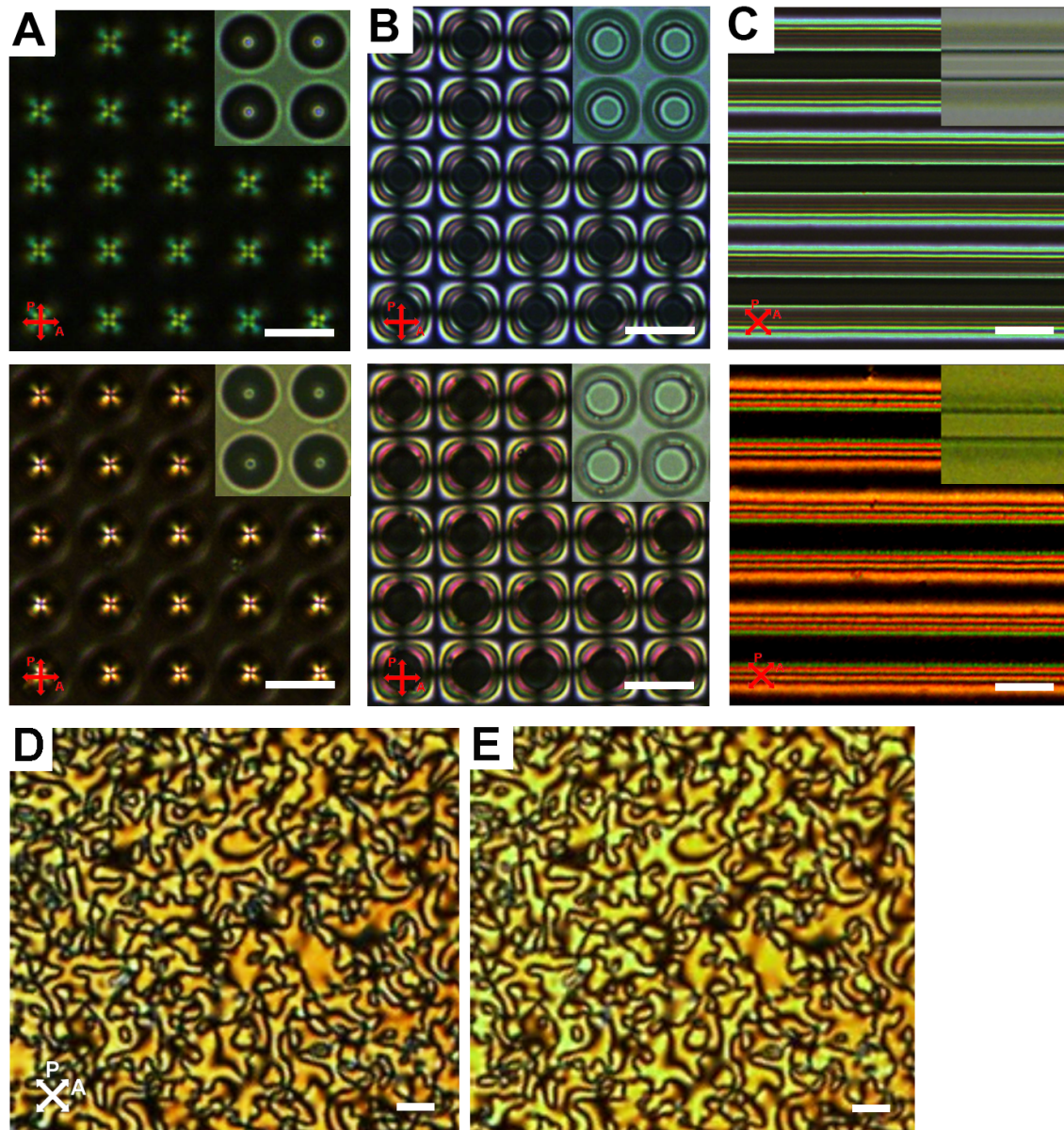


Figure 3.6 POM and BF images of 5CB and LCM_X1. (A-C): POM and BF images of 5CB (top panels) and LCM_X1 (bottom panels) in (A) porous membranes (diameter: 10 μm , pitch: 15 μm , depth: 20 μm), (B) pillar arrays (diameter: 10 μm , pitch: 20 μm , height: 19 μm), and (C) square channels (width: 10 μm , pitch: 40 μm , depth: 20 μm) with homeotropic anchoring imposed at all surfaces. Insets in A: BF image of LCs in pores where the dark dots at the center showing possible defects; Insets in B: BF image with black circles showing possible bulk line defects circumscribing the pillars; Insets in C: BF image of a single ridge where the gray color indicates a distorted director field but no defect; (D-E) POM images of the schlieren texture of LCM_X1 before (D) and after (E) UV curing. The nearly identical nematic schlieren textures indicate that the LC director field is well-maintained during polymerization. Scale bars, 20 μm applicable to all panels.

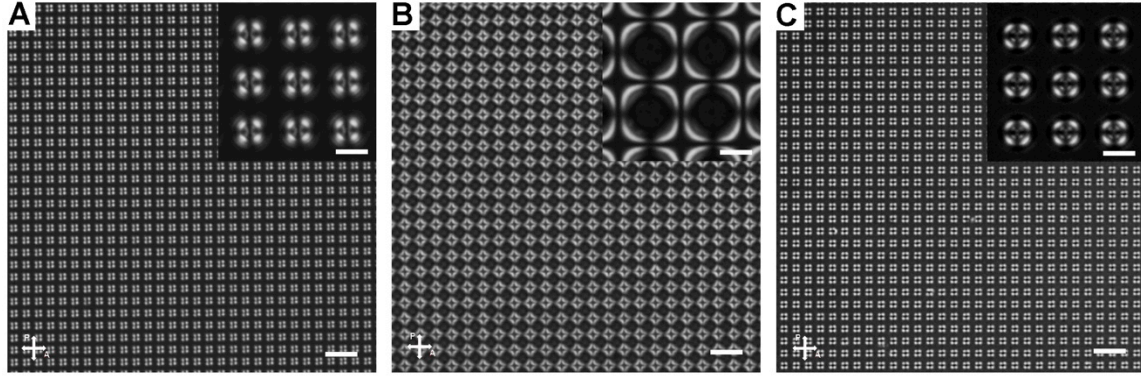


Figure 3.7 POM images of various LCMs on patterned substrates with homeotropic anchoring at the boundaries. (A) LCM_X2 in the square array of pores. (B) LCM_X2 between the square array of pillars. (C) LCM_X3 in the square array of pores. Scale bars: 40 μ m. Insets: POM images with higher magnification. Scale bars: 10 μ m. Pores in A&C: diameter: 10 μ m, pitch: 15 μ m, depth: 20 μ m. Pillar arrays in (B): diameter: 10 μ m, pitch: 20 μ m, height: 19 μ m. Samples were fast cooled (\sim 20 $^{\circ}$ C/min) from isotropic phase (LCM_X2, 110 $^{\circ}$ C; LCM_X3, 85 $^{\circ}$ C) to nematic phase (LCM_X2, 90 $^{\circ}$ C; LCM_X3, 70 $^{\circ}$ C).

In cylindrical pores with homeotropic anchoring on all boundaries, the nematic director either forms a bulk point defect with integer topological charge (± 1) in the center or it "escapes into the third dimension"^{39, 40} to separate two half-defects on the boundaries. Likewise, in the pillar arrays, there could be a bulk disclination ring surrounding the pillars¹⁵ or an escape configuration where the defects are all concentrated next to the pillar edges. However, neither POM nor BF microscopy can distinguish these two modalities without further investigation of the director field through the whole sample, or through the use of a variety of state-of-the-art tools such as confocal polarized microscopy.

3.5 Direct mapping of liquid crystal local direct field

To access the director information in these geometries, we crosslinked the LCMs through cationic polymerization of epoxy, a common reaction in negative-tone photoresists^{41, 42}. Compared to acrylate and methacrylate groups that are often used in radical polymerization of LCMs, epoxides have several advantages that are key to our LCM design: 1) They are insensitive to ambient oxygen. 2) They can be crosslinked efficiently through chemically amplified ring-opening reactions; each photogenerated acid can initiate hundreds of reactions locally, rendering fast polymerization without large volume shrinkage seen in (meth)acrylate polymers. 3) The bulky aromatic ester mesogens limit acid diffusion at room temperature, therefore, photopolymerization occurs locally. Together with the strong dipole-dipole intermolecular interactions, our LC molecules can lock in position effectively without altering the field direction during polymerization. Closely related are earlier studies of cationic photopolymerization of LC diepoxides^{43, 44}, which show that the NLC phase is maintained in the densely crosslinked network -- in contrast to that from radical polymerization of diacrylates. It was noted, however, that unintentional heating by the high intensity UV light could realign the mesogens, thus, increasing the order parameter after curing⁴⁴. In order to prepare even cleaner data, we further suppressed reorientation during crosslinking by performing the UV curing at room temperature (~ 25 °C) with a low UV light intensity (2 mw/cm^2), keeping the viscous timescales longer than the polymerization timescale (see detailed in Experimental methods).

From the birefringence of the material (see Experimental methods) and the POM images of samples before and after polymerization (Figure 3.6D, E), we confirmed that

on the micron scale the director field was preserved during polymerization. However, it should be noted here that the LCM-X1 sample appeared somewhat yellowish after polymerization. The slight change in color can be attributed to the difference in UV-vis absorption of monomer vs. polymer (Figure 3.8).

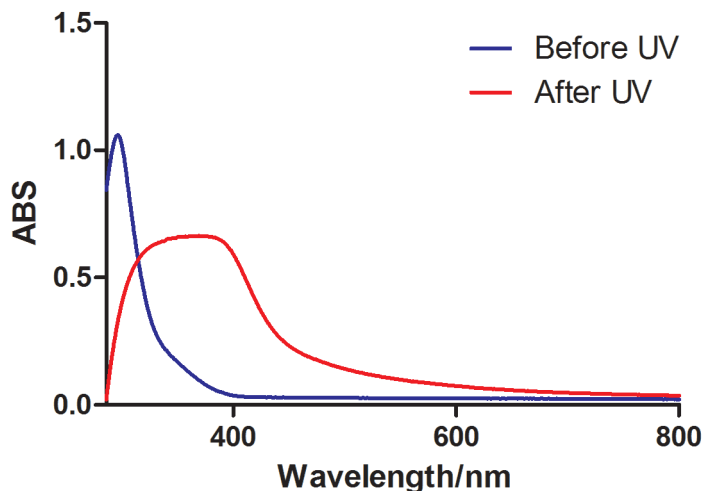


Figure 3.8 UV-Vis spectra of LCM_X1 before and after UV curing.

Once polymerized, we could use SEM to directly visualize the nematic texture with nanoscale resolution of the director configuration in various cross-sections obtained by fracturing the sample at room temperature. As shown in Figure 3.9A-C, the local director field is visible under SEM, represented by the nanofiber-like fracture structures, the footprints of the director field. We should note that the polymer itself does not form fibers. Rather, the oriented structures observed in SEM are a consequence of the anisotropic mechanical properties of LCPs, in which the bulk elastic modulus is usually much smaller perpendicular to the director^{21, 45}, and in which fractures occur along surfaces parallel to the director field^{46, 47}. The same type of fracture pattern can be observed in a nematic polymer which has some similarity with our LCPs⁴⁵. Following the

fracture structures, we directly mapped the LC alignment with 100 nm resolution as illustrated by the red dotted line in Figure 3.9. From Figure 3.9A and we determine the angle of molecular alignment at the surface to be 90° inside a wide channel; likewise, we can see that homeotropic anchoring breaks down when the director field is tightly confined as shown in Figure 3.9B-C. We can now directly visualize the defect structure in pores, pillar arrays, and 1-D channels, and observe that the director most often adopts an escaped configuration, avoiding defects in the bulk. By contrast, in POM the observed point- and line-like structures could just as well be the sign of a distorted director field or a defect. Further, from SEM images we can estimate the elastic constants and the extrapolation length of the LCM⁴⁸ for planar and homeotropic anchoring (see Section 3.6).

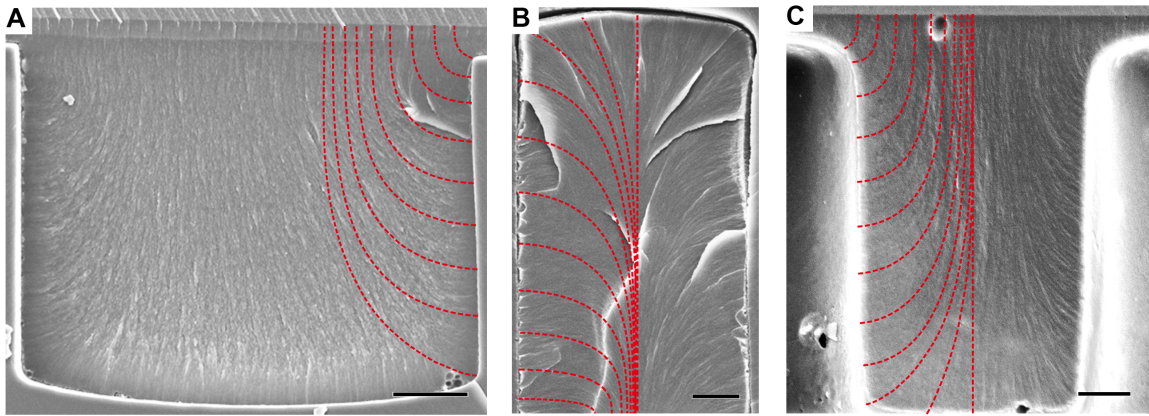


Figure 3.9 SEM images show the fracture structure of LCP after polymerization in a 1-D microchannel (A), in a pore (B), and between two pillars (C). Escaping director field of LC can be observed from the orientation of the fracture structures in all three structures; The red dotted lines in A-C represent local director field of LCM mirrored in the other half of images. Scale bars: A: 5 μm ; B and C: 2 μm .

3.6 Estimation of the elastic constants of liquid crystal monomers

The elastic anisotropy of LCM_X1 was estimated by looking at the SEM images (see Figure 3.10) of the LCM homeotropically anchored on the walls of a cylindrical pore. The director here “escapes in the third dimension” through a splay/bend deformation. We look at the angle ϑ that the nematic director adopts at any point relative to the axis of the pore (see Figure 3.10 inset), as a function of the radius r , which goes from the center of the pore to its walls. The results are plotted in Figure 3.10. We find that the data points can be very satisfactorily fit by eq. (3-1).⁴⁰

$$\vartheta(r) = 2 \tan^{-1}(\alpha r/R_0) \quad (3-1)$$

where R_0 is the width over which the escape takes place (the radius of the pore), and α is a parameter that depends on the anchoring angle of the director on the homeotropic wall. Specifically, α is equal to the cotangent of the anchoring angle φ_h at the homeotropic wall of the capillary divided by two. Eq. (3-1) is the theoretical prediction for the escape configuration in a cylindrical channel in the approximation of single elastic constant. It holds when the splay constant and the bend constant are equal. Figure 3.10 shows a good agreement between the experimental data and the theoretical prediction, which suggests that the ratio between splay and bend constant for our monomers is close to one. As shown in the literature⁴⁹, elastic anisotropy would lead to deviations from this curve.

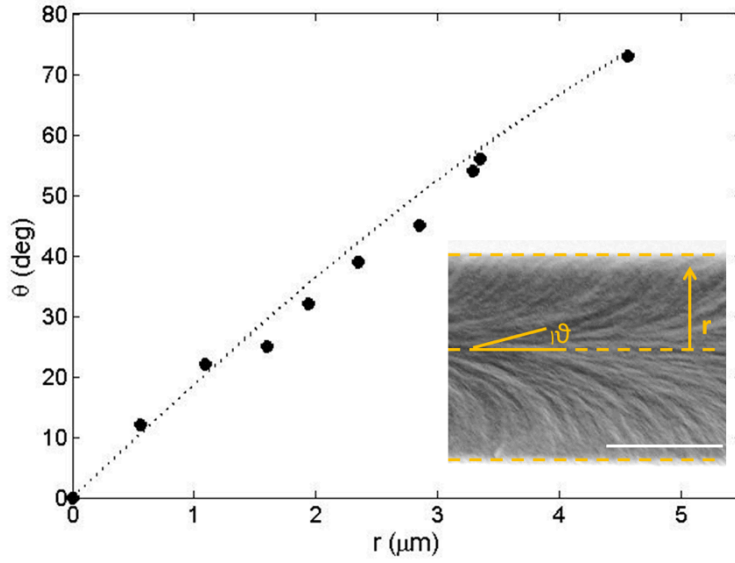


Figure 3.10 Director angle as a function of the radial coordinate r . The points are calculated from the escape configuration shown in the inset (scale bar, $5 \mu\text{m}$). The line is calculated from Eq. (3-1).

We do not get information about the twist elastic constant in this configuration, but the lack of twisted escape configuration (observed, for example, in phases with very low twist elastic constant), combined with the observed structure of the hedgehogs near colloids, suggests that the twist elastic constant is of the same order of magnitude as the other two.

From Eq. (3-1) and the model proposed by Crawford *et al.*⁴⁰, we can also estimate the extrapolation length for homeotropic anchoring, *i.e.* the ratio between the elastic and the anchoring constant. The anchoring angle φ_h on the homeotropic wall is expressed in eq. (3-2).

$$\varphi_h = \sin^{-1}(((R_0 W_h + K_{24})/K - 1)^{-1}) \quad (3-2)$$

where W_h is the homeotropic anchoring constant, K is the elastic constant (always in the one elastic constant approximation), and K_{24} is the saddle-splay constant. If we make the common approximation of neglecting K_{24} , we obtain the extrapolation length $\xi_h = K/W_h = 1.3\mu$.

In order to estimate the extrapolation length in the case of weak planar anchoring, we use a hybrid wedge cell, with one glass untreated (for homeotropic anchoring) and the other one treated with rubbed polyimide. Following the method in the literature⁵⁰, we can estimate the extrapolation length by directly measuring the angles formed by the liquid crystals in a hybrid wedge cell with the homeotropic and the planar surfaces, and relating them as eq. (3-3) and (3-4):

$$2 \xi_h (\varphi_p - \varphi_h) = d \sin(2(\Phi_h - \varphi_h)) \quad (3-3)$$

$$2 \xi_p (\varphi_p - \varphi_h) = d \sin(2(\Phi_p - \varphi_p)) \quad (3-4)$$

Here, the subscript p and h represent the planar and the homeotropic surfaces, respectively, d is the cell thickness, ξ the extrapolation length, Φ the preferred angle with respect to the normal and the flat surface (that is, Φ_h is zero and Φ_p is $\pi/2$), φ is the angle that the nematic director forms with the normal to the cell surface (see Figure 3.11). In writing this formula from reference⁵⁰, we already make the approximation that the ratio of the splay and bend elastic constant is close to unity. The extrapolation length can then be estimated at various thicknesses of the wedge cell. We could estimate ξ_h from the study of LCM in the pores with homeotropic anchoring, and that with planar anchoring, ξ_p .

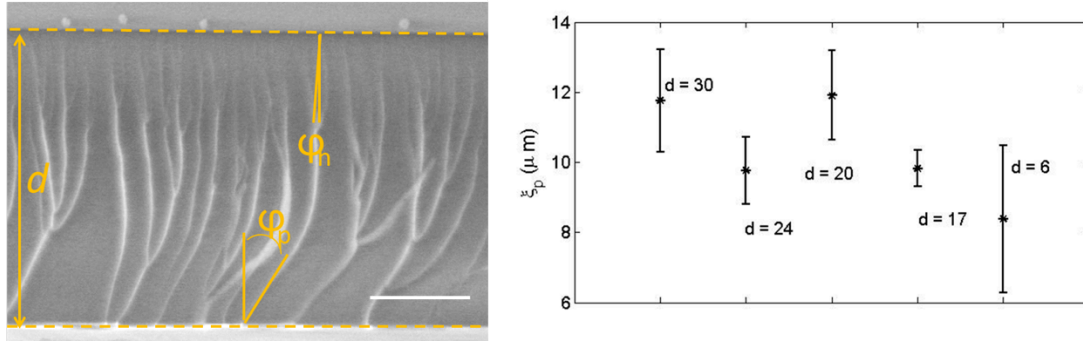


Figure 3.11 SEM image of a hybrid wedge cell (left panel), with highlighted angles at the planar and homeotropic surface, and the corresponding measurements of the planar anchoring extrapolation length (right panel) taken from the cell at different cell thicknesses (indicated next to each data point, in microns). Scale bar in SEM image, 10 μm .

The preferred tilt angle on the planar polyimide surface could be independently estimated by measuring it directly from the SEM images on a planar cell. The points in the SEM image shown in Figure 3.11 represent measurements of the extrapolation length at different thickness of the wedge cell, ranging from 6 μ to 30 μm , which gives a value of the planar extrapolation length $\sim 10 \mu\text{m}$, *i.e.* ten times longer than the homeotropic extrapolation length. This clearly shows that the anchoring is weaker on the polyimide than on the silica surface.

We should remark that the direct visualization of the director profile by SEM image makes it extremely simple and direct to calculate the relevant parameters for our newly synthesized LC. A crude estimate of the elastic constants can be obtained simply by dividing the energy necessary to align the mesogens (*i.e.* the thermal energy at the temperature at which the mesogen achieves its alignment, around 370K) by the molecular size a . $K = k_B T / a = 1.4 * 10^{-23} * 370 \text{ K} * 0.5 * 10^9 \text{ m}^{-1} = 2.6 * 10^{-12} \text{ N}$, which is on the order of a few pico-Newtons, in line with the elastic moduli of other LCs. Consequently, the

homeotropic anchoring constants can be calculated as the ratio between the elastic constant and the extrapolation length: $W_h = 2.6 \times 10^{-12} \text{ N} / 1.3 \text{ } \mu\text{m} = 2 \times 10^{-5} \text{ N/m}$ and $W_p = 2.6 \times 10^{-6} \text{ N/m}$, indicating relatively weak anchoring for both homeotropic and planar anchoring.

3.7 Direct mapping of liquid crystal defect structures

Armed with our careful study of the local director field of LCs on patterned surfaces, we turned to more complex director field structures: point defects and line defects created by colloids with homeotropic anchoring suspended in NLC. POM images in Figure 3.12 depict typical pictures of hedgehog and Saturn ring defects surrounding silica colloids. Though numerous studies have focused on these defects in LC systems with varying colloidal size, geometry, and topology⁵¹⁻⁵⁴, direct visualization of the director structure is difficult, as is measuring the precise position of the induced topological defects. With fracture and SEM, here, we can determine these features with 100 nm accuracy. Consider, for example, the hedgehog in Figure 3.12A; the defect can be seen as clearly located 2 μm above the colloid. In the same sample, we also found Saturn ring line defects around other silica colloids – Figure 3.12B shows a typical defect with a slightly tilted director field. This slight tilting (tilting angle $< 15^\circ$) could not be detected by POM (Figure 3.12B inset); however, it can be easily read off from SEM.

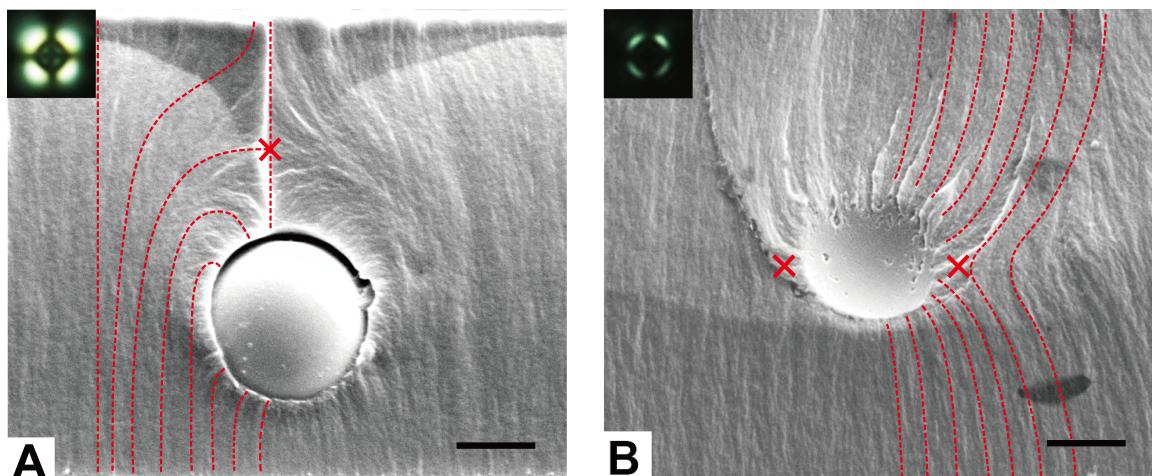


Figure 3.12 SEM images of silica colloids suspended in LCP where either a point defect (A) or a line defect (B) was formed to screen the charge of the colloid. Insets: POM images of point (A) and line (B) defects circumscribing silica colloids. The director field of the LC is represented by the red dotted line and the red crosses show the position of defects. Scale bars: 2 μm

We can use this technique to study the nematic textures in more complex LC systems. For instance, in Figure 3.13 we show a LC cell treated for homeotropic alignment that we expect to image as black in POM. Instead, we see the appearance of blue regions, suggesting planar alignment, separated from the dark regions by disclination lines. Though such disclination lines are metastable in a neat NLC and relax very quickly, they can have a much longer lifetime when they are stabilized by colloids trapped at the disclinations. To observe the structures in Figure 3.13B-E with SEM, we again cooled down the sample and then crosslinked the LCM_X1. In Figure 3.13B a disclination line generated at the boundary of the homeotropic and planar regions is shown. The disclination line can be identified by the fracture structure below and above the fracture plane in SEM as shown in Figure 3.13B because of the different mechanical properties of the defect. Similar line defects can also be found in Figure 3.13C, where

silica colloids are trapped at the boundary. From the SEM images, we can observe the merging of the line defect in the bulk of LC and the Saturn ring surrounding the colloid. Further, it should be noted that bulk disclinations can also be stabilized by pinning to boundaries of the LC cell, as illustrated in Figure 3.13D. The bending of the director field can be observed with such clarity that in future work we plan to use this data to study the bending energy of LCs along the defect line as we move from the bulk towards the boundary. Figure 3.13E shows the LC orientation inside a planar-like region stabilized by silica colloids. The escaped configuration is surprising since it requires a large bending of the director field from the homeotropic boundaries to the center of the LC cell, resulting in a high elastic energy in the bulk of this 2D LC thin film ($\sim 8 \mu\text{m}$). A clarifying example of this behavior can be found in the SI Appendix, where we show a SEM image of a small escape region whose boundaries could be both visualized in the same picture (Figure 3.14). The SEM images provide us a detailed director configuration in this small region, where the planar region starts at the surface of a colloid with an associated defect with charge -1, escapes in the direction determined by the defect structure around the colloid and finally ends at another colloid surface. These SEM studies thus provide us the capability to fully explore LC anchoring behaviors inside LC cells featuring complex topology and also to “lock” and observe metastable states.

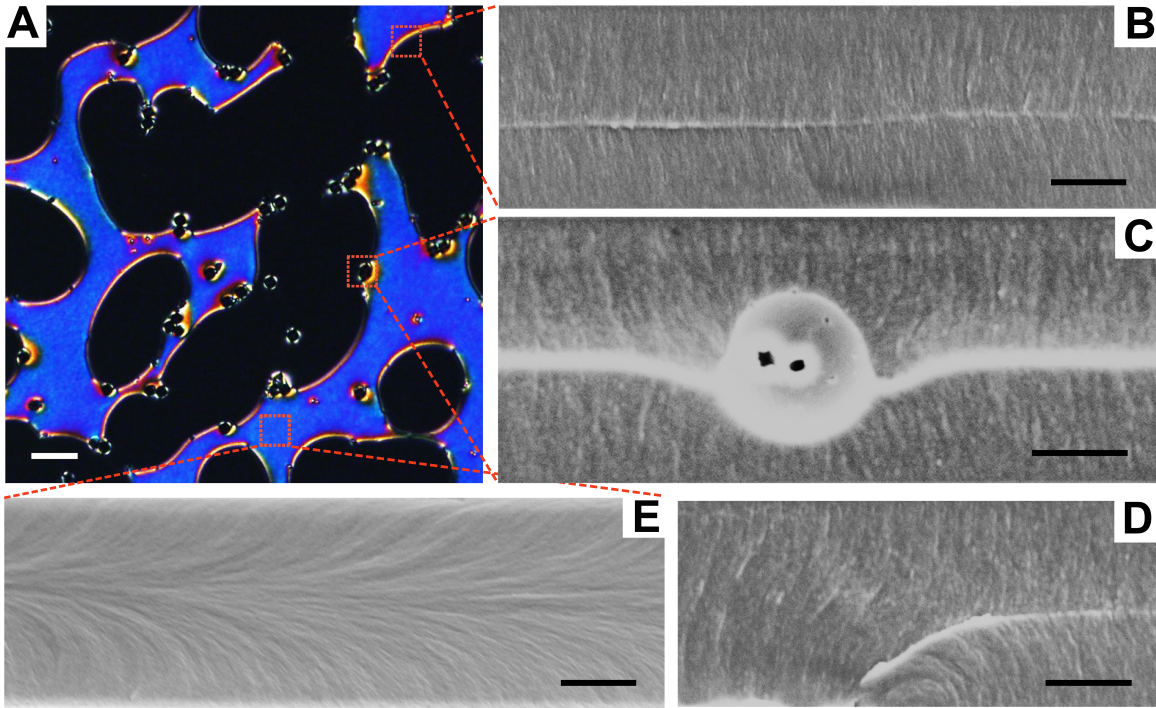


Figure 3.13 Metastable configurations. (A) POM image of silica colloids suspended in LCM resulting in coexistence of homeotropic and planar-like regions, where the metastable planar regions (blue color) are stabilized by silica colloids. (B, C, E) SEM images characterizing the local director field at different positions in (A) as indicated by the red dotted squares. (B) SEM image taken at the boundary between homeotropic and planar regions of LC, where a bright line in the middle of the image is shown, indicating the presence of a disclination line defect. (C) SEM image of a silica colloid sitting at the boundary. The bright line in the image shows a line defect in the bulk of LC that merged with the Saturn ring defect encircling the colloid. The silica colloid was trapped in the middle of the LC cell, and slightly sank downwards. (D) SEM image of fiber-like structure that shows a bulk disclination line pinned to the bottom surface, as indicated by the bending white line. (E) SEM image of local LC director field inside an escaped region. Horizontally aligned fiber-like fractures indicating planar alignment of LC director field were found in the middle of the image, where the bending fiber-like fractures from top and bottom boundaries merged. Scale bars: A: 20 μm ; B-E: 3 μm .

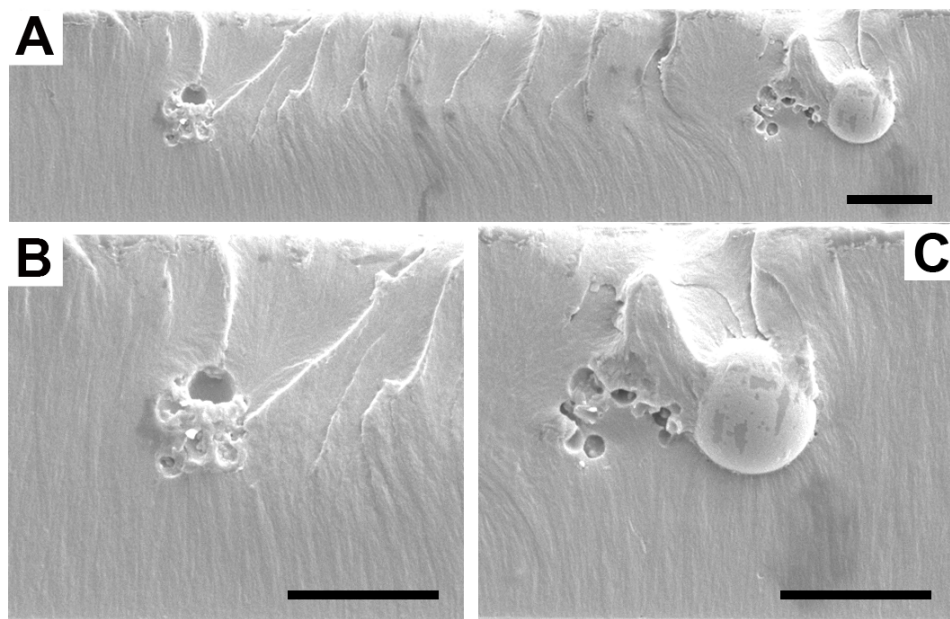


Figure 3.14 Escaping behavior of LCs in a planar-like region. SEM images of LCP inside a planar region in a homeotropic LC cell. (A) The fracture structure shows stabilization of disclination lines with silica colloids sitting at the two ends of the planar region, and the escaping behavior of LC director from right to left. (B-C) A close look at the director field surrounding the colloid. Scale bars: 5 μm

3.8 Conclusions

In conclusion, we designed and synthesized a new LCM system with strong dipole-dipole interactions, resulting in a stable nematic phase and precise control of molecular anchoring and alignment on different boundary conditions. The director field can be faithfully “locked” by photocrosslinking, allowing for direct mapping of the LC director field and defect structures by SEM. In turn, we can calculate the extrapolation length, and estimate the elastic and anchoring constants of LCs (Figure 3.10 and 3.11). This molecular design strategy can be extended to other substituents (e.g. to induce hydrogen bonding) and bridging groups that connect the mesogen and epoxy group in order to fine-tune the mesomorphic properties. Moreover, our LC monomers are low cost, e.g. LCM_X1 can be produced at a cost of approximately 10% that of 5CB, but with

equal flexibility to be aligned on various boundary conditions. This newfound ability provides us with new tools to enhance our understanding of anchoring, defects, and elasticity of short-molecule nematics, which will enable the further control of bulk structures *via* nanoscale patterning of the substrate and surface chemistry. We anticipate that by directly photopatterning a 2-D sheet of NLC elastomer or glass with embedded defects and elasticity, followed by actuation by heat or light, we could induce folding into 3-D.

3.9 Contributions

Y.X. and S.Y. conceived the ideas and designed the experiments. Y.X. synthesized the liquid crystal molecules and performed the experiments. F.S. helped the experiments and interpretation, and estimated the elastic constants. R.D.K, K.J.S. and S.Y. supervised the work. All the authors wrote the paper.

3.10 References

1. Higgins DA & Luther BJ (2003) Watching molecules reorient in liquid crystal droplets with multiphoton-excited fluorescence microscopy. *J. Chem. Phys.* 119(7):3935-3942.
2. Kachynski AV, Kuzmin AN, Prasad PN, & Smalyukh II (2007) Coherent anti-Stokes Raman scattering polarized microscopy of three-dimensional director structures in liquid crystals. *Appl. Phys. Lett.* 91(15):-.
3. Smalyukh II, Shiyankovskii SV, & Lavrentovich OD (2001) Three-dimensional imaging of orientational order by fluorescence confocal polarizing microscopy. *Chem. Phys. Lett.* 336(1-2):88-96.
4. Feller MB, Chen W, & Shen YR (1991) Investigation of surface-induced alignment of liquid-crystal molecules by optical second-harmonic generation. *Phys. Rev. A* 43(12):6778-6792.
5. Yelin D, Silberberg Y, Barad Y, & Patel JS (1999) Phase-Matched Third-Harmonic Generation in a Nematic Liquid Crystal Cell. *Phys. Rev. Lett.* 82(15):3046-3049.
6. Yoon DK, *et al.* (2007) Internal structure visualization and lithographic use of periodic toroidal holes in liquid crystals. *Nat. Mater.* 6:5.

7. Zhang C, *et al.* (2012) Direct observation of smectic layers in thermotropic liquid crystals. *Phys. Rev. Lett.* 109.
8. Gao M, *et al.* (2014) Direct observation of liquid crystals using cryo-TEM: specimen preparation and low-dose imaging. *Microscopy Res. and Technique* 77:19.
9. Yoon DK, *et al.* (2013) Three-dimensional textures and defects of soft material layering revealed by thermal sublimation. *Proc. Natl. Acad. Sci.* 110(48):19263-19267.
10. Costello MJ, Meiboom S, & Sammon M (1984) Electron microscopy of a cholesteric liquid crystal and its blue phase. *Phys. Rev. A* 29(5):2957-2959.
11. Livolant F & Bouligand Y (1989) Freeze-fractures in cholesteric mesophases of polymers. *Mol. Cryst. Liq. Cryst.* 166:10.
12. Bouligand Y (1972) Twisted fibrous arrangements in biological materials and cholesteric mesophases *Tissue Cell* 4:29.
13. Donald AM, Viney C, & Windle AH (1983) Banded structures in oriented thermotropic polymers. *Polymer* 24(2):155-159.
14. Mitchell GR & Windle AH (1982) Structural analysis of an oriented liquid crystalline copolyester. *Polymer* 23(9):1269-1272.
15. Cavallaro M, *et al.* (2013) Exploiting imperfections in the bulk to direct assembly of surface colloids. *Proc. Natl. Acad. Sci.* 110(47):18804-18808.
16. Bishop DJ, Gammel PL, Huse DA, & Murray CA (1992) Magnetic flux-line lattices and vortices in the copper oxide superconductors. *Science (New York, N.Y.)* 255(5041):165-172.
17. Tchernyshyov O & Chern G-W (2005) Fractional Vortices and Composite Domain Walls in Flat Nanomagnets. *Phys. Rev. Lett.* 95(19):197204.
18. Kibble TWB (1976) Topology of cosmic domains and strings. *J. Phys. A: Math. General* 9(8):1387.
19. Nikkhou M, *et al.* (2015) Light-controlled topological charge in a nematic liquid crystal. *Nat. Phys.* 11(2):183-187.
20. Modes CD, Bhattacharya K, & Warner M (2010) Disclination-mediated thermo-optical response in nematic glass sheets. *Phys. Rev. E* 81(6):060701.
21. Ware TH, McConney ME, Wie JJ, Tondiglia VP, & White TJ (2015) Voxelated liquid crystal elastomers. *Science (New York, N.Y.)* 347(6225):982-984.
22. Zhang Y, Lo C-W, Taylor JA, & Yang S (2006) Replica Molding of High-Aspect-Ratio Polymeric Nanopillar Arrays with High Fidelity. *Langmuir* 22(20):8595-8601.
23. Warenghem M (1982) A Test for Surface Energy Anisotropy Sign Determination. *Mol. Cryst. Liq. Cryst.* 89(1-4):15-21.
24. Klaus JW & George SM (2000) SiO₂ chemical vapor deposition at room temperature using SiCl₄ and H₂O with an NH₃ catalyst. *J. Electrochem. Soc.* 47(7):2658-2664.
25. Dierking I (2010) Recent developments in polymer stabilised liquid crystals. *Polym. Chem.* 1(8):1153-1159.
26. Dierking I & Archer P (2013) Imaging liquid crystal defects. *RSC Adv.* 3:5.
27. Broer DJ, Bastiaansen CMW, Debijs MG, & Schenning APHJ (2012) Functional Organic Materials Based on Polymerized Liquid-Crystal Monomers: Supramolecular Hydrogen-Bonded Systems. *Angew. Chem. Int. Ed.* 51(29):7102-7109.
28. Küpfer J & Finkelmann H (1991) Nematic liquid single crystal elastomers. *Makromol. Chem. Rapid. Commun.* 12(12):717-726.

29. Ohm C, Brehmer M, & Zentel R (2010) Liquid Crystalline Elastomers as Actuators and Sensors. *Adv. Mater.* 22(31):3366-3387.
30. Thomsen DL, *et al.* (2001) Liquid Crystal Elastomers with Mechanical Properties of a Muscle. *Macromolecules* 34(17):5868-5875.
31. Yu Y, Nakano M, & Ikeda T (2003) Photomechanics: Directed bending of a polymer film by light. *Nature* 425(6954):145-145.
32. Warner M & Terentjev EM (2003) *Liquid crystal elastomers* (Clarendon Press, Oxford).
33. J. BD, P. CG, & S. Z (2011) *Cross-Linked Liquid Crystalline Systems: From Rigid Polymer Networks to Elastomers* (CRC Press, New York).
34. Petrov VF & Shimizu Y (2001) Nitro substitution in achiral calamitic liquid crystals. *Liq. Cryst.* 28(11):1627-1647.
35. Dewar MJS & Goldberg RS (1970) Effects of central and terminal groups on nematic mesophase stability. *J. Org. Chem.* 35(8):2711-2715.
36. Lee JY, Jang J, Hong SM, Hwang SS, & Kim KU (1999) Relationship between the structure of the bridging group and curing of liquid crystalline epoxy resins. *Polymer* 40(11):3197-3202.
37. Minkin VI, Osipov OA, & Zhdanov YA (1970) *Dipole Moments in Organic Chemistry* (Plenum Press, New York).
38. Zuev VV & de Vekki DA (2006) Catalytic isomerization of terminal olefins in liquid-crystalline polyesters at hydrosilylation with 1-(1'-arylethoxy)-1,1,3,3-tetramethyldisiloxanes. *Russ. J. Org. Chem.* 42(8):1105-1112.
39. Faetti S (1998) The effects of curvature on nematic liquid crystals confined in a cylindrical cavity. *Phys. Lett. A* 237(4-5):264-270.
40. Crawford GP, Allender DW, & Doane JW (1992) Surface elastic and molecular-anchoring properties of nematic liquid crystals confined to cylindrical cavities. *Phys. Rev. A* 45(12):8693-8708.
41. Shaw JM, Gelorme JD, LaBianca NC, Conley WE, & Holmes SJ (1997) Negative photoresists for optical lithography. *IBM J. Res. Dev.* 41(1.2):81-94.
42. Ito H (1997) Chemical amplification resists: history and development within IBM. *IBM J. Res. Dev.* 41(1-2):69-80.
43. Broer DJ, Lub J, & Mol GN (1993) Synthesis and photopolymerization of a liquid-crystalline diepoxide. *Macromolecules* 26(6):1244-1247.
44. Jahromi S, Lub J, & Mol GN (1994) Synthesis and photoinitiated polymerization of liquid crystalline diepoxides. *Polymer* 35(3):622-629.
45. van Oosten CL, Bastiaansen CWM, & Broer DJ (2009) Printed artificial cilia from liquid-crystal network actuators modularly driven by light. *Nat. Mater.* 8(8):677-682.
46. Berreman DW, Meiboom S, Zasadzinski JA, & Sammon MJ (1986) Theory and Simulation of Freeze-Fracture in Cholesteric Liquid Crystals. *Phys. Rev. Lett.* 57(14):1737-1740.
47. Zasadzinski JAN & Bailey SM (1989) Applications of freeze - fracture replication to problems in materials and colloid science. *J. Electron. Microsc. Tech.* 13(4):309-334.
48. Hudson SD & Thomas EL (1989) Frank Elastic-constant anisotropy measured from transmission electron microscope images of disclinations. *Phys. Rev. Lett.* 62:5.

49. Scharkowski A, Crawford GP, Žumer S, & Doane JW (1993) A method for the determination of the elastic constant ratio K_{33}/K_{11} in nematic liquid crystals. *J. Appl. Phys.* 73(11):7280-7287.
50. Barbero G, Madhusudana NV, & Durand G (1984) Weak anchoring energy and pretilt of a nematic liquid crystal. *J. Phys. Lett.* 45(12):613-619.
51. Lapointe CP, Mason TG, & Smalyukh II (2009) Shape-Controlled Colloidal Interactions in Nematic Liquid Crystals. *Science (New York, N.Y.)* 326(5956):1083-1086.
52. Senyuk B, *et al.* (2013) Topological colloids. *Nature* 493(7431):200-205.
53. Poulin P, Stark H, Lubensky TC, & Weitz DA (1997) Novel Colloidal Interactions in Anisotropic Fluids. *Science (New York, N.Y.)* 275(5307):1770-1773.
54. Mušević I, Škarabot M, Tkalec U, Ravnik M, & Žumer S (2006) Two-Dimensional Nematic Colloidal Crystals Self-Assembled by Topological Defects. *Science (New York, N.Y.)* 313(5789):954-958.

CHAPTER 4: Better Actuation Through Chemistry: Using Surface Coatings to Create Uniform Director Fields in Nematic Liquid Crystal Elastomers

Yu Xia, Elaine Lee, Hao Hu, Mohamed Amine Gharbi, Daniel A. Beller, Eva-Kristina Fleischmann, Randall D. Kamien, Rudolf Zentel, Shu Yang, manuscript submitted to *Angew. Chem. Int. Ed.* 2016 (under review).

4.1 Introduction

Because of their geometrical, mechanical, and electronic anisotropy, liquid crystal (LC) molecules are not only highly sensitive to external aligning fields but can also exquisitely control the propagation of electromagnetic phenomena. Consequently, LC molecules have long been of interest for scientific advancement and technological applications, including displays, artificial muscles, and actuators that rely upon anisotropic properties of LC molecules.¹⁻⁴ It is known that nematic liquid crystalline elastomers (NLCEs) exhibit a spontaneous contraction along the director axis when heated above their nematic (N) – isotropic (I) phase-transition temperatures (T_{NI}), and the polymer chain adopts an, on-average, spherical conformation.⁵ Therefore, NLCEs have a reversible shape memory effect when triggered by external stimuli, including heat, UV light, and electric fields⁶⁻¹⁰. However, the deformation of LCE networks is highly dependent on the molecular alignment of LC molecules, both globally and locally, on the boundary conditions imposed at interfaces by topography, topology, and surface chemistry, as well as on the application of an external field¹¹⁻¹³.

Coupling of responsive materials with patterned surfaces at the micro- and nano-scale has led to interesting surface properties, including tunable structural color and transparency¹⁴⁻¹⁹, tunable dry adhesion²⁰⁻²², and switchable wettability²³⁻²⁵. To achieve a

large and reversible strain in micro-structured LCE actuators⁷⁻⁹, it is critically important to control LC anchoring within the pattern at the molecular level. The most common techniques to control LC anchoring include rubbing the substrate and application of a magnetic field before the LCMs are crosslinked. Rubbing is effective when preparing non-patterned LCE where the LC molecules align along the formed microgrooves.^{6, 26, 27} However, it is difficult to apply rubbing on a micro- and nano-structured template to align LCEs. Moreover, the generation of static charge and scratches often interferes with the LC alignment within the microgrooves.

Keller *et al.* first demonstrated the fabrication and actuation of NLCE micropillar arrays using a poly(dimethylsiloxane) (PDMS) mold with cylindrical pores (20 μm in diameter and 100 μm in height) by applying a magnetic field (1-1.5 Tesla) to align LCs vertically along the film thickness, although alignment was not confirmed by polarized optical microscopy (POM) images in those early reports.^{28, 29} A large contraction strain (~35%) was generated when actuating the pillars above T_{NI} (120°C) for micropillars made of side-chain NLCEs³⁰. Nevertheless, detailed investigation (both experimentally and theoretically) of LC anchoring within a soft lithography template such as PDMS mold remains lacking. In part it is because, compared to a flat substrate, micro-patterned PDMS molds provide much more complicated surface topographies to control the LC anchoring uniformly over the entire sample area -- so called monodomain LC anchoring. When the dimension of the surface topography shrinks to micron size, the surface effect become increasingly important. Given the wide range of potential applications of structured NLCEs, it is pressing to understand and eventually precisely control LC anchoring under confinement of a PDMS mold during soft lithography through surface

topography and surface chemistry vs. the use of an external field.

Here we prepared NLCE micropillars (diameter of 10 μm , pitch of 20 μm , and height of 40 μm) by polymerizing the NLC monomer, (4''-acryloyloxybutyl)-2,5-di-(4'-butyloxybenzoyloxy) benzoate (LCM4), pre-aligned in a surface-treated PDMS mold. To generate a uniform, defect free monodomain nematic configuration of vertically aligned LCM4 within the pores, it is important to promote planar anchoring of LCM4 inside the molds. We checked the LC alignment using both small molecule NLC, 4-Cyano-4'-pentylbiphenyl (5CB) and the unpolymerized LCM4 under polarized optical microscopy (POM). We corroborate the POM observations with Landau-de Gennes numerical modeling, which simulates the LC alignment with both homeotropic and planar anchoring within the PDMS mold. In all cases, we found that perfect alignment of the LC director field along the pillar thickness could only be achieved with planar anchoring surface chemistry. To confirm this experimentally, we coated a thin layer of poly(2-hydroxyethyl methacrylate) (PHEMA) onto the PDMS mold to create degenerate planar surface anchoring for both LCM4 and 5CB. In comparison, in untreated PDMS molds, both NLCs maintained homeotropic anchoring at the interfaces and the director exhibited radial escape into the third dimension³¹. The NLCE pillars with planar anchoring demonstrated a relatively large radial strain ($\sim 30\%$) during heating across T_{NI} , while those created with homeotropic alignment had smaller strains due to the inherent frustration of the nematic texture within the pillars.

4.2. Experiment methods

4.2.1 Materials

(4''-acryloyloxybutyl)-2,5-di-(4'-butyloxybenzoyloxy)benzoate (LCM4) was synthesized according to the literature³. N,N-dimethyl-n-octadecyl-3-amino-propyltrimethoxysilyl chloride (DMOAP), hydroxyethyl methacrylate (HEMA), 1,6-hexane-diol diacrylate and 4-Cyano-4'-pentylbiphenyl (5CB) were purchased from Sigma Aldrich and used as received. Photoinitiator, Irgacure®184 (1-hydroxy cyclohexyl phenyl ketone), was obtained from Ciba Specialty Chemicals.

4.2.2 Preparation of PDMS molds

The PDMS porous membrane (diameter of 10 μm , pitch, or center-to-center distance of 20 μm , and depth of 40 μm) was replicated from the epoxy (D.E.R. 354, Dow Chemical) pillar master, following the protocol reported earlier³².

4.2.3 Preparation of PDMS molds with different surface chemistry

The as-cured PDMS porous membranes offered homeotropic anchoring to LCM4 and 5CB, and were used as control substrates. To prepare a planar anchoring surface, the PDMS mold was immersed into a solution consisting of Irgacure®184 (30 wt%) in acetone for 30 min, followed by rinsing with acetone three times and drying by air gun. The PDMS mold was then immersed into neat HEMA liquid and exposed under UV light (365 nm, Hg lamp) at a dosage of 1000 mJ/cm^2 . The resulting mold was rinsed by ethanol three times to remove unreacted HEMA monomers, followed by drying on a hot stage at 95 °C.

4.2.4 Preparation of DMOAP coated glass substrates

Glass slides were pre-cleaned by washing with ethanol and acetone twice, respectively.

They were then immersed into an aqueous solution of DMOAP (1 vol%) for 30 min, followed by rinsing with DI water three times and baking at 110 °C in an oven for 1 h.

4.2.5 Preparation of 5CB in the PDMS mold

One drop of 5CB (~ 5 μ L) was placed on the pre-cleaned glass slide, and the PDMS mold (treated or untreated) was applied on top. After filling the mold with 5CB by capillary force for 1 min, the PDMS mold was lifted and bladed with a razor blade on the top surface to remove the residual 5CB. Then a DMOAP treated glass slide was placed on top of the PDMS mold, and the sample filled with 5CB was characterized by POM.

4.2.6 Fabrication of LCM4 pillars

LCM4 and 1,6-hexanediol diacrylate (as a crosslinker) were first mixed at a molar ratio of 4:1 in dichloromethane (20 wt%) to obtain a homogeneous solution, followed by addition of 2 wt% of photoinitiator (Irgacure® 184). 20 μ L of the mixture was drop-cast on a clean glass slide and dried under vacuum. The mixture was then covered by the PDMS mold heated to 110 °C on a hot stage for 10 min. After the pores of the mold were completely filled with LCM4, the glass slide was carefully removed, and a razor blade was used to scrape off the residual LCs. The PDMS mold filled with LCM4 was then placed on a DMOAP treated glass substrate, and examined under POM to check LC anchoring before UV exposure. The PDMS mold along with LC monomers was exposed to 365 nm UV light (97435 Oriel Flood Exposure Source from Newport, intensity of 54 mW/cm²) at 17, 000 mJ/cm² dosage, followed by removal of the DMOAP coated glass substrate. The sample was then placed on top of a thin layer of polyurethane acrylate (PUA) liquid (Minuta Technology) on a clean glass slide, and exposed with another 17,000 mJ/cm² dosage of UV light to bond PUA onto pillars. After the sample was cooled

to room temperature, the PDMS mold was peeled off to obtain the LCE pillars supported on a PUA thin film. Here, the PUA supporting layer (more rigid than PDMS) helps to pull the LCE pillars out of the PDMS mold, much like the use of poly(methyl methacrylate) (PMMA) layer in the literature³³.

4.2.7 Polarized optical microscopy

The LC textures were observed by an Olympus BX61 motorized optical microscope with crossed polarizers using CellSens software.

4.2.8 Water contact angle measurement

Water contact angle was measured from a 5 μ L water droplet placed on a flat PDMS film coated with PHEMA polymerized at different UV dosages using a model 200 Ramé-Hart standard automated goniometer with sessile drop method. For each water contact angle reported in Figure 4.3, it was averaged over three measurements at different locations of the sample.

4.2.9 Landau-de Gennes numerical modeling

Numerical modeling of LC alignment within the PDMS mold was performed on 5CB as a model LC according to literature³⁴ using the Frank elastic constants of 5CB at 298K,³⁵ $K_1 = 0.64 \times 10^{-11}$ N (splay), $K_2 = 0.3 \times 10^{-11}$ N (twist), and $K_3 = 1 \times 10^{-11}$ N (bend). The simulation box to model 5CB in cylindrical pores was set as diameter 352 nm and height 1408 nm; the size is smaller than experiments due to the calculation time. The aspect ratio (height/diameter) of the pores is 4, the same as that in the sample.

4.3 Landau-de Gennes numerical modeling

To fabricate monodomain LCE microstructures by soft lithography, researchers

mainly rely on magnetic fields to align LCs using a non-treated PDMS mold^{8, 30, 36}. The freshly prepared PDMS surface has a low surface energy (~ 20 mJ/m²). The commonly used small molecule NLC, *e.g.* 5CB, has weak homeotropic anchoring on the PDMS surface. To understand the effect of surface chemistry in aligning NLCs, we first simulated the anchoring of 5CB in a PDMS pore using Landau-de Gennes numerical modeling. As seen in Figure 4.1, 5CB filled in the untreated PDMS mold adopts the classic radial escape into the third dimension (Figure 4.1a). To achieve full vertical alignment of the director in the PDMS pore, an external magnetic field has been used. The effect of a magnetic field can be quantified by the magnetic coherence length, ξ_H , the lengthscale over which the LC director can orient and reorient along the field direction, given by:

$$\xi_H = \sqrt{\frac{K_3}{\Delta\chi H^2}} \quad (4-1)$$

where K_3 is the bend elastic constant of LC, $\Delta\chi$ is the anisotropic magnetic susceptibility, and H is the magnetic field strength. In the case of a small molecule LC such as 5CB, K_3 is on the order of 10^{-11} N and $\Delta\chi$ is on the order 10^{-7} .³⁷ Thus, with a magnetic field strength $H \sim 10^6$ A/m (~ 1 Tesla), 5CB with any boundary conditions can be reoriented on a length scale $\xi_H \sim 10$ nm. Therefore, a strong magnetic field could be quite effective in aligning 5CB molecules into monodomains in the PDMS pores. However, this is not the case for NLC monomers such as LCM4, which often fail to be fully aligned within the pores by magnetic field. Radially escaping configurations of LCM4 in PDMS pores under an 1.5 Tesla vertical magnetic field have been reported⁸:

however, the exact mechanism remains unclear, since neither the elastic constants of LCM4 nor its magnetic susceptibility has been precisely measured. Recall that in the nematic elastomers, there is different shape transformation parallel and perpendicular to the local director field. Thus, in the escaped configuration, large strains cannot be achieved because of the radial variation of the LC texture. With our desire to create pillars with a large strain response when heated across T_{NI} , we seek, instead, a nematic texture that generates a cooperative shape transformation. However, planar anchoring alone on the PDMS mold surface presents a potential problem – the bottom of a cylindrical pore would disfavor a uniform nematic texture parallel to the cylinder axis. Our numerical modeling, however, finds that this issue is limited to the bottom of the pore for 5CB (Figure 4.1b). If we can create and maintain this nematic texture in LCM4 during photopolymerization, it is possible to achieve a large strain without the use of an aligning magnetic field – purely through interfacial chemistry!

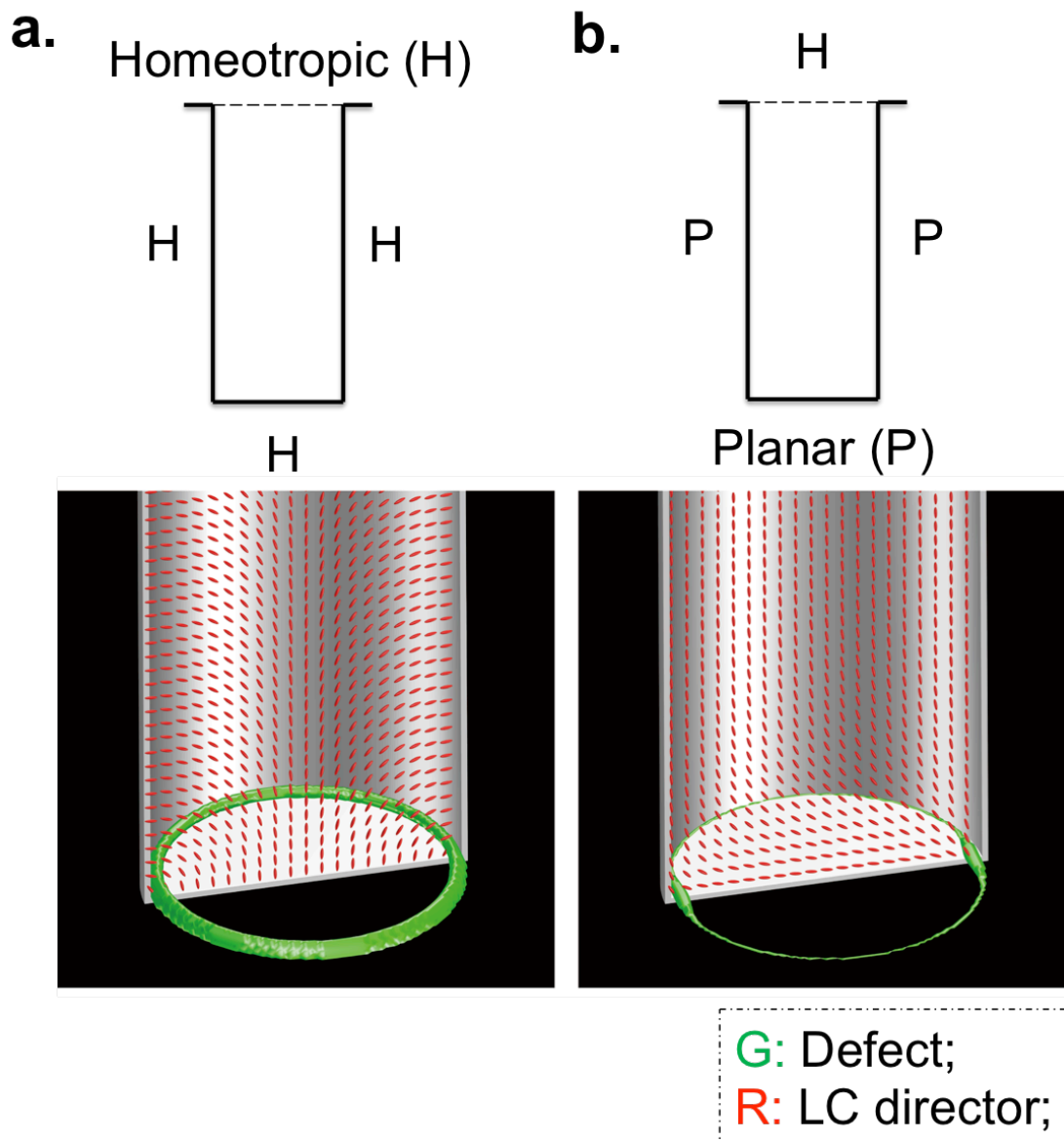


Figure 4.1 Landau-de Gennes numerical modeling of 5CB in a PDMS mold with (a) homeotropic anchoring and (b) planar anchoring.

4.4 Control of liquid crystal surface anchoring

Indeed, when we grafted a thin layer of PHEMA on the PDMS mold we induced planar anchoring of the LCs (Figure 4.2a). While planar anchoring of LCs on a glass slide is usually achieved by absorbing a thin layer of poly(vinylalcohol) (PVA) or polyimide

(PI) on the substrate, it is challenging to uniformly coat hydrophilic polymers, *i.e.* PVA or PI, on a hydrophobic PDMS mold. To circumvent this we first treated the mold with an acetone solution of photoinitiator (Irgacure®184), which we expected to be partially trapped within the mold surface (since PDMS is slightly swollen by acetone with a swelling ratio $\sim 1.03^{38}$). The PDMS mold was then immersed into HEMA monomers that wet the PDMS surface, followed by UV curing at different dosages.

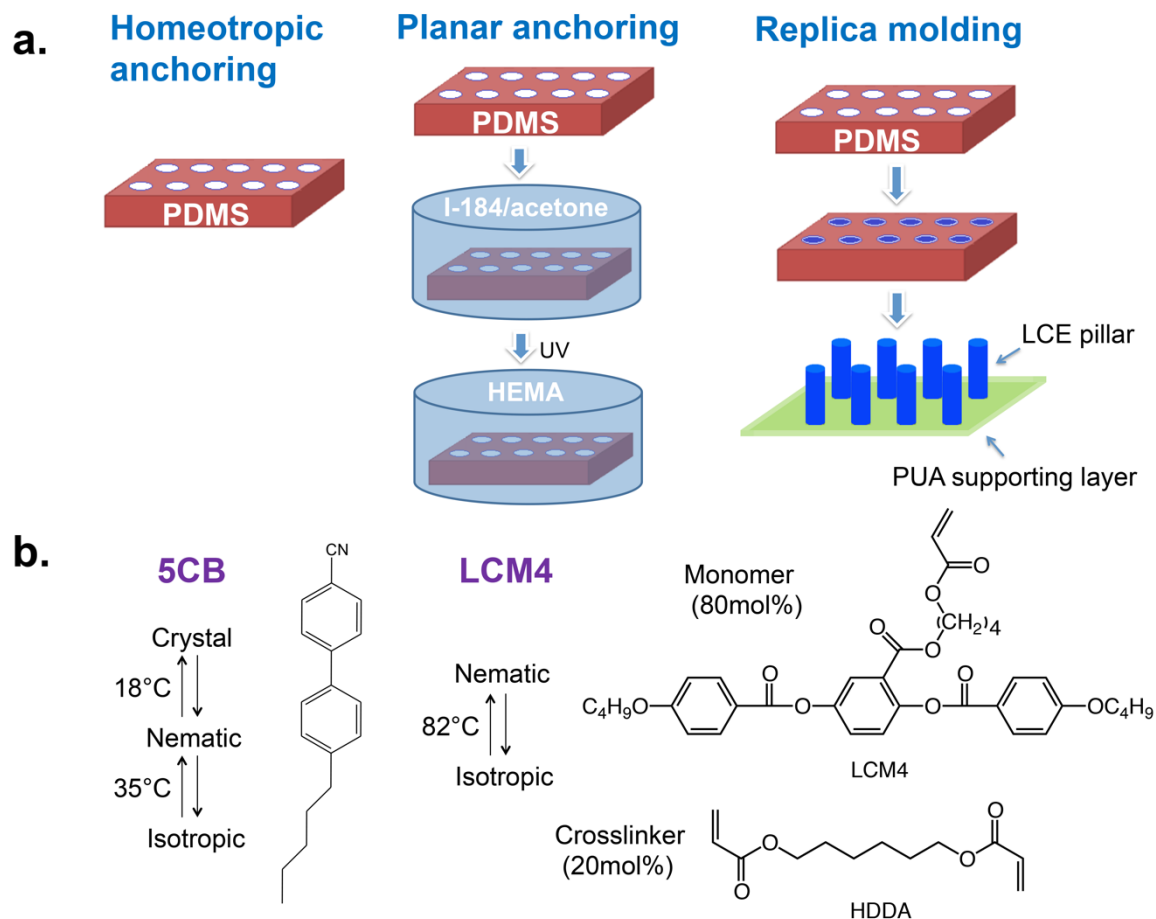


Figure 4.2 (a) Schematic illustrations of the preparation of the PDMS molds with different surface chemistry and the fabrication of LCE pillar array. Pillar dimensions: diameter, 10 μm , pitch (center-to-center distance), 20 μm and height, 40 μm . (b) Chemical structures of LC systems used in the experiments.

To ensure complete coverage of PHEMA on the PDMS mold, we monitored the

water contact angles of the treated molds prepared at different UV dosages (Figure 4.3). At low UV dosages (≤ 800 mJ/cm^2), the water contact angle of the mold was found greater than 50° . At 1000 mJ/cm^2 , the lowest water contact angle ($\sim 27^\circ$) was achieved, suggesting sufficient coverage and polymerization of PHEMA on PDMS. At a higher dosage ($1,500$ mJ/cm^2), the water contact angle increased again, possibly due to condensation/crosslinking of the hydroxyl groups on PDMS.

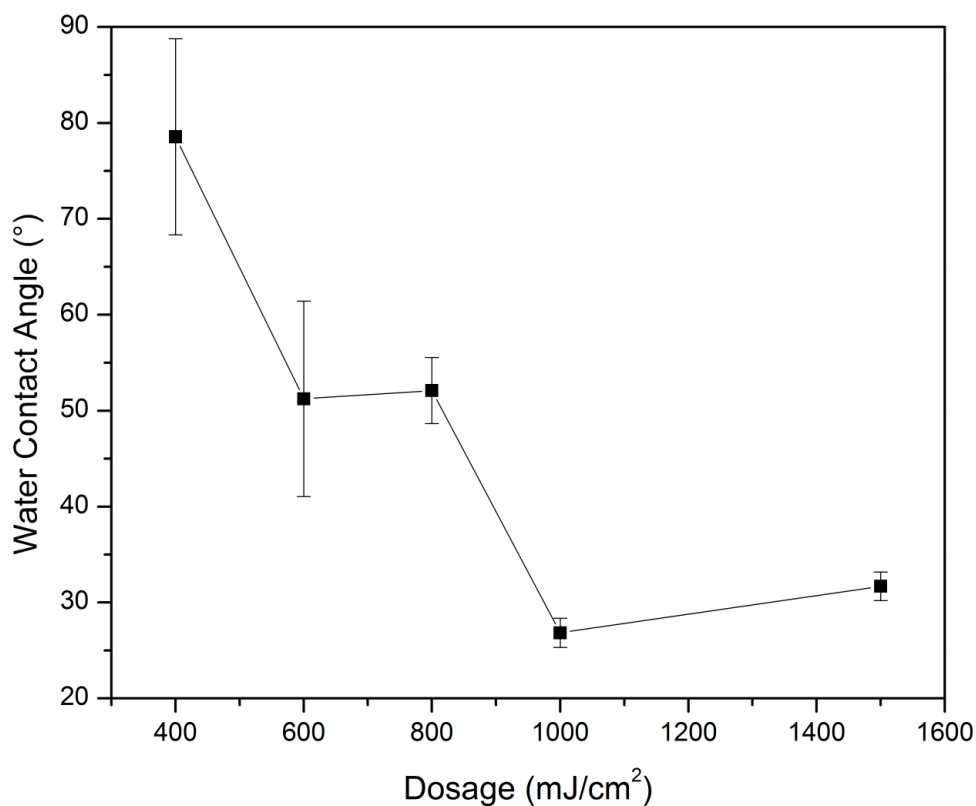


Figure 4.3 Average water contact angles on PHEMA coated PDMS exposed to different UV dosages.

The cured PHEMA has very similar chemistry to PVA as they both have one hydroxyl group in each repeat unit. As evident from Figure 4.4, 5CB molecules and LCM4 monomers had planar anchoring in porous mold made of pure PHEMA, where the directors were nearly all vertically aligned.

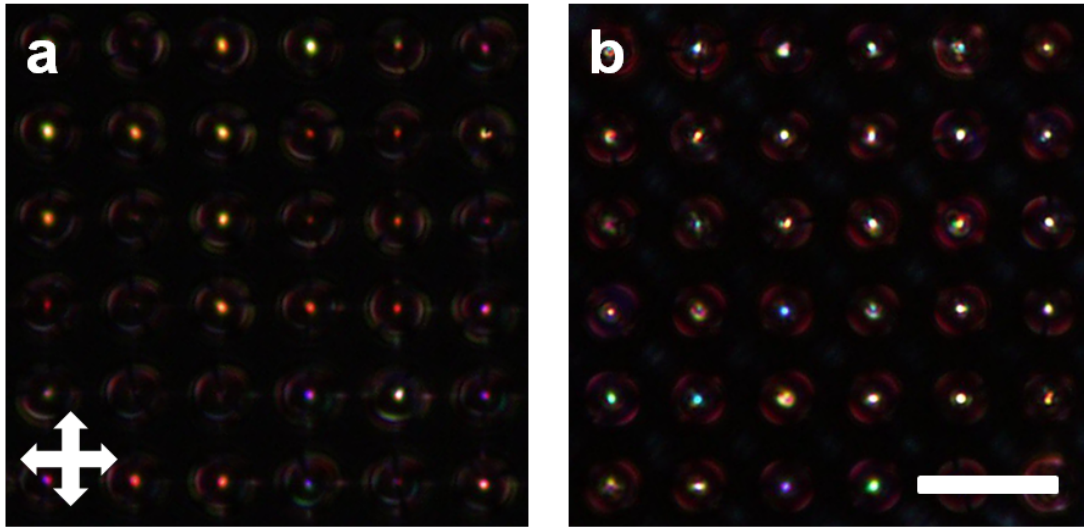


Figure 4.4 POM images of 5CB (a) and LCM4 (b) in a PHEMA porous mold with pore diameter 10 μm , pitch 15 μm , and depth 20 μm . Vertical alignments of LC molecules were observed in both LC systems. Scale bar: 20 μm .

We then investigated the anchoring of 5CB and LCM4 in the PDMS molds under POM. We used 5CB to establish baseline expectations. As predicted by numerical modeling (Figure 4.1), 5CB in the PDMS mold attains an escaped configuration under homeotropic anchoring and vertical alignment under planar alignment. As sketched in Figure 4.5a, alignment of 5CB should generate two disclination loops at the top edge and bottom corners of the mold. The escaped configuration has lower energy and will appear as a ± 1 planar defect under POM – the standard four-brush texture, as shown in Figure 4.5b. Under planar anchoring, the numeric suggests that 5CB molecules will be mostly vertically aligned with director distortion only occurring at the bottom of the mold but with no disclination line on the top edge (see Figure 4.5d). Thus, under POM, the image should be dark with light transmitted only from the texture at the bottom of the mold, in agreement with the experimental observation (see Figure 4.5e).

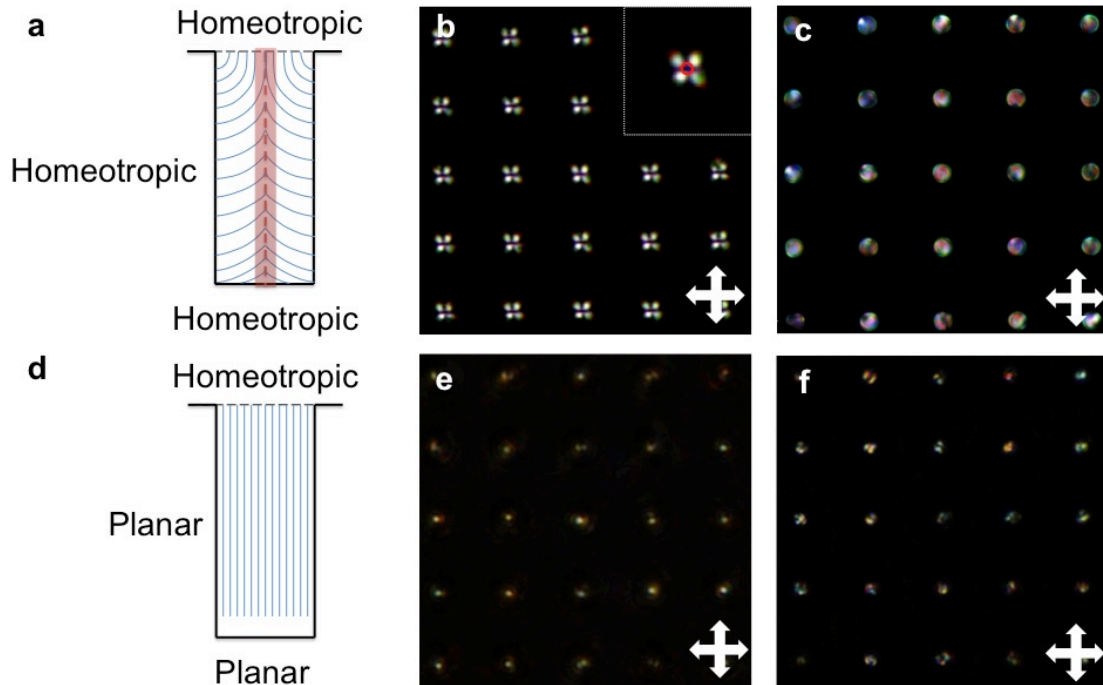


Figure 4.5 (a) Schematic of the LC disclination line in a mold with homeotropic anchoring. The red dotted line indicates the escape of the LC director, while the red shaded region indicates the width of the escaping configuration, where the director field is uniformly vertical. (b-c) POM images of (b) 5CB and (c) LCM4 under homeotropic anchoring in the PDMS mold. Inset in (b): LC escaping domain indicated by the red circle under cross polarizers when observing the sample from the top under POM. (d) Schematic of the disclination line of 5CB in a PDMS mold treated with planar anchoring chemistry. (e-f) POM images of (e) 5CB and (f) LCM4 in a planar-anchored PDMS mold.

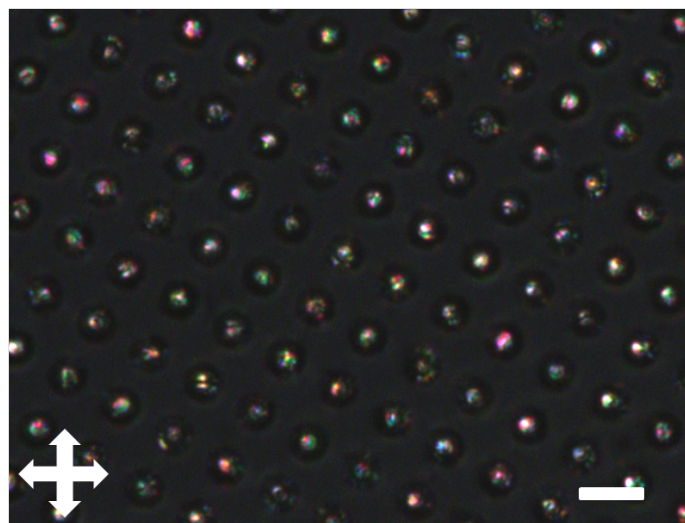


Figure 4.6 POM image showing polydomain alignment of LCM4 in a non-treated PDMS porous mold. Scale bar: 20 μm

We now turn to LCM4 (before polymerization). In the case of homeotropic anchoring, a polydomain texture lacking a simple cross with each pore was observed under POM (Figure 4.5c & 4.6) as a result of non-uniform light transmittance. It has been reported that the standard escaped radial structure can be achieved by applying a vertical magnetic field from a 1.5T permanent magnet⁸. Fortunately, in the case of planar anchoring (Figure 4.5f) we achieved the target texture – a match to that of 5CB as seen in Figure 4.5e.

4.5 Actuation of cross-linked LCEs

So do we get the desired effect? We carefully crosslinked LCM4 within the mold under planar anchoring and POM observation confirmed that mono-domain alignment of LCM4 within the pillars was maintained. The tops of the extracted pillars now show the texture on the bottom of the molds, revealing topological defects seen in Figure 4.7a-b. To better understand the LCM4 alignment within the mold and how these defects were formed when LCM4 infiltrated the PDMS mold, we performed Landau-de Gennes numerical modeling of 5CB (Figure 4.8). The observed defects arise from the planar anchoring of the monomer to the PDMS mold at the bottom of each micro-hole. When planar anchoring is weak (Figure 4.8a), no defect appears either in the bulk or at the boundary. When planar anchoring strength is increased (b-d), defects start to arise from the corner of the pore: the line defect at the corner (Figure 4.8b) gradually shrinks down to two point defects as seen in Figure 4.8d). From Figure 4.4, we show how 5CB in planar anchoring shows line defects at the corner, a configuration close to the simulation result in Figure 4.8b, indicating the two systems have similar surface anchoring

contributions to the LC director orientation. Therefore, we can estimate the surface anchoring strength of 5CB in PHEMA treated PDMS pores from simulation. Since the simulation box is ~ 30 times smaller than the actual pore size in experiment, the experimental data suggests that the planar anchoring strength for 5CB in a PHEMA treated pore is roughly $\frac{7.74 \times 10^{-4} \text{ J/m}^2}{30} \sim 10^{-5} \text{ J/m}^2$. Here, since 5CB and LCM4 showed similar anchoring configuration in PHEMA treated pores (Figure 4.4), we used the analogy between 5CB and LCM4 to estimate the relative planar anchoring strength of LCM4 in PHEMA coated pores as $\sim 10^{-5} \text{ J/m}^2$, suggesting a relatively weak planar anchoring.

Finally, across T_{NI} , we find a relatively large strain in the radial direction ($\sim 30\%$) measured from the diameters in the middle of the pillars at 50°C and 110°C , respectively (see Figure 4.7c-d). Our result is consistent with that from the strain induced in LCM4 nano-fibers ($\sim 300 \text{ nm}$ in diameter, $6 \mu\text{m}$ in length) templated from an anodic aluminum oxide (AAO) membrane with 20 mol% crosslinker³⁹. Similar to PHEMA, the AAO surface is rich in hydroxyl groups, providing planar anchoring of LCM4. When the actuation of the LCM4 pillars was characterized in a top view under the bright field (BF) microscopy (see Figure 4.7e), a 30% radial strain was measured, similar to that observation from Figure 4.7b. We note that when heated above T_{NI} , the pillars tilted slightly at 110°C , which could be attributed to the different thermal expansion coefficients between the polyurethane (PUA) supporting layer and LCM4 pillars.

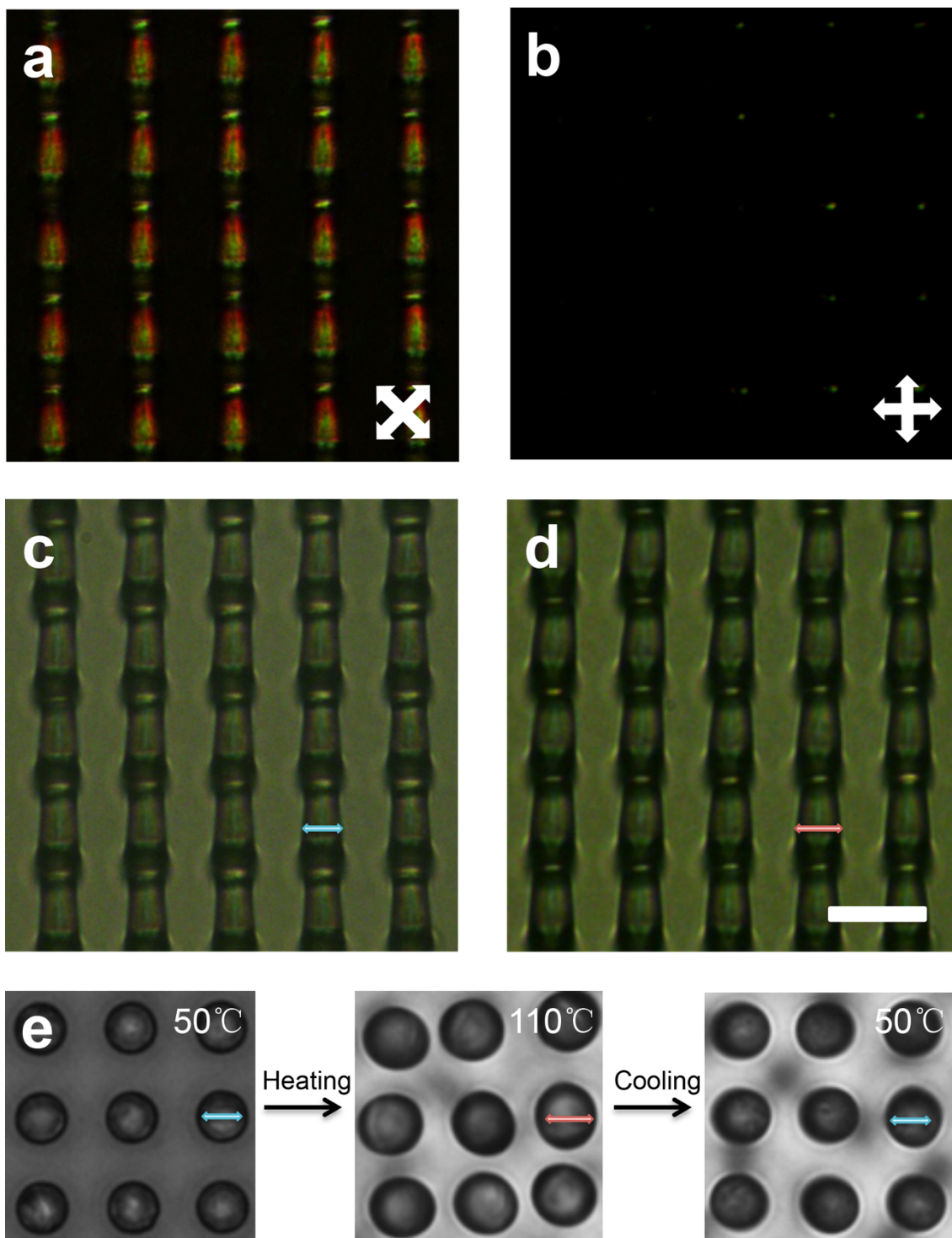


Figure 4.7 (a-b) Cross-sectional views of POM images of LCM4 pillars after UV curing viewed at (a) 45° and (b) 0° polarization angles. (c-d) Cross-sectional views of BF images of LCM4 pillars at 50°C (c) and 110°C (d). (e) Top-view BF image of LCM4 pillars through a heating and cooling cycle. Blue and Red arrows in (c-e) indicate the position of pillars for measurement of diameter at 50°C and 110°C , respectively. Length of arrow: blue- $8.6\ \mu\text{m}$, red- $11.1\ \mu\text{m}$. Scale bar: $20\ \mu\text{m}$.

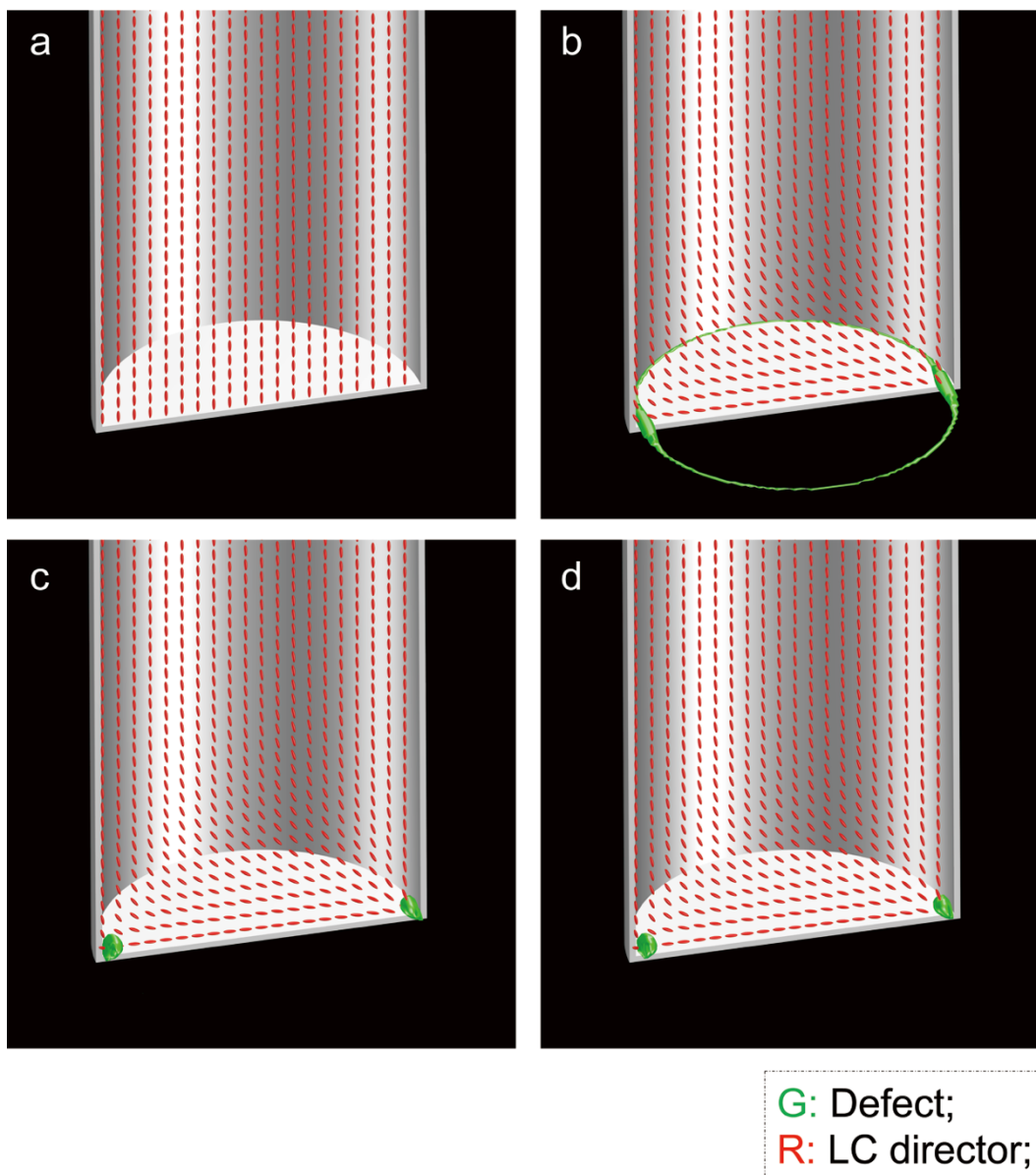


Figure 4.8 Landau-de Gennes numerical modeling of 5CB in a PDMS mold with planar anchoring strength of (a) $7.74 \times 10^{-5} \text{ J/m}^2$, (b) $7.74 \times 10^{-4} \text{ J/m}^2$, (c) $7.74 \times 10^{-3} \text{ J/m}^2$, and (d) $3.87 \times 10^{-2} \text{ J/m}^2$.

4.6 Conclusions

We successfully prepared LCE micropillars with uniform LC alignment by manipulating the surface chemistry of the PDMS mold for soft lithography. By coating the mold with PHEMA, we switched the PDMS mold surface from hydrophobic to

hydrophilic, thus altering the LC anchoring from weakly homeotropic to planar for both 5CB and LCM4. In turn, highly uniform mono-domains of LC alignment along the film thickness were obtained. After crosslinking LCM4 monomers imbedded in the mold, the LC director in the resulting LCE pillars was maintained, leading to a large radial strain (~30%) across T_{NI} . Compared to the application of a magnetic field, we believe that the use of interfacial chemistry of a patterned mold in soft lithography is, in some ways, much simpler and more elegant to direct LC alignment over a large area, specifically in the case of more complex systems, such as porous membranes, channels, and 3D. By combining topography and interfacial chemistry to manipulate the boundary conditions within the micro- and nanostructures, we expect to induce a rich library of LCE actuation behaviors for a variety of potential applications, including sensors, tunable wetting and adhesion, photonic displays, and *origami* assembly.

4.7 Contributions

Y.X., E.L., and H.H. performed the liquid crystal elastomer experiments and data analysis. Y.X. performed simulation of LCM4 in pillars using the code developed by D.A.B., and R.D.K., who also provided theoretical insights. M.A.G. participated in discussion and provided physical insights of experiments. E.F., and R.D.Z. provided initial LCM4 materials for testing the concept, while Y.X. later synthesized large quantities of LCM4 to carry out the experiments reported here.

4.8 References

1. Warner M & Terentjev EM (2003) *Liquid Crystal Elastomers* (Oxford University Press, Oxford) p 424.
2. Spillmann CM, Naciri J, Chen M-S, Srinivasan A, & Ratna BR (2006) Tuning the

- physical properties of a nematic liquid crystal elastomer actuator. *Liq. Cryst.* 33(4):373 - 380.
3. Thomsen DL, *et al.* (2001) Liquid Crystal Elastomers with Mechanical Properties of a Muscle. *Macromolecules* 34(17):5868-5875.
 4. Li M-H & Keller P (2006) Artificial muscles based on liquid crystal elastomers. *Phil. Trans. R. Soc. A* 364(1847):2763-2777.
 5. Jin LH, Lin Y, & Huo YZ (2011) A large deflection light-induced bending model for liquid crystal elastomers under uniform or non-uniform illumination. *Int. J. Solids Struct.* 48(22-23):3232-3242.
 6. Ohm C, Brehmer M, & Zentel R (2010) Liquid Crystalline Elastomers as Actuators and Sensors. *Adv. Mater.* 22(31):3366-3387.
 7. van Oosten CL, Bastiaansen CWM, & Broer DJ (2009) Printed artificial cilia from liquid-crystal network actuators modularly driven by light. *Nat. Mater.* 8(8):677-682.
 8. Cui J, *et al.* (2012) Bioinspired Actuated Adhesive Patterns of Liquid Crystalline Elastomers. *Adv. Mater.* 24(34):4601-4604.
 9. Liu D, Bastiaansen CWM, den Toonder JMJ, & Broer DJ (2012) Photo-Switchable Surface Topologies in Chiral Nematic Coatings. *Angew. Chem. Int. Ed.* 51(4):892-896.
 10. Urayama K, Honda S, & Takigawa T (2006) Deformation Coupled to Director Rotation in Swollen Nematic Elastomers under Electric Fields. *Macromolecules* 39(5):1943-1949.
 11. Ohm C, Brehmer M, & Zentel R (2010) Liquid Crystalline Elastomers as Actuators and Sensors. *Adv. Mater.* 22(31):3366-3387.
 12. Yu Y & Ikeda T (2006) Soft Actuators Based on Liquid-Crystalline Elastomers. *Angew. Chem. Int. Ed.* 45(33):5416-5418.
 13. White TJ & Broer DJ (2015) Programmable and adaptive mechanics with liquid crystal polymer networks and elastomers. *Nat. Mater.* 14(11):1087-1098.
 14. Ge J, Hu Y, & Yin Y (2007) Highly tunable superparamagnetic colloidal photonic crystals. *Angew. Chem. Int. Ed.* 119(39):7572-7575.
 15. Sato O, Kubo S, & Gu Z-Z (2008) Structural color films with lotus effects, superhydrophilicity, and tunable stop-bands. *Acct. Chem. Res.* 42(1):1-10.
 16. Kim H, *et al.* (2009) Structural colour printing using a magnetically tunable and lithographically fixable photonic crystal. *Nat. Photonics* 3(9):534-540.
 17. Li J, *et al.* (2012) Switching periodic membranes via pattern transformation and shape memory effect. *Soft Matter* 8(40):10322-10328.
 18. Lee E, *et al.* (2014) Tilted Pillars on Wrinkled Elastomers as a Reversibly Tunable Optical Window. *Adv. Mater.* 26(24):4127-4133.
 19. Ge D, *et al.* (2015) A Robust Smart Window: Reversibly Switching from High Transparency to Angle-Independent Structural Color Display. *Adv. Mater.* 27(15):2489-2495.
 20. Glassmaker NJ, Jagota A, Hui C-Y, & Kim J (2004) Design of biomimetic fibrillar interfaces: 1. Making contact. *J. Roy. Soc. Interface* 1(1):23-33.
 21. Lin PC, Vajpayee S, Jagota A, Hui CY, & Yang S (2008) Mechanically tunable dry adhesive from wrinkled elastomers. *Soft Matter* 4(9):1830-1835.
 22. Kamperman M, Kroner E, del Campo A, McMeeking RM, & Arzt E (2010) Functional Adhesive Surfaces with “Gecko” Effect: The Concept of Contact

- Splitting. *Adv. Eng. Mater.* 12(5):335-348.
23. Krupenkin TN, Taylor JA, Schneider TM, & Yang S (2004) From Rolling Ball to Complete Wetting: The Dynamic Tuning of Liquids on Nanostructured Surfaces. *Langmuir* 20(10):3824-3827.
 24. Lin P-C & Yang S (2009) Mechanically switchable wetting on wrinkled elastomers with dual-scale roughness. *Soft Matter* 5(5):1011-1018.
 25. Chen C-M & Yang S (2014) Directed Water Shedding on High-Aspect-Ratio Shape Memory Polymer Micropillar Arrays. *Adv. Mater.* 26(8):1283-1288.
 26. Woltman SJ, Jay GD, & Crawford GP (2007) Liquid-crystal materials find a new order in biomedical applications. *Nat. Mater.* 6(12):929-938.
 27. Yu Y & Ikeda T (2006) Soft Actuators Based on Liquid-Crystalline Elastomers. *Angew. Chem. Int. Ed.* 45(33):5416-5418.
 28. Buguin A, Li M-H, Silberzan P, Ladoux B, & Keller P (2006) Micro-Actuators: When Artificial Muscles Made of Nematic Liquid Crystal Elastomers Meet Soft Lithography. *J. Am. Chem. Soc.* 128(4):1088-1089.
 29. Yang H, *et al.* (2009) Micron-Sized Main-Chain Liquid Crystalline Elastomer Actuators with Ultralarge Amplitude Contractions. *J. Am. Chem. Soc.* 131(41):15000-15004.
 30. Buguin A, Li M-H, Silberzan P, Ladoux B, & Keller P (2006) Micro-Actuators: When Artificial Muscles Made of Nematic Liquid Crystal Elastomers Meet Soft Lithography. *J. Am. Chem. Soc.* 128(4):1088-1089.
 31. Meyer RB (1973) On the existence of even indexed disclinations in nematic liquid crystals. *Phil. Mag.* 27(2):405-424.
 32. Zhang Y, Lo C-W, Taylor JA, & Yang S (2006) Replica Molding of High-Aspect-Ratio Polymeric Nanopillar Arrays with High Fidelity. *Langmuir* 22(20):8595-8601.
 33. Cui J, *et al.* (2012) Bioinspired Actuated Adhesive Patterns of Liquid Crystalline Elastomers. *Adv. Mater.* 24(34):4601-4604.
 34. Cavallaro M, *et al.* (2013) Exploiting imperfections in the bulk to direct assembly of surface colloids. *Proc. Nat. Acad. Sci.* 110(47):18804-18808.
 35. Kleman M & Lavrentovich OD (2003) *Soft Matter Physics: An Introduction* (Springer, New York) p 140.
 36. Wei RB, Zho LY, He YN, Wang XG, & Keller P (2013) Effect of molecular parameters on thermomechanical behavior of side-on nematic liquid crystal elastomers. *Polymer* 54(20):5321-5329.
 37. Gennes P-Gd (1974) *The physics of liquid crystals* (Oxford, Clarendon).
 38. Lee JN, Park C, & Whitesides GM (2003) Solvent compatibility of poly(dimethylsiloxane)-based microfluidic devices. *Anal. Chem.* 75(23):6544-6554.
 39. Ohm C, Haberkorn N, Theato P, & Zentel R (2011) Template-Based Fabrication of Nanometer-Scaled Actuators from Liquid-Crystalline Elastomers. *Small* 7(2):194-198.

CHAPTER 5: Pre-programmed Folding of a 2D Nematic Liquid Crystal Elastomer Sheet into 3D by Directing Liquid Crystal Alignment in 1D Micro-channels

Yu Xia, Gerardo Cedillo, and Shu Yang, manuscript in preparation

5.1 Introduction

Materials that can expand and collapse, fold, and transform into a variety of shapes in response to external stimuli have attracted significant interest for potential applications in flexible electronics,¹⁻³ energy storage devices (*e.g.* batteries⁴ and supercapacitors⁵⁻⁸), optics,^{9, 10} artificial muscles,^{11, 12} actuators,¹³ haptic displays¹⁴⁻¹⁶, smart windows,^{17, 18} soft robotics¹⁹⁻²¹, microfluidics^{22, 23}, and solar harvesting²⁴⁻²⁶. Significant effort has been made to form complex structures through programmable shape change, for example, transforming two-dimensional (2D) sheets into a specific three-dimensional (3D) shape (so called *Origami*) in a variety of responsive soft materials, including hydrogels²⁷⁻³⁰, semicrystalline polymers^{31, 32}, electroactive polymers³³⁻³⁵ and liquid crystalline polymers^{22, 36-38}. An essential aspect of the shape change is actuation at the local regions.

Shape memory polymers (SMPs) are known to be programmable into a temporary shape upon heating above the melting temperature (T_m) or the glass transition temperature (T_g) of the polymer^{39, 40}, which decreases the Young's modulus by 2 – 3 orders of magnitude. When reheated, the temporary shape recovers to the permanent shape. Reheating SMP in the temporary shape above the transition temperature (T_{trans}) triggers the relaxation of the stored elastic energy and the recovery of the permanent

shape. Previously, our group⁴¹⁻⁴⁴ and others^{10, 19, 45-47} have fabricated SMP microstructures for tunable optical and surface properties. Despite the advances and recent demonstrations to achieve multiple temporary shapes,⁴⁸⁻⁵⁰ it remains difficult to achieve reversible shape changing using off-the-shelf SMPs.

Another major challenge in shape change is miniaturization and realization of molecular level anisotropy in material design to locally control shape change and actuation.

Nematic liquid crystal elastomers (NLCEs) that are lightly crosslinked nematic liquid crystalline polymer networks that exhibit spontaneous phase transition or shape change^{51, 52} driven by re-orientation of the local directors of the LC mesogens. It is known that NLCEs exhibit a spontaneous contraction along the director axis and expand perpendicular to the director when heated above their nematic (N) – isotropic (I) phase-transition temperatures (T_{NI}), and the polymer chains attain spherical conformations.⁵³ The phase transition can be triggered by heat, light, and electric field^{51, 52}. Therefore, control of the director field or local alignment of LCs in NLCEs is critical to direct the actuation behavior of LCEs. Monodomain LC alignment has been primarily achieved through mechanical methods^{54, 55}, including mechanical stretching and sheering, and use of magnetic fields^{56, 57}, exhibiting strains of 10%-300%⁵¹. In order to realize more complex and monolithic shape change, control of spatial orientation of LC director profile is necessary, and has been achieved by photoalignment method in a series of 2D liquid crystalline polymer sheets³⁶⁻³⁸. This technique largely relies on a photosensitive molecule consisting of, *e.g.* azobenzene, which orients with the linearly polarized light. To prepare spatially heterogeneous LCEs, a special optical setup is required to control the

local surface alignment of the photoalignment layer from spot to spot. After filling liquid crystal monomers (LCMs) onto the alignment layer in a LC cell, the director of LCMs aligns to the surface orientation of the photoalignment layer. Arbitrary and spatially complex patterns can be generated in LCMs, and the director field profile is transferred into polymer networks after crosslinking. While photoalignment method is an effective and powerful technique to prepare spatially heterogeneous LCEs, it requires special optical setups and the photoaligning process is time-consuming. Therefore, it will be highly desirable to develop a simple, easily accessible, and efficient method that can spatially control LCM orientation to program LCE actuation.

Application of surface topography, such as microgrooves generated by rubbing a polymer layer, to align LCs has been widely used in research and liquid crystal display industry^{51, 58, 59}. The topographical cues in the alignment were first revealed in 1972 by Berreman⁶⁰ who established a theoretical model for the resultant elastic distortion energy of LC on the one-dimensional (1D) grooves. Berreman's work has been a benchmark for the researches of LC alignment by geometrical patterns. More sophisticated LC alignment patterns with arbitrary rubbing directions were later demonstrated by scratching using an AFM tip,⁶¹ a more elegant rubbing technique. Through this method, a tri-stable LC device was prepared⁶¹. However, rubbing method often suffers from the disadvantages such as generation of dusts, scratches, and creation of static charges on the aligning surface. Here, we fabricate 1D channels using photolithography and replicate to epoxy substrate by soft-lithography to prepare charge-free and planar anchored surfaces to precisely control the LCM alignment (Figure 5.1a&c). We show that LCMs can be aligned faithfully within the patterned 1D micro-channels with exceptional spatial

resolution, leading to the formation of a variety of 3D structures predicted by theory^{62, 63}.

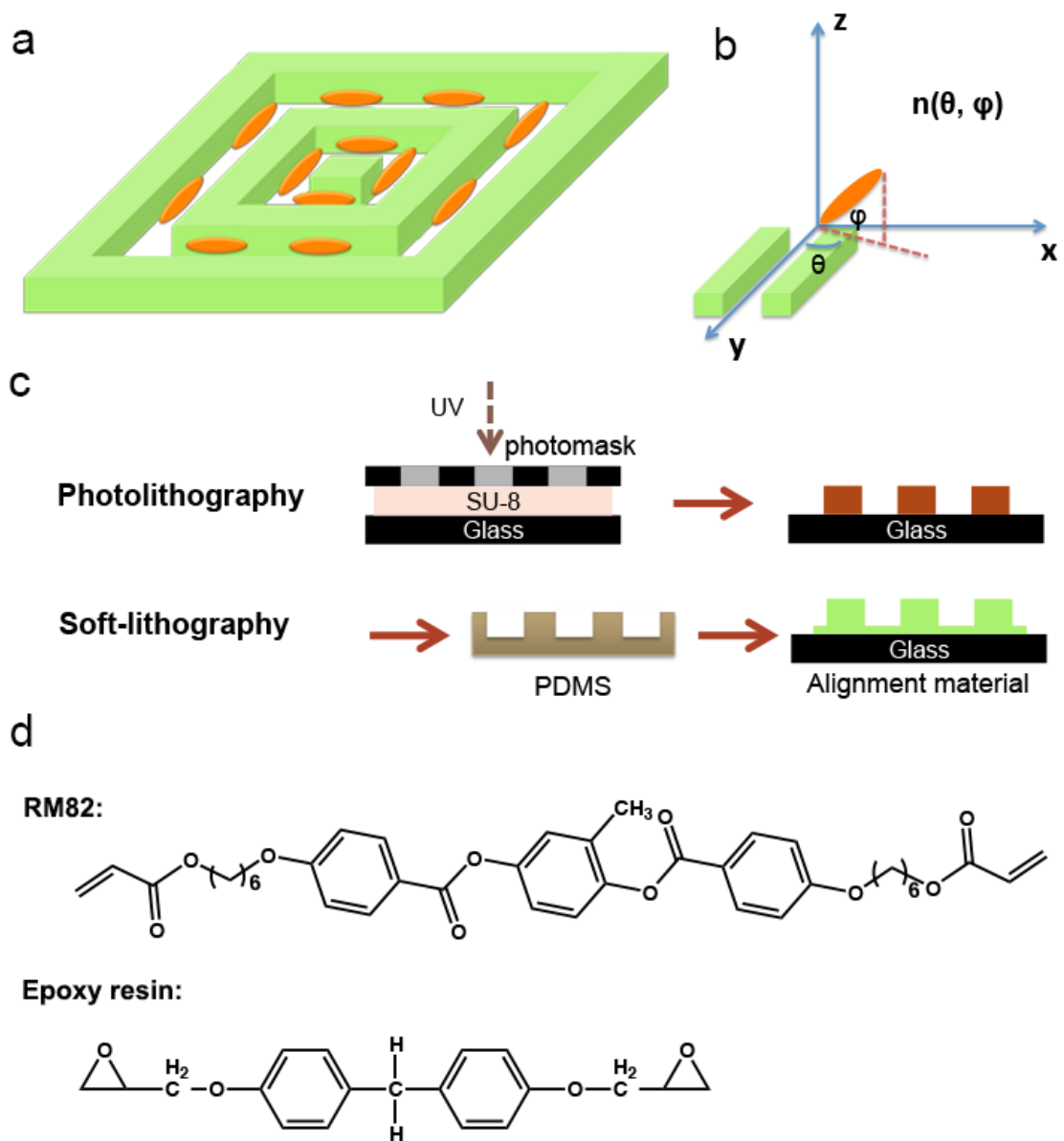


Figure 5.1 Design of the 1D channels for LCM alignment. (a) Illustration of LCMs oriented in patterned 1D channels, where LC molecule follows the local orientation of the channel; (b) Representation of a LC molecule within the 1D channel in a Cartesian coordinate. Channel direction is along y-axis; (c) Schematic of the 1D channel fabrication process. A pattern master is first fabricated by photolithography, and then replicated twice to PDMS and epoxy resin (D.E.R. 354), respectively, by soft lithography. (d) Chemical structures of RM82 and epoxy resin (D.E.R. 354).

5.2 Experimental methods

5.2.1 Materials

N,N-dimethyl-n-octadecyl-3-amino-propyltrimethoxysilyl chloride (DMOAP), propylene glycol monomethyl ether acetate (PGMEA), n-butylamine, and photoinitiator 2,2-dimethoxy-2-phenylacetophenone (DMPA) were purchased from Sigma Aldrich and used as received. 4-Cyano-4'-pentylbiphenyl (5CB) was purchased from Kingston Chemicals Limited. Hydrochloric acid (HCl) was purchased from Fisher Scientific. Negative-tone photoresist SU8-2 was purchased from MicroChem Corporation and epoxy resin D.E.R. 354 was purchased from DOW chemical. Poly(dimethylsiloxane) (PDMS) resin and curing agent were purchased from DOW Corning. Liquid crystal monomer, 1,4-bis-[4-(6-acryloyloxy-hexyloxy)benzoyloxy]-2-methylbenzene (RM82), was purchased from Wilshire technologies and used without further purification.

5.2.2 Characterization

Liquid crystal alignment was characterized by a motorized optical microscope (Olympus BX61) with crossed polarizers using CellSens software. For thermal anneal and actuation, samples were heated on a Mettler FP82 and FP90 thermo-system hot stage in ambient air. SEM imaging was performed on a dual beam FEI Strata DB 235 Focused Ion Beam (FIB)/ SEM instrument with 5KV electron-beam.

5.2.3 Fabrication of 1D channel masters

The 1D channels were fabricated from photoresist SU8 using conventional photolithography. Glass substrates were pre-cleaned by washing with acetone three times, followed by drying with an air gun. A thin layer of SU8-2 was spin-coated (2000 rpm for 40s) on a glass substrate with thickness $\sim 1.5 \mu\text{m}$, followed by prebaking at 95°C for 1

min. The SU8 layer was then exposed to 365nm UV light (Newport model 97436-1000-1, Hg source) through a photomask with a dosage of 200 mJ/cm². After post-baking on 95°C for 1 min, the sample was developed by PGMEA to wash away the uncured SU8, and obtain the final SU8 pattern.

5.2.4 Replica molding of epoxy alignment patterns

First, the PDMS mold was replicated from the above fabricated SU8 master, following the protocol reported earlier⁶⁴. To create a planar anchoring 1D channels to align LCMs, the PDMS mold was replicated to epoxy (D.E.R. 354).

5.2.5 Preparation of DMOAP coated glass substrates.

3 vol% DMOAP solution was prepared in a mixture of water/ethanol (1:9 v/v). The glass slides were immersed into the solution for 30 min, followed by rinsing with deionized (DI) water three times and baking at 110 °C in a convection oven for 1 h.

5.2.6 Preparation of liquid crystal cells

Liquid crystal cells were constructed by composing one surface with the patterned epoxy and the other one either from the patterned epoxy or non-patterned (flat) glass. For the alignment tests shown in Figure 5.3, the non-patterned glass substrates were treated with DMOAP to introduce homeotropic anchoring for 5CB or no treatment for RM82. So the alignment patterns of LCs shown in Figure 5.3 were entirely guided by the patterned epoxy surface, since the non-patterned regions are homeotropic for both LCs. In the preparation of the 2D NLCE sheet, patterned epoxy substrates were used for both top and bottom surfaces in the LC cells, which were aligned under an optical microscope with mismatch within 10 μm. The top and bottom channels were designed to be either parallel for the uniform cells or perpendicular for the twist cells. The thickness of the LC cells

was controlled using a Mylar spacers $\sim 150 \mu\text{m}$.

5.2.7 Preparation of NLCE sheets

Following the literature³⁶, NLCE sheets from RM82 were prepared in two steps. First, 150 mg RM82 was mixed together with 16 mg n-butylamine (molar ratio=1.02:1) and 2 mg DMPA in a sealed glass vial. The powder mixture was then heated at $95 \text{ }^\circ\text{C}$ to be fully melted under stirring. The liquid was substantially infiltrated into the LC cells prepared in Section 5.2.6 on a hot stage at $80 \text{ }^\circ\text{C}$ and kept overnight to form oligomers. In the second step, the oligomers of RM82 was slowly cooled down to room temperature under ambient condition, and photocrosslinked using a 365nm UV lamp (Thorlabs-CS2010) with a strong light power $\sim 65 \text{ mW/cm}^2$ for 5 min at both front and back, respectively. After crosslinking, the NLCE cell was opened by a razor blade, and the epoxy alignment layers were carefully peeled to obtain a freestanding LCE sheet.

5.2.8 Characterization of the NLCE sheets

LC alignment in the NLCE sheet was characterized under POM with either parallel or crossed polarizers. Actuation of the LCE sheet was studied by heating to 200°C and cooling the sample in ambient air on a hot stage reversibly.

5.3 Fabrication of patterned 1D channels

The advancement of top-down lithographic techniques make them accessible to fabricate 1D channels with precise control of size and geometry at various lengthscales and in a wide range of materials. To align LCs on 1D channels uniformly over the entire sample ($\sim 2\text{cm}^2$), it is critical to maximize the LC surface anchoring strength, which

depends on the surface chemistry of the aligning material and the dimensions of the channels. As illustrated in Figure 5.1b, a LC molecule sits in a Cartesian coordinates with LC director \mathbf{n} represented by the azimuthal angle θ and zenithal angle ϕ . To achieve faithful control of LC alignment, ϕ and θ need to be minimized by carefully selecting the surface chemistry of the alignment material and constructing the topography of the channel, respectively. As a proof-of-concept of our surface alignment channels, we chose 1,4-bis-[4-(6-acryloyloxy-hexyloxy)benzoyloxy]-2-methylbenzene (RM82) as LCM, which was recently demonstrated for folding based on photoalignment technique³⁶. Accordingly, we chose a commercial epoxy resin based on bisphenol F (D.E.R. 354) to prepare alignment 1D channels (Figure 5.1c-d). D.E.R. 354 is cheap and widely used in replica molding. More importantly, bisphenol F consists of conjugated benzyl rings like RM82, thus D.E.R. 354 can strongly bond with RM82 through π - π interaction, leading to planar anchoring of RM82, and in turn minimizing the zenithal angle ϕ . Similar mechanism has been reported in the alignment of columnar phase on the substrate coated with a thin layer of graphene and polystyrene⁶⁵. To minimize azimuthal angle θ , it requires a more detailed description of anchoring energy of LCs on the 1D channels. According to Berreman's model, the maximum free energy density for LC aligning perpendicular to the channel direction, or the surface anchoring energy is expressed as⁶⁰

$$\rho_{max} = \frac{\pi^2 K A^2}{\lambda^3} \quad (5-1)$$

where K is the average elastic constant of LC, A and λ are the amplitude and wavelength

of the surface topography, respectively. Apparently, to minimize alignment angle θ , it is preferably to have deeper and narrower channels. Here, we designed and fabricated 1D channels with variable width and depth to fine-tune the anchoring strength as well as different layout to generate various topological defects in LC anchoring, including “+1” defects in Figure 5.2a-b, “-1” (Figure 5.2c) and “+1/2” (Figure 5.2d).

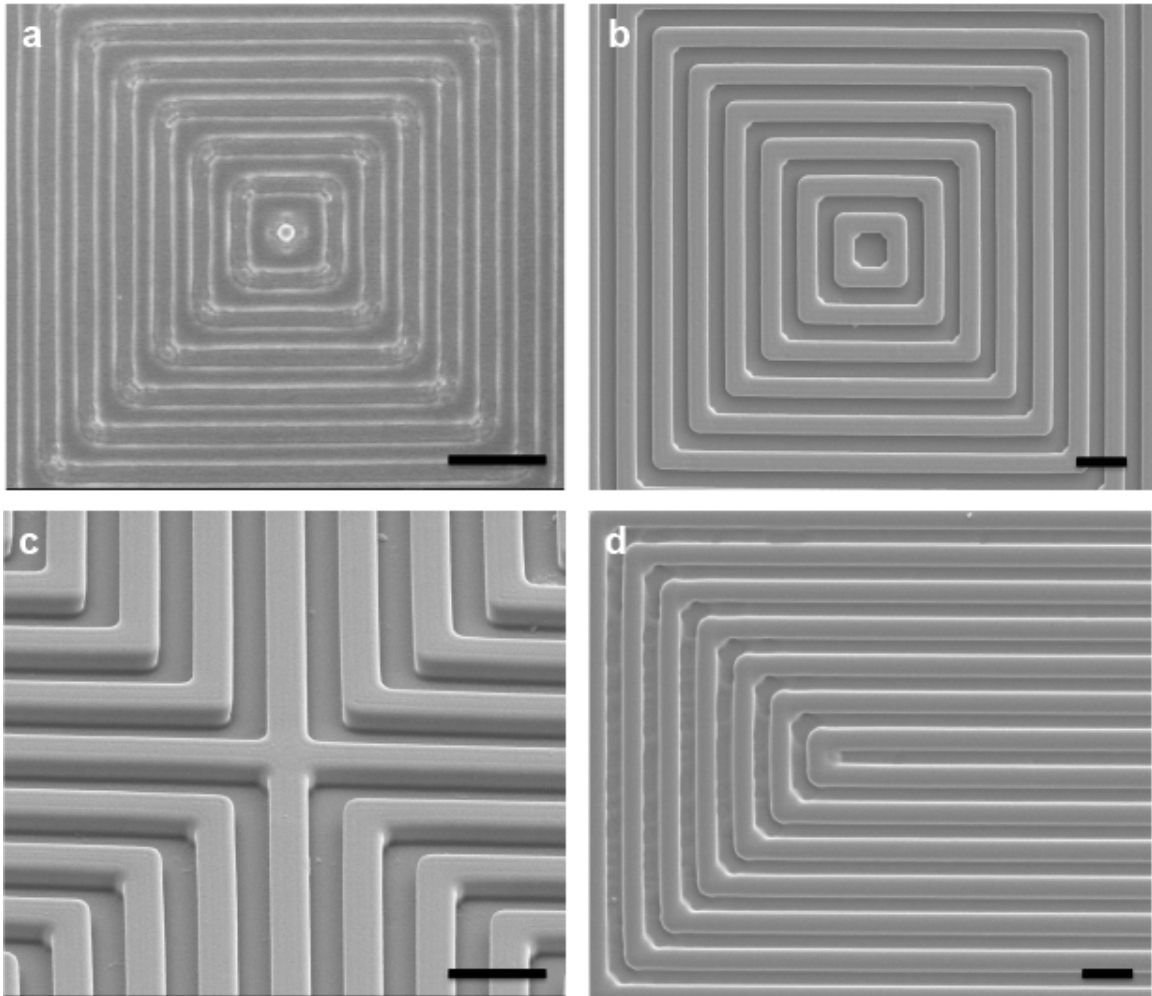


Figure 5.2 SEM images of the different patterned 1D channels with the same depth of 1.5 μm . (a-b) “+1” defect structures from different channel width: (a) 1 μm and (b) 2 μm . (c) Channels with 2 μm channel width with a “-1” defect. Image is tilted at 45°. (d) Channels with 2 μm feature width with a “+1/2” defect. Scale bars: 5 μm .

Using photolithography at 365 nm through a photomask, we prepared line patterns with feature size of 1 μm and 2 μm , respectively, and the same depth of 1.5 μm as shown in Figure 5.2. According to Eq. (5-1), pattern with smaller feature size will better align the LCs. However, decreasing the feature size also sacrifices the pattern resolution unless we use 248 nm and 193 nm DUV lithography⁶⁶, which increases the fabrication complexity and cost. As shown in Figure 5.2a, there are numerous fabrication defects appeared at the corners of each squares consisting of 1 μm 1D channels, indicating 1 μm feature size is approaching the fabrication limit of the 365nm UV lamp. When we prepared 2 μm patterns, as seen in Figure 5.2b no apparent defects were observed, which is essential to achieve faithful anchoring control of LCM alignment. In a similar manner, we fabricated 1D channels with 2 μm width in a variety of geometries (Figure 5.2c-d) to investigate the capability to control LCM alignment and program NLCE sheet folding. Channel depth, another important factor that affects LCM alignment, was kept the same as 1.5 μm for all samples in this study. In principal, deeper channels can offer stronger alignment. However surface corrugations from the patterns may as well affect the actuation behavior of NLCEs due to the surface geometrical constrain. Such effect becomes more significant with increasing channel depth. We found channels with 1.5 μm depth were sufficient to orient LCMs in our study (Figure 5.3) yet small enough comparing to the sample thickness ($\sim 150 \mu\text{m}$), thus has negligible effect on the NLCE actuation.

5.4 LC anchoring study

LC alignment on the patterned 1D channels was verified by polarized optical microscopy (POM), as shown in Figure 5.3. First, we demonstrated the effect using small molecule NLC, 4-cyan-4'-penylbiphenyl (5CB), which also possesses planar anchoring on epoxy, on a pattern with “+1” and “-1” defect arrays and the other with “+½” and “-½” defect arrays. 5CB is strongly aligned by both patterns, as one can clearly see the topological defects under POM (Figure 5.3a-b). Similarly, RM82 aligned well by the patterns (Figure 5c-d) with topological defects same as seen in 5CB with uniform director pattern across the entire sample. Moreover, the sharp features of LC alignment at the corners of the square/rectangular patterns indicate the orientation of LC molecules on the patterned surface is “local” with submicron resolution, comparable to that using a photoalignment layer³⁶. However, our alignment system is much simpler, low cost, and more importantly, any arbitrary 2D structures can be generated without concern of light intensity distribution from the center to the edge of the light beam, which limits the unit area (or pixel size) using photoalignment method. In our system, LCM is oriented more “locally” within a length scale around several micrometers, whereas a typical pixel size is ~100 μm using photoalignment, indicating that our method is more effective in aligning LCMs. As the result, our method is capable to create up to millions of topological defects in one setting. The miniaturization of the topological patterns can thus be easily achieved in our system.

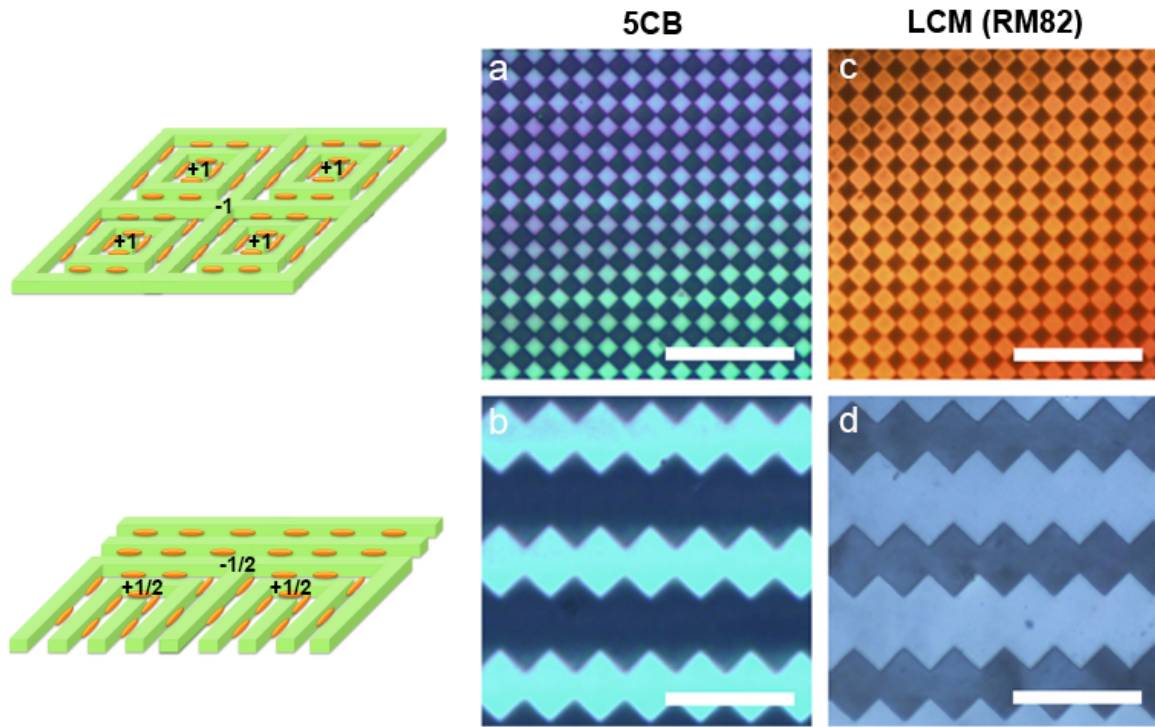


Figure 5.3 POM images of LC alignment on patterned 1D channels. Left panels: schematics of LCs aligning in different patterns with topological defects marked. Right panels: POM images of (a-b) 5CB and (c-d) RM82 on the corresponding patterned surfaces. Scale bars: (a,c), 200 μm , (b,d), 25 μm .

5.5 Folding of NLCE 2D Sheets

With faithful anchoring control of LCMs within the patterned 1D channels, LCEs were prepared by photo-crosslinking within a LC cell, either twisted or uniform, constructed with top and bottom surfaces with 1D channels of different channel orientations. As demonstrated in Figure 5.4a, a twisted cell is prepared by aligning the top and bottom channels perpendicular with each other, which is verified by POM images shown in Figure 5.4b-c. The LCE film appeared dark between parallel polarizers (b) and bright with crossed polarizers (c), indicating the transmitted light has been rotated 90° across the LC film, and so was the LC director. The folding behavior of the NLCE film

with twisted LC director profile has been predicted by theory that a saddle-like negative Gaussian curvature can be generated with a strain $\epsilon < 100\%$ ⁶⁷. In our system, the strain of the NLCE film is $\sim 55\%$, therefore the film buckles into 3D. As shown in Figure 5.4e, an array of convex “cones” is observed in the NLCE film with embedded “+1” and “-1” LC topological defects when heating at 200 °C. In those cones, the apex of the cone is formed by the “+1” defect in the NLCE film with least contraction, while “-1” defect gives the base of each cone, which contract most and push the sheet up. This shape transformation agrees well with the theoretical prediction⁶² and it is also consistent with the literature reports from the same NLCE systems³⁶. We note that since our sheet has a much higher density of LC defects compared to those obtained by photoalignment, our photopatterning approach can afford much more complex shape transformation and load sharing.

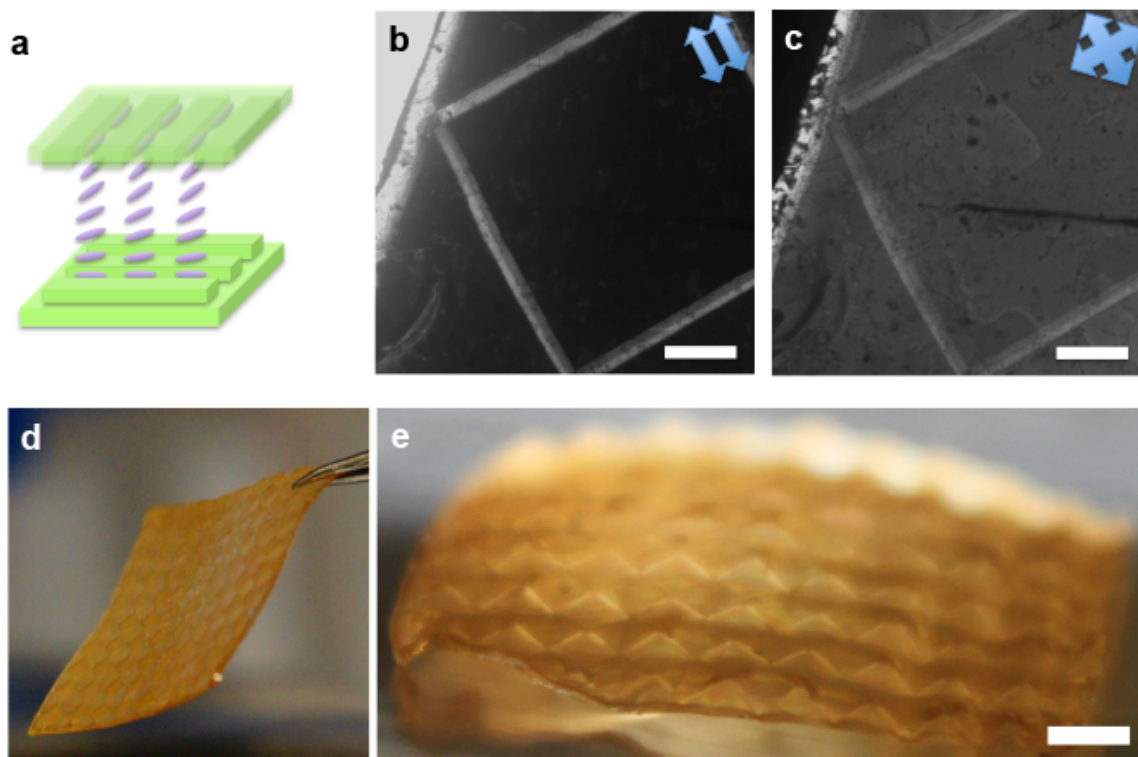


Figure 5.4 Actuation of the NLCE film with “+1” and “-1” defect array. (a) Schematic of LC orientation in the LC cell. LC director is twisted by 90° from bottom to top. (b-c) POM images of the LCE film with parallel (b) and cross (c) polarizers indicated by the arrows in the up right corner. (d-e) Optical images of the NLCE films at (d) room temperature and (e) 200 °C. Scale bars: (b-c) 100 μm , (e) 1 mm.

Buckling of 2D NLCE film into 3D structures can also be realized in a uniform LC cell as demonstrated in Figure 5.5. Locally uniform LC director field is obtained by aligning the top and bottom channels parallel to each other, thus avoiding LC elastic distortion. In this case, “+ $\frac{1}{2}$ ” and “- $\frac{1}{2}$ ” topological defects are incorporated into the LC director pattern for the study of LCE actuation with a complex director profile design. It is predicted by theoretically modeling⁶³, when actuated, the “+ $\frac{1}{2}$ ” defects buckle up to form the ridges of the wrinkle and the “- $\frac{1}{2}$ ” defects curls down to form the grooves. In our system, the NLCE sheet with “+ $\frac{1}{2}$ ” and “- $\frac{1}{2}$ ” LC defect arrays transforms into a

curling wrinkled film (see Figure 5.4c), exactly as predicted by theory. The number of the wrinkles shown in Figure 5.4c matches perfectly with that of the patterned LC director field shown in Figure 5.4b, further confirming that the wrinkling formation of the NLCE sheet is programmed by the complex LC director profile when heated above T_{NI} . An extra degree of freedom of bending has also been suggested by theoretical modeling⁶³ that the film curls perpendicular to the direction of the ridge and groove, which again is in complete agreement with our observation in experiments. Therefore, the study presented here clearly shows that 1D micro-channels patterned by top-down techniques are simple yet versatile to align LCM and can preprogram NLCE folding precisely as theory predication.

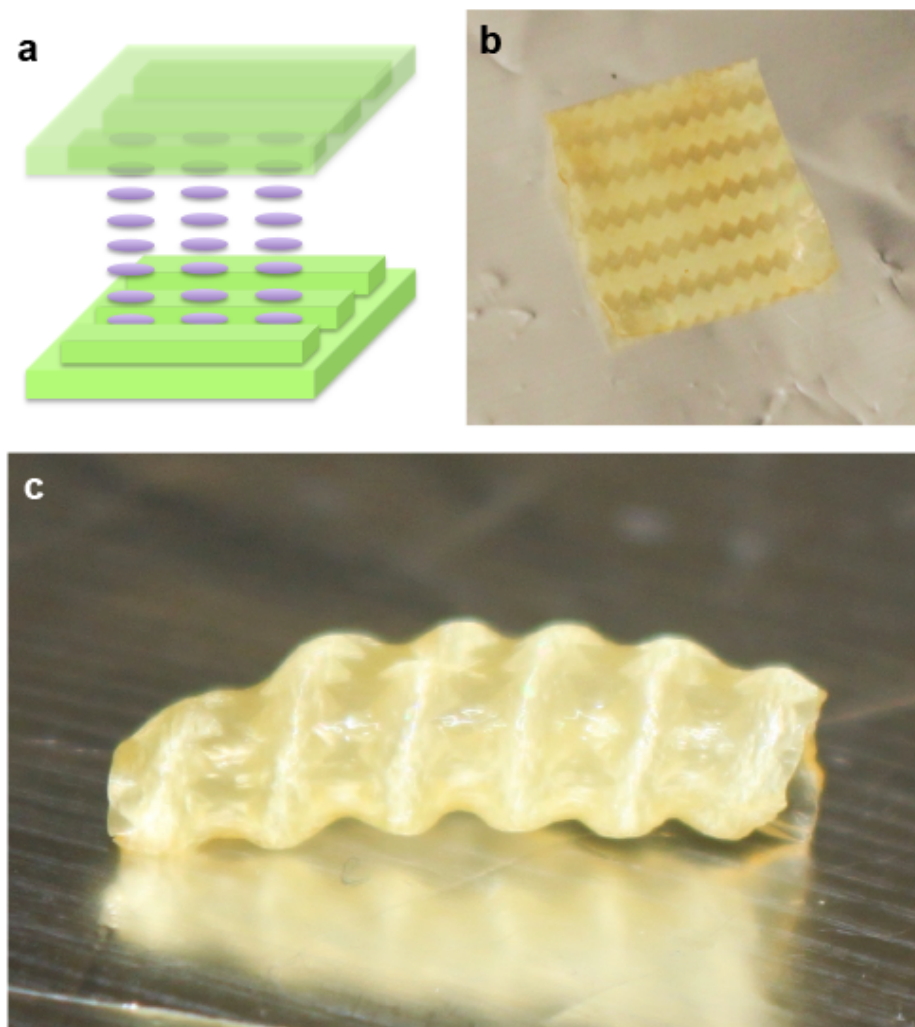


Figure 5.5 Actuation of NLCE sheet with “+ $\frac{1}{2}$ ” and “- $\frac{1}{2}$ ” defect array. (a) Schematic of LC orientation in the LC cell. LC director is parallel from bottom to top. (b-c) Optical images of the NLCE films at (b) room temperature and (c) 200 °C.

5.6 Conclusions

We demonstrate a new method to faithfully align small molecule LCs and LCMs within the patterned epoxy micro-channels with 2 μm channel width and 1.5 μm channel depth. Both channel width and depth together with surface chemistry are critical to tune the anchoring strength of LC alignment on the channel. We investigated both

experimentally and by energy calculation. Guided by theoretical modeling, we patterned complex LC director profiles with different types of topological defects in NLCE sheets by design of different surface patterns in epoxy alignment layers. Upon heating above T_{NI} , the NLCE sheet with embedded “+1” and “-1” defects folded into an array of cones in a large area ($\sim 4\text{cm}^2$), and the one with “+1/2” and “-1/2” defects formed curling 3D wrinkles. The observed shape transformations from both examples are in complete agreement with theoretical predictions, which unequivocally validate the applicability and universality of our approach.

Since the pattern’s feature size and arrangement can be sculpted arbitrarily by lithographic techniques in sub-micron scale, we will work with theoretical physics groups to design topological defect arrays to preprogram the folding at even finer scales and control the actuation magnitude. Currently, the 2D sheet can fold up or down with little energy cost between two states. To further control the magnitude and directionality of the strain, local crosslinking gradient in-plane and out-of-plane will be introduced through a photomask or use light absorbing azobenzene dyes.

Since the level of the internal strain of NLC is also critical to realize the folding structures, we will build upon our understandings in LC mesogen designs shown in Chapter 3 and synthesize new LCMs that meet the requirements for NLCE actuation, including: 1) stable nematic phases to achieve strong anchoring; 2) fast polymerization to maintain the director field; 3) relatively low T_g to obtain fully crosslinked network; 4) relatively low crosslinking density for detectable T_{NI} ; and 5) a suitable nematic window for polymerization. In particular, we will design LCMs that can be photopolymerized by thio-ene “click” chemistry⁶⁸, which is fast and less sensitive to the environmental oxygen

and to side chain functionality of the mesogens.

5.7 Contributions

Y.X. and S.Y. conceived and designed the experiments. Y.X. and G.C. performed the experiments. S.Y. supervised the work. Y.X. and S.Y. wrote the paper.

5.8 References

1. Sekitani T & Someya T (2012) Stretchable organic integrated circuits for large-area electronic skin surfaces. *MRS Bull.* 37(03):236-245.
2. Suo Z (2012) Mechanics of stretchable electronics and soft machines. *MRS Bull.* 37(03):218-225.
3. Kim DH, *et al.* (2011) Epidermal Electronics. *Science* 333(6044):838-843.
4. Xu S, *et al.* (2013) Stretchable batteries with self-similar serpentine interconnects and integrated wireless recharging systems. *Nat. Commun.* 4:8.
5. Weng Z, *et al.* (2011) Graphene–Cellulose Paper Flexible Supercapacitors. *Adv. Energy Mater.* 1(5):917-922.
6. Zheng GY, Hu LB, Wu H, Xie X, & Cui Y (2011) Paper supercapacitors by a solvent-free drawing method. *Energ. Environ. Sci.* 4(9):3368-3373.
7. Jost K, *et al.* (2011) Carbon coated textiles for flexible energy storage. *Energy Environ. Sci.* 4(12):5060-5067.
8. Ge D, *et al.* (2015) Foldable supercapacitors from triple networks of macroporous cellulose fibers, single-walled carbon nanotubes and polyaniline nanoribbons. *Nano Energy* 11:568-578.
9. Song YM, *et al.* (2013) Digital cameras with designs inspired by the arthropod eye. *Nature* 497(7447):95-99.
10. Xu HX, *et al.* (2013) Deformable, Programmable, and Shape-Memorizing Micro-Optics. *Adv. Funct. Mater.* 23(26):3299-3306.
11. Baughman RH (1996) Conducting polymer artificial muscles. *Synthetic Metals* 78(3):339-353.
12. Jager EWH, Smela E, & Inganäs O (2000) Microfabricating conjugated polymer actuators. *Science* 290(5496):1540-1545.
13. Keplinger C, *et al.* (2013) Stretchable, Transparent, Ionic Conductors. *Science* 341(6149):984-987.
14. Camargo CJ, *et al.* (2012) Batch fabrication of optical actuators using nanotube–elastomer composites towards refreshable Braille displays. *J. Micromech. Microeng.* 22(7):075009.

15. Torras N, *et al.* (2014) Tactile device based on opto-mechanical actuation of liquid crystal elastomers. *Sensors Actuators A: Phys.* 208:104-112.
16. Liu D & Broer DJ (2014) Self-assembled Dynamic 3D Fingerprints in Liquid-Crystal Coatings Towards Controllable Friction and Adhesion. *Angew. Chem.* 126(18):4630-4634.
17. Lee E, *et al.* (2014) Tilted Pillars on Wrinkled Elastomers as a Reversibly Tunable Optical Window. *Adv. Mater.* 26(24):4127-4133.
18. Ge D, *et al.* (2015) A Robust Smart Window: Reversibly Switching from High Transparency to Angle-Independent Structural Color Display. *Adv. Mater.* 27(15):2489-2495.
19. Liu C, Qin H, & Mather PT (2007) Review of progress in shape-memory polymers. *J. Mater. Chem.* 17(16):1543-1558.
20. de Haan LT, Schenning APHJ, & Broer DJ (2014) Programmed morphing of liquid crystal networks. *Polymer* 55(23):5885-5896.
21. De Gennes P-G, Hébert M, & Kant R (1997) Artificial muscles based on nematic gels. *Macromol. Symp.* 113(1):39-49.
22. Chen M, *et al.* (2011) Photodeformable CLCP material: study on photo-activated microvalve applications. *Appl. Phys. A* 102(3):667-672.
23. van Oosten CL, Bastiaansen CWM, & Broer DJ (2009) Printed artificial cilia from liquid-crystal network actuators modularly driven by light. *Nat. Mater.* 8(8):677-682.
24. Hiscock T, Warner M, & Palffy-Muhoray P (2011) Solar to electrical conversion via liquid crystal elastomers. *J. Appl. Phys.* 109(10):104506.
25. Li C, Liu Y, Huang X, & Jiang H (2012) Direct Sun-Driven Artificial Heliotropism for Solar Energy Harvesting Based on a Photo-Thermomechanical Liquid-Crystal Elastomer Nanocomposite. *Adv. Funct. Mater.* 22(24):5166-5174.
26. Yin R, *et al.* (2009) Can sunlight drive the photoinduced bending of polymer films? *J. Mater. Chem.* 19(20):3141-3143.
27. Zhou Y, *et al.* (2012) Hierarchically Structured Free-Standing Hydrogels with Liquid Crystalline Domains and Magnetic Nanoparticles as Dual Physical Cross-Linkers. *J. Am. Chem. Soc.* 134(3):1630-1641.
28. Liu D, Bastiaansen CWM, den Toonder JMJ, & Broer DJ (2013) (Photo-)Thermally Induced Formation of Dynamic Surface Topographies in Polymer Hydrogel Networks. *Langmuir* 29(18):5622-5629.
29. Palleau E, Morales D, Dickey MD, & Velev OD (2013) Reversible patterning and actuation of hydrogels by electrically assisted ionoprinting. *Nat. Commun.* 4:2257.
30. Kim J, Hanna JA, Byun M, Santangelo CD, & Hayward RC (2012) Designing Responsive Buckled Surfaces by Halftone Gel Lithography. *Science (New York, N.Y.)* 335(6073):1201-1205.
31. Behl M, Kratz K, Noechel U, Sauter T, & Lendlein A (2013) Temperature-memory polymer actuators. *Proc. Natl. Acad. Sci.* 110(31):12555-12559.
32. Pandini S, *et al.* (2015) The two-way shape memory behaviour of crosslinked poly(ϵ -caprolactone) systems with largely varied network density. *J. Intell. Mater. Syst. Struct.*
33. Li J, *et al.* (2011) Superfast-Response and Ultrahigh-Power-Density

- Electromechanical Actuators Based on Hierarchical Carbon Nanotube Electrodes and Chitosan. *Nano Lett.* 11(11):4636-4641.
34. Li Q, *et al.* (2015) Large-Strain, Multiform Movements from Designable Electrothermal Actuators Based on Large Highly Anisotropic Carbon Nanotube Sheets. *ACS Nano* 9(1):409-418.
 35. Kong L & Chen W (2014) Carbon Nanotube and Graphene-based Bioinspired Electrochemical Actuators. *Adv. Mater.* 26(7):1025-1043.
 36. Ware TH, McConney ME, Wie JJ, Tondiglia VP, & White TJ (2015) Voxellated liquid crystal elastomers. *Science (New York, N.Y.)* 347(6225):982-984.
 37. McConney ME, *et al.* (2013) Topography from Topology: Photoinduced Surface Features Generated in Liquid Crystal Polymer Networks. *Adv. Mater.* 25(41):5880-5885.
 38. de Haan LT, Sánchez-Somolinos C, Bastiaansen CMW, Schenning APHJ, & Broer DJ (2012) Engineering of Complex Order and the Macroscopic Deformation of Liquid Crystal Polymer Networks. *Angew. Chem.* 124(50):12637-12640.
 39. Lendlein A & Kelch S (2002) Shape-Memory Polymers. *Angew. Chem. Int. Ed.* 41(12):2034-2057.
 40. Mather PT, Luo XF, & Rousseau IA (2009) Shape Memory Polymer Research. *Ann. Rev. Mater. Res.* 39:445-471.
 41. Li J, *et al.* (2012) Switching periodic membranes via pattern transformation and shape memory effect. *Soft Matter* 8(40):10322-10328.
 42. Chen C-M, Chiang C-L, Lai C-L, Xie T, & Yang S (2013) Buckling-Based Strong Dry Adhesives Via Interlocking. *Adv. Funct. Mater.* 23(30):3813-3823.
 43. Chen C-M & Yang S (2014) Directed Water Shedding on High-Aspect-Ratio Shape Memory Polymer Micropillar Arrays. *Adv. Mater.* 26(8):1283-1288.
 44. Zheng Y, Li J, Lee E, & Yang S (2015) Light-induced shape recovery of deformed shape memory polymer micropillar arrays with gold nanorods. *RSC Adv.* 5(39):30495-30499.
 45. Patrick TM, Xiaofan L, & Ingrid AR (2009) Shape Memory Polymer Research. *Annu. Rev. Mater. Res.* 39(1):445-471.
 46. Lendlein A & Kelch S (2002) Shape-Memory Polymers. *Angew. Chem. Int. Ed.* 41(12):2034-2057.
 47. Yu Z, *et al.* (2011) Highly Flexible Silver Nanowire Electrodes for Shape-Memory Polymer Light-Emitting Diodes. *Adv. Mater.* 23(5):664-668.
 48. Xie T (2010) Tunable polymer multi-shape memory effect. *Nature* 464(7286):267-270.
 49. Bellin I, Kelch S, Langer R, & Lendlein A (2006) Polymeric triple-shape materials. *Proc. Nat. Acad. Sci. U. S. A.* 103(48):18043-18047.
 50. Xie T, Xiao X, & Cheng YT (2009) Revealing Triple - Shape Memory Effect by Polymer Bilayers. *Macromol. Rap. Comm.* 30(21):1823-1827.
 51. Ohm C, Brehmer M, & Zentel R (2010) Liquid Crystalline Elastomers as Actuators and Sensors. *Adv. Mater.* 22(31):3366-3387.
 52. Warner M & Terentjev EM (2003) *Liquid crystal elastomers* (Clarendon Press, Oxford).

53. Jin LH, Lin Y, & Huo YZ (2011) A large deflection light-induced bending model for liquid crystal elastomers under uniform or non-uniform illumination. *Int. J. Solids Struct.* 48(22-23):3232-3242.
54. Küpfer J & Finkelmann H (1991) Nematic liquid single crystal elastomers. *Makromol. Chem. Rapid. Commun.* 12(12):717-726.
55. Ohm C, Fleischmann E-K, Kraus I, Serra C, & Zentel R (2010) Control of the Properties of Micrometer-Sized Actuators from Liquid Crystalline Elastomers Prepared in a Microfluidic Setup. *Adv. Funct. Mater.* 20(24):4314-4322.
56. Buguin A, Li M-H, Silberzan P, Ladoux B, & Keller P (2006) Micro-Actuators: When Artificial Muscles Made of Nematic Liquid Crystal Elastomers Meet Soft Lithography. *J. Am. Chem. Soc.* 128(4):1088-1089.
57. Yang H, *et al.* (2009) Micron-Sized Main-Chain Liquid Crystalline Elastomer Actuators with Ultralarge Amplitude Contractions. *J. Am. Chem. Soc.* 131(41):15000-15004.
58. Yu Y & Ikeda T (2006) Soft Actuators Based on Liquid-Crystalline Elastomers. *Angew. Chem. Int. Ed.* 45(33):5416-5418.
59. Abbott NL (1997) Surface effects on orientation of liquid crystals. *Curr. Opin. Colloid Interface Sci.* 2(1):76-82.
60. Berreman DW (1972) Solid Surface Shape and the Alignment of an Adjacent Nematic Liquid Crystal. *Phys. Rev. Lett.* 28(26):1683-1686.
61. Kim J-H, Yoneya M, & Yokoyama H (2002) Tristable nematic liquid-crystal device using micropatterned surface alignment. *Nature* 420(6912):159-162.
62. Modes CD & Warner M (2011) Blueprinting nematic glass: Systematically constructing and combining active points of curvature for emergent morphology. *Phys. Rev. E* 84(2):021711.
63. Modes CD & Warner M (2012) The activated morphology of grain boundaries in nematic solid sheets. *Proc. SPIE*, pp 82790Q82791-82798.
64. Zhang Y, Lo C-W, Taylor JA, & Yang S (2006) Replica Molding of High-Aspect-Ratio Polymeric Nanopillar Arrays with High Fidelity. *Langmuir* 22(20):8595-8601.
65. Jeong J, *et al.* (2014) Homeotropic Alignment of Lyotropic Chromonic Liquid Crystals Using Noncovalent Interactions. *Langmuir* 30(10):2914-2920.
66. Choi JO, Moore JA, Corelli JC, Silverman JP, & Bakhru H (1988) Degradation of poly(methylmethacrylate) by deep ultraviolet, x - ray, electron beam, and proton beam irradiations. *J. Vac. Sci. Technol. B* 6(6):2286-2289.
67. Warner M, Modes CD, & Corbett D (2010) Curvature in nematic elastica responding to light and heat. *Proc. R. Soc. London, Ser. A* 466(2122):2975-2989.
68. Xi W, Scott TF, Kloxin CJ, & Bowman CN (2014) Click Chemistry in Materials Science. *Adv. Funct. Mater.* 24(18):2572-2590.

CHAPTER 6: Alignment of Nematic Liquid Crystals on Chemically Patterned Surfaces: Precise Design of Topological Defects

Yu Xia, Hye-Na Kim, Gaoxiang Wu, Sachin Deshpande, and Shu Yang, manuscript in preparation

6.1 Introduction

Structural heterogeneity and imperfections within a material have profound impact to the material thermodynamics¹⁻⁴, mechanical^{1, 5}, electrical and optical properties^{2, 6}. Liquid crystals (LCs), the nanomaterials with anisotropic thermal, optical, electrical, and magnetic properties have offered many beautiful examples of spontaneous assembly of micro- and nano-objects at surface and interface⁷⁻⁹. Although preparation of defect-free LC alignment is vital in liquid crystal displays (LCDs), topological defects in LCs (or singularities) and their patterning have attracted great interests to pre-program responsiveness in liquid crystal elastomers (LCEs)¹⁰⁻¹², to promote bistability in LC optical devices¹³⁻¹⁵, and to direct assembly of micron-sized colloids^{16, 17} nanoparticles¹⁸⁻²¹ and amphiphiles²². The process of (dis)assembly to the topological defects can be triggered and precisely directed. The balance of the orientational elasticity and surface anchoring of the surrounding liquid crystals has led to a dynamic and robust process, where topological defects can be reversibly assembled and disassembled depending on the local LC orientation – the director surrounding the topological defects.

Topological defects in nematic liquid crystals (NLCs) can exist in various forms from points to lines. By imposing topology, topography, and surface chemistry at interfaces, it is possible to precisely control the defect structures, and in turn the guided

assembly/disassembly. Topological and topographical effects of boundary conditions on LC alignment and defect formation have been studied in a variety of settings, including micron-sized colloids with various genus, micro- and nano- grooves and 1D channels, surface wrinkles and micro-pillars^{16, 17, 23-27}. However, it has been shown over and over again (see our discussions in prior chapters), surface chemistry is equally important if not more important. First of all, LC molecules have to sense the substrate. The ability to pattern surface chemistry, therefore, will offer a powerful approach to direct LC alignment and generate topological defects through precise control of the azimuthal and zenithal orientations of LC directors on the local patterns of the desired anchoring surface. Moreover, a microscopically smooth (flat and curved) but chemically patterned surface will be highly advantageous as it can suppress light interference with the surface patterns, which are critical for applications in optical devices, for example, for wide viewing angles of LCDs²⁸ and graded-index micro-lenses²⁹. Current methods to create chemically patterned surfaces on molecularly smooth substrates include photo-patterning by UV exposure³⁰, micro-contact printing^{31, 32} of self-assembled monolayers (SAMs), and nanoimprint lithography followed by etching, chemical deposition, and lift-off^{33, 34}. For example, Gupta and Abbott³¹ create 1D gratings from striped SAMs, and show that 5CB forms homeotropic or random planar anchoring on alkanethiol SAMs depending on the alkane chain length, odd or even. Lee and Clark³⁰ pattern stripes with alternating homeotropic and randomly planar anchoring regions from isotropic octadecyltriethoxysilane (OTE) SAMs on glass where OTE coated region offers homeotropic anchoring and UV exposed glass region is randomly planar. Near the boundary line and its vicinity, which has a step of 1 nm height and 100 nm wide, they

observe predominantly twisted director structure. They then investigate the effect of the width of homeotropic and randomly planar regions, and find that if the width of the latter is sufficiently small, the boundary line alignment dominated the randomly planar regions, leading to uniform azimuthal anchoring of LCs on the randomly planar stripes with anchoring strength as large as that obtained from the rubbed polymer films. The groups of Abbott^{31, 35}, Scharf^{33, 34} and Evans³⁶ further demonstrate large area surface features in the form of squares, circles and stripes with pattern resolution up to 50 nm. It is suggested both from experimental observations^{30, 33, 34} and theory³⁷ that the surface coverage or relative ratio of areas with different anchoring characteristics plays an important role to the polar orientation of the LCs on the pattern, while the azimuthal orientation of LCs is determined by the direction of the chemical patterns. Cleaver *et al.*³⁸⁻⁴⁰ investigate both theoretically and experimentally LC anchoring on patterned SAMs with stripes, circles, and squared checkerboard patterns. Theory suggests competing alignments of NLCs on square patterns with alternating homeotropic and planar anchoring. Two distinct pairs of domain boundaries are suggested: one is T-like configuration (with bend and splay distortion) where the planar domain facing the homeotropic one and the other is X-like configuration (with twist distortion) at the corner of two regions. They conclude that such a square bridging domain is unstable since the symmetry change across the interface is spatially inhomogeneous. Experimentally, degenerate, bistable states at 45° to the checkerboard is observed, which is attributed to the intrinsic low azimuthal anchoring of the surface. Stable topological defects with “+1” charge are observed on circular patterns experimentally when the circle diameter is 10 μm or less³⁹. Whereas these prior studies

have demonstrated richness of chemically patterned surfaces in directing LC orientations and thus controlling topological defects, questions remain such as how to create stable defects with different topological charges, and whether the formation of topological defects can be guided by the geometry of the chemical patterns, how to take advantage of the possible switching of the LC orientation near the boundaries of homeotropic and planar anchoring domains.

In an attempt to address these questions, we use small molecule NLC, 4-Cyano-4'-pentylbiphenyl (5CB), as our model LC system, and study the anchoring behavior on chemical patterns of various geometries. To create a sharp boundary between homeotropic and planar anchoring domains, instead of micro-contact printing SAMs, here, we photo-pattern a thin layer (~200 nm) SU8 film on a flat glass substrate to generate the desired surface geometry with planar anchoring, followed by surface treatment with N,N-dimethyl-n-octadecyl-3-amino-propyltrimethoxysilyl chloride (DMOAP). By carefully tuning DMOAP treatment time, we successfully generate homeotropic anchoring on DMOAP coated regions, while keeping the regions patterned with SU8 planar. We investigate topological defect structures on the chemically patterned surfaces of different shapes, including circles, squares, and more complex geometries such as triplet and quadruplet circles, squared checkerboard and a square array of connecting rings, while keeping the pattern size the same as 10 μm . For all patterns, we only observed topological defect formation on the planar regions of the chemical patterns. In the case of isolated planar patterns, including circles, squares, triplet and quadruplet circles, we find that 5CB always displays “+1” defects regardless of the

pattern shape. However, on the connecting planar patterns, including squared checkerboard and the square arrays of connecting rings, we find that the formation of topological defects is critically dependent on the pattern geometry. On the array of rings, we obtain “-1/2” defects at the boundaries between the homeotropic and planar anchoring regions, while on the squared checkerboard, we achieve uniform LC alignment without topological defect. Finally, we used the “+1” defects of NLC on circular chemical patterns to trap micron-sized silica colloids.

6.2 Experimental methods

6.2.1 Materials.

N,N-dimethyl-n-octadecyl-3-amino-propyltrimethoxysilyl chloride (DMOAP), poly(vinyl) alcohol (PVA) and propylene glycol monomethyl ether acetate (PGMEA) were purchased from Sigma Aldrich and used as received. 4-Cyano-4'-pentylbiphenyl (5CB) was purchased from Kingston Chemicals Limited. Negative-tone photoresist, SU8-2, was purchased from MicroChem Corporation.

6.2.2 Characterization.

Liquid crystal alignment was characterized by an Olympus BX61 motorized optical microscope with crossed polarizers using CellSens software. Sample annealing was carried out on a Mettler FP82 and FP90 thermo-system hot stage under ambient condition. SEM imaging was performed on a dual beam FEI Strata DB 235 Focused Ion Beam (FIB)/ SEM instrument with 5KV electron-beam. AFM imaging was performed on a Bruker Icon AFM.

6.2.3 Micro-contact printing of SAMs.

A clean glass substrate was first treated with 1wt% PVA aqueous solution for 20 min, followed by washing with DI water for three times. The glass substrate was fully dried in a convention oven at 110°C for 1h. A PDMS stamp with cylindrical pores (diameter 60 μm , pitch or center to center distance 120 μm and depth 120 μm) was immersed in DMOAP solution of water/ethanol (1:9 v/v) for 10 min. DMOAP solution was varied with different concentration from 1vol% to 8vol% to fine tune the coating density of DMOAP. The stamp was then washed by DI water for three times. After drying with air gun, the PDMS stamp was gently pressed to the PVA coated glass and maintained for 2 min. The stamp was then carefully peeled off to obtain the chemical patterns from micro-contact printing of SAMs.

6.2.4 Photo-patterning of SU8 layer.

A typical photolithography process was applied to fabricate SU8 patterns. Glass substrates were pre-cleaned by washing with acetone three times, followed by drying with an air gun. After diluting SU8-2 solution received from the vendor by cyclopentanone (1:4 v/v), the solution was spin-coated (4000 rpm for 40s) on the pre-cleaned glass to obtain a thickness ~ 200 nm, followed by prebaking on a hot stage at 95°C for 1 min. The SU8 layer was then exposed to 365 nm UV light (Newport model 97436-1000-1, Hg source) through a photomask at a dosage of 200 mJ/cm^2 . After post-baking at 95°C for 1min, the sample was developed in PGMEA to obtain the final SU8 pattern.

6.2.5 DMOAP treatment

3 vol% DMOAP solution was prepared in a mixture of water/ethanol (1:9 v/v). For non-

patterned glass substrates, they were immersed in DMOAP solution for 30 min. For SU8 patterned glasses, DMOAP treatment was varied to find the optimal condition to generate homeotropic anchoring in non-patterned region while maintaining SU-8 patterned region planar. The DMOAP treated substrates were washed with deionized (DI) water three times and baking at 110 °C in a convection oven for 1 h.

6.2.6 Water contact angle measurement

Water contact angle was measured from a 5- μ L water droplet placed on the sample surface from Ramé-Hart standard automated goniometer (model 200) using the sessile drop method. For each water contact angle reported, it was averaged over three measurements at different locations of the sample.

6.2.7 Preparation of liquid crystal cells

Liquid crystal cells were constructed from one glass slide with chemical patterns and the other one as DMOAP treated non-patterned substrate. The thickness of the LC cells was controlled using a Mylar spacer ($\sim 50 \mu\text{m}$ thick). 5CB was then infiltrated into the LC cells through capillary filling. To remove the mechanical and thermal history of 5CB, samples were heated on a hot stage to 35°C to the isotropic phase and maintained for 1min, followed by slowly cooling down (1°C/min) to room temperature for the anchoring study with optical microscopy.

6.2.8 Assembly of colloids with liquid crystals

0.1 wt% of silica colloids (diameter, 1 μm) were well-dispersed in LCs, followed by capillary infiltration into the LC cell. The LC cell was then heated to the isotropic phase of LC and subsequently cooled down (1°C/min) to the nematic phase and maintained for

at least 1h before observation of colloid assembly under the optical microscope.

6.3 Preparation of chemically patterned surfaces

In spite of the azimuthal degeneracy of NLC on an isotropic surface, that is LCs are free to rotate in the surface plane, Lee and Clark³⁰ have demonstrated that spatially heterogeneous isotropic surfaces combining with LC elastic anisotropy could align LC. For many known NLCs, such as 5CB, twist distortion involves with minimum elastic energy penalty comparing to splay and bend. Therefore, at the local boundary of a chemically patterned surface, as illustrated in Figure 6.1a, rod-like NLCs prefer twist alignment that results in a mean director \mathbf{n} parallel to the boundary line on the planar surface. One simple implantation of this alignment scheme is to pattern the surface boundary coupling with the design of pattern geometry for the generation of topological defects. As shown in Figure 6.1b is a binary patterned surface with planar circles surrounding by homeotropic surface, in which azimuthal boundary anchoring of NLC leads to a concentric alignment of LC with a “+1” topological defect at the center, illustrated in Figure 6.1c. Such anchoring configuration has been experimentally verified by Cleaver *et al.* using micro-contact printing (μ CP) of organothiols on gold³⁹. Up to 87% uniform defects were obtained, and the rest 13% was identified as non-uniform where the LC directors were disordered³⁹.

Here, we first tested the idea of μ CP to prepare chemically patterned surfaces using silane SAMs (see Experimental methods and Figure 6.2), similar to the procedure reported in literature³⁹. We coated DMOAP on PVA surface to create chemical patterns

with alternating homeotropic and planar anchorings for 5CB. As shown in Figure 6.2, chemical patterns with planar anchored circles (diameter 60 μm) were prepared with different DMOAP concentration to fine-tune the silane coating density on the homeotropic region of the patterned surfaces. At a low DMOAP concentration (1 vol%), only partial coverage of the silane was obtained and non-uniform tilted anchoring of 5CB on DMOAP was observed as evident from the POM image - Figure 6.2a showing the light transmittance at the DMOAP coated region. With increasing DMOAP concentration, the homeotropic anchoring was substantially improved (Figure 6.2b-c). Nevertheless, as shown in Figure 6.2b-c, μCP of DMOAP on PVA failed to achieve uniform boundary lines between the planar and homeotropic regions in the chemical patterns, regardless of DMOAP coating density. Therefore, we developed a more effective approach to create the alternating chemical patternings. It involves with photopatterning of planar SU8 and kinetically control of the coating of homeotropic DMOAP on the substrate, as illustrated in Figure 6.1d.

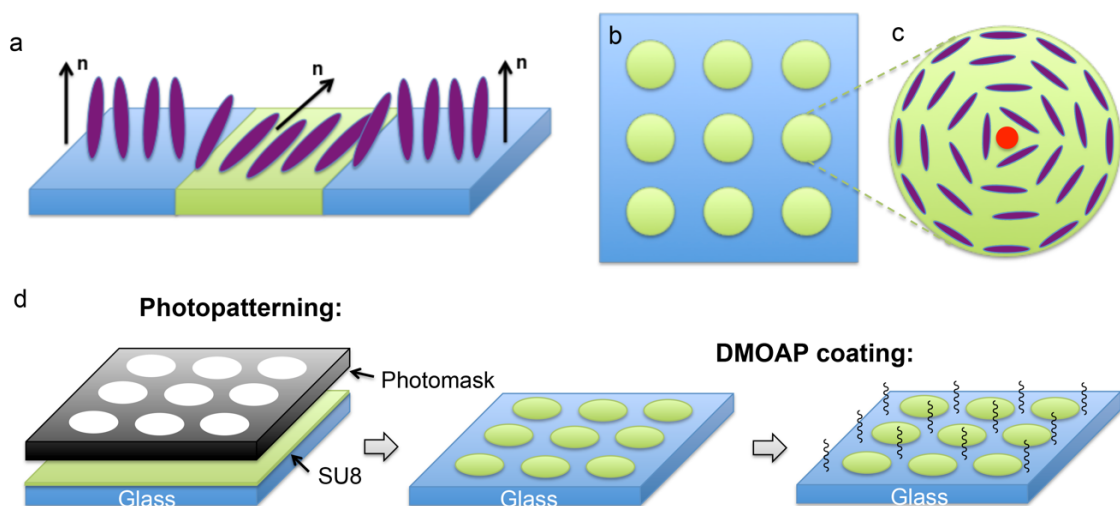


Figure 6.1 Schematic illustration of the design of the chemically patterned surface for controlled LC anchoring. (a) NLC at the boundaries of homeotropic and planar anchoring

domains represented by different colors: blue – homeotropic, green – planar, purple rods – LC mesogens. The black arrow represents the LC director (\mathbf{n}). A twist configuration of LC alignment at the boundary of homeotropic and planar regions is illustrated. (b) Illustration of the patterned surface with isolated circles. (c) NLC director field on the circular pattern shown in (b). Purple rods represent local LC director and the red dot indicates the “+1” point defect. (d) Illustration of the sample preparation process. Different colors represent different materials: Blue – glass, green – SU8.

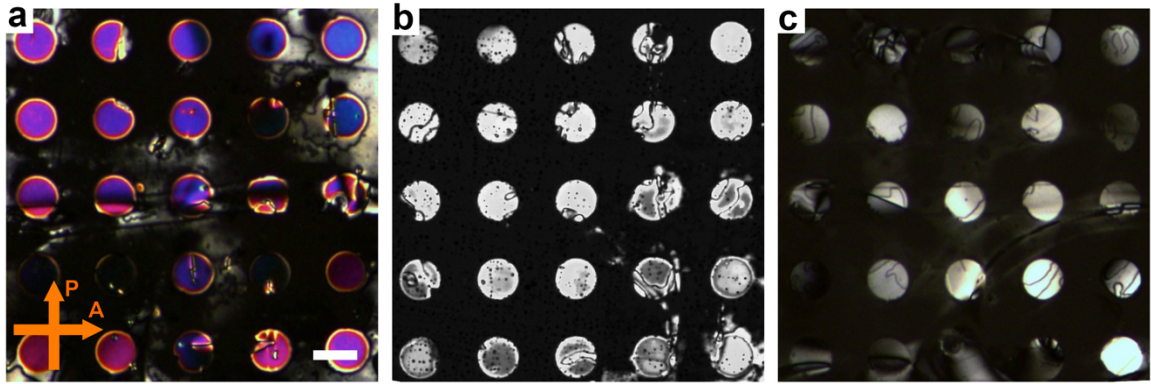


Figure 6.2 POM images of 5CB on chemical patterns prepared by μ CP of DMOAP of different concentrations. (a) 1 vol%; (b) 3 vol%; (c) 8 vol%. Scale bar: 60 μ m.

We prepared designed SU8 pattern on a glass substrate by photolithography through a photomask (see Figure 6.1d & Experimental methods), followed by immersing the substrate in DMOAP solution to make the non-SU8 patterned regions homeotropic for 5CB. Here, DMOAP treatment time is critical as SU8 may also slowly react with the silane (DMOAP) and change the surface chemistry. To maximize the surface anchoring contrast, it is important to optimize the DMOPA treatment time. First, we investigated the reaction kinetics of DMOAP with glass and SU8 by monitoring water contact angle (WCA) change over time. As shown in Figure 6.3a, the initial WCAs on a clean glass and SU8 film were 19° and 63° , respectively. The WCA on DMOAP treated glass quickly increased to 82° and leveled at 2-3 min treatment time, while WCA of DMOAP treated

SU8 showed no significant change during this time span (Figure 6.3a). Even after 15 min treatment, WCA on DMOAP treated SU8 remained at 64°, lower than that on DMOAP treated glass after 2 min, suggesting that SU8 surface is thermodynamically unattractive to DMOAP. To maximize the chemical contrast on the patterned SU8/glass surfaces in our study, we chose 2 min as the optimal DMOAP treatment time.

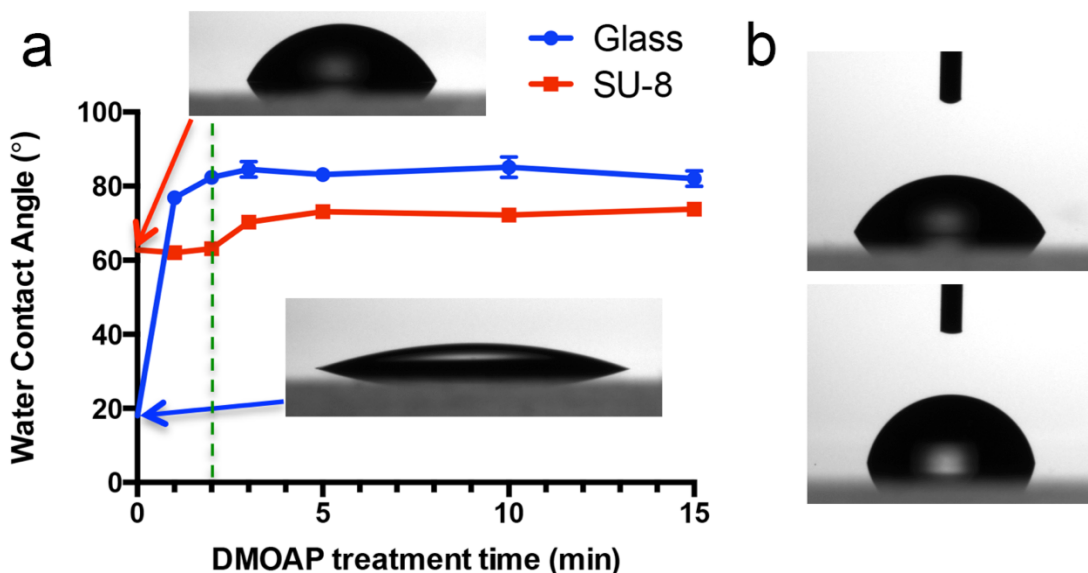


Figure 6.3 Reaction kinetics of DMOAP with SU8 and glass based on the change of water contact angles over time. (a) Water contact angles of glass and SU8 after different DMOAP treatment time. Inset: optical microscopy (OM) images of water droplets on the sample surface. Green dotted line indicates the optimized DMOAP treatment time (2 min). (b) OM images of water droplets on SU8 (top panel) and glass (bottom panel) after 2 min DMOAP treatment.

6.4 LC anchoring study on chemical patterns

To validate the control of LC anchoring on the patterned SU8/glass surface, we investigated 5CB alignment on the square array of circular patterns (Figure 6.4). Figure 6.4a shows an array of planar circles with diameter of 10 μm and pitch (center-to-center

distance) of 20 μm . Uniformly patterned “+1” defects were observed over entire 2 cm-wide sample area (Figure 6.4a). Indeed, nearly 100% of the patterns had uniform defects with the classical four-brush textures under POM, albeit the position of the topological defect on each circle slightly varied. According to theory³⁹, stable “+1” defects on the circular patterns generated from the concentric LC anchoring should appear at the center of each circle when the circle diameter is 10 μm or less. To further verify the position of the “+1” defects, we used bright field (BF) imaging to accurately show the location of the defects comparing to the boundary of the circles. Under BF microscopy, topological defects appeared as black dots due to light scattering in the defect regions (Figure 6.4a inset). As seen from the inset in Figure 6.4a, the black dots in the circles have small positional deviation from the center of each circular pattern, suggesting the topological defects on the 2D surfaces are kinetically trapped by the surface; relaxation of free energy towards the ground state requires more careful annealing of the sample. It should be noted here that since we used SU8 photo-patterning method to prepare the chemical patterns, the surface topography of our samples is somewhat different from the samples prepared by micro-contact printing of SAMs, which has height of a few nm³⁹. Atomic force microscopy (AFM) study of the surface topography showed that the height of the circles in our study is ~ 200 nm (Figure 6.4b). However, as evident from Figure 6.4a, such small topography of the chemically patterned surface showed negligible influence on the LC anchoring and defect formation.

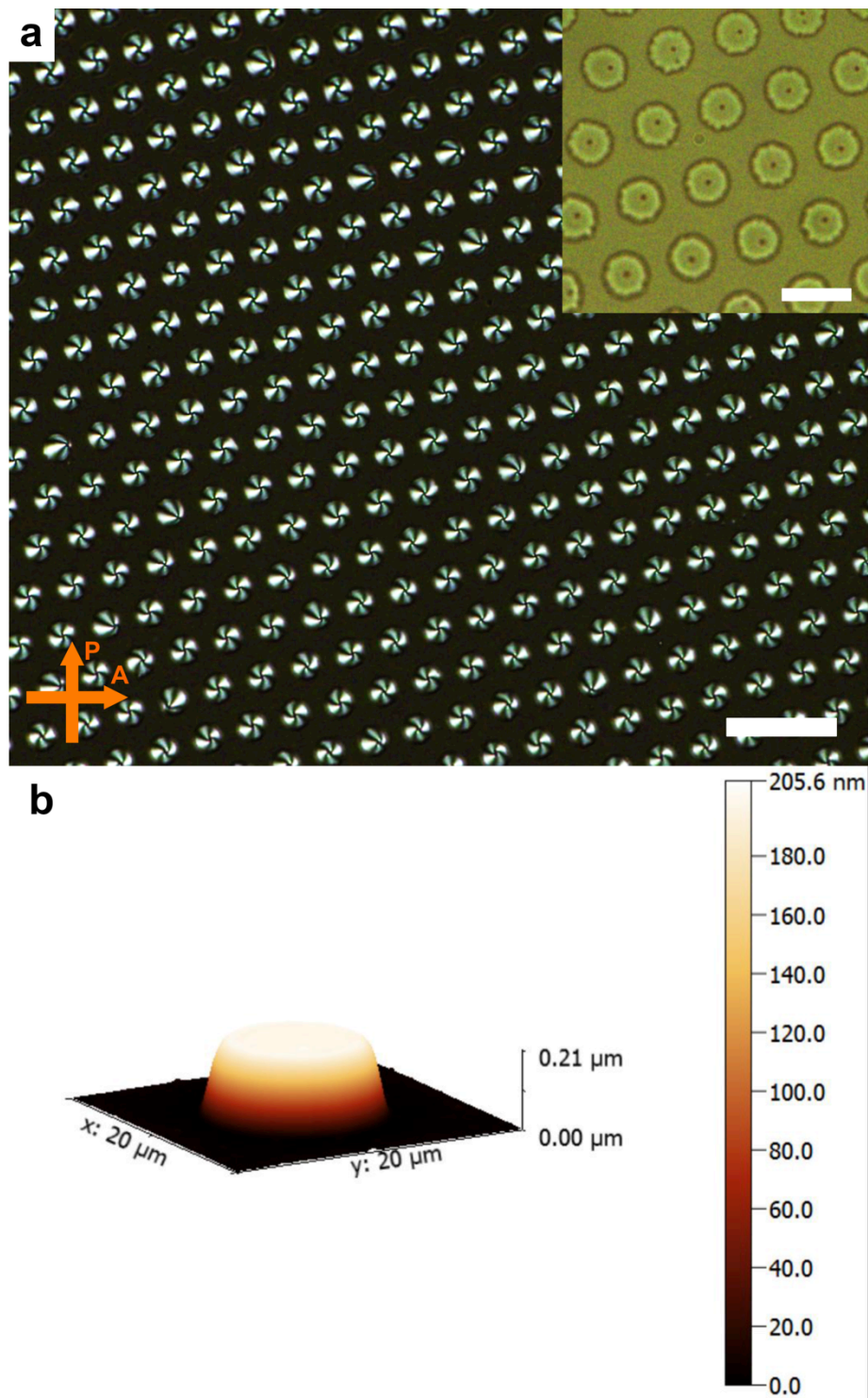


Figure 6.4 5CB on an array of circular patterns. (a) Polarized optical microscopy (POM) image of 5CB on the circular patterns. “+1” defects were found on each individual circle. Scale bar: 50 μm. Inset: Bright field (BF) image showing the circular patterns with

topological defects of 5CB (black dots). Scale bar: 20 μm . (b) AFM image of a single SU8 circle on glass.

Armed with the careful study on the circular patterns, we then investigated chemical patterns with various shapes, as shown in Figure 6.5. The SEM images in Figure 6.5a-c showed three different patterns, in which the sharp corners in the patterns were rounded due to the resolution limit of a contact photo-lithography under a UV lamp (see Experimental methods). In spite of the complex shapes of the chemical patterns, only “+1” topological defects were observed (Figure 6.5, bottom panel). It indicates that pattern geometry has negligible effect on the LC anchoring, yet it could affect the location of defect formation. In the case of complex boundary geometries, we found defects were not necessarily formed at the center of the pattern, but could be simply trapped and required much longer annealing time to achieve uniform defect structures comparing to that of 5CB on the circular patterns. One notable difference between the circular pattern and the square pattern is the different extents of elastic distortions required to accommodate the boundary constrains. LCs on the circular patterns possess much higher bending curvature (energy) than that of square pattern, suggesting LC anchoring on circular pattern is more energetically favorable to approach the minimum free energy state. Therefore, relaxation of LC director field on a circular pattern involved much faster kinetics. In the case of triplet and quadruplet circle patterns, the pattern size may play an essential role. The complex patterns had much larger pattern area – 2 - 3 times bigger than that of circular pattern shown in Figure 6.4, leading to smaller elastic distortions to accommodate the boundary conditions; therefore they showed much slower

relaxation kinetics of the LC director field. The pattern size effect was previously observed in literature^{30, 39} that larger patterns showed much lower probability of forming uniform LC defect structures. Nevertheless, we concluded from our observations that LC anchoring on isolated chemical patterns had no dependence on pattern geometry.

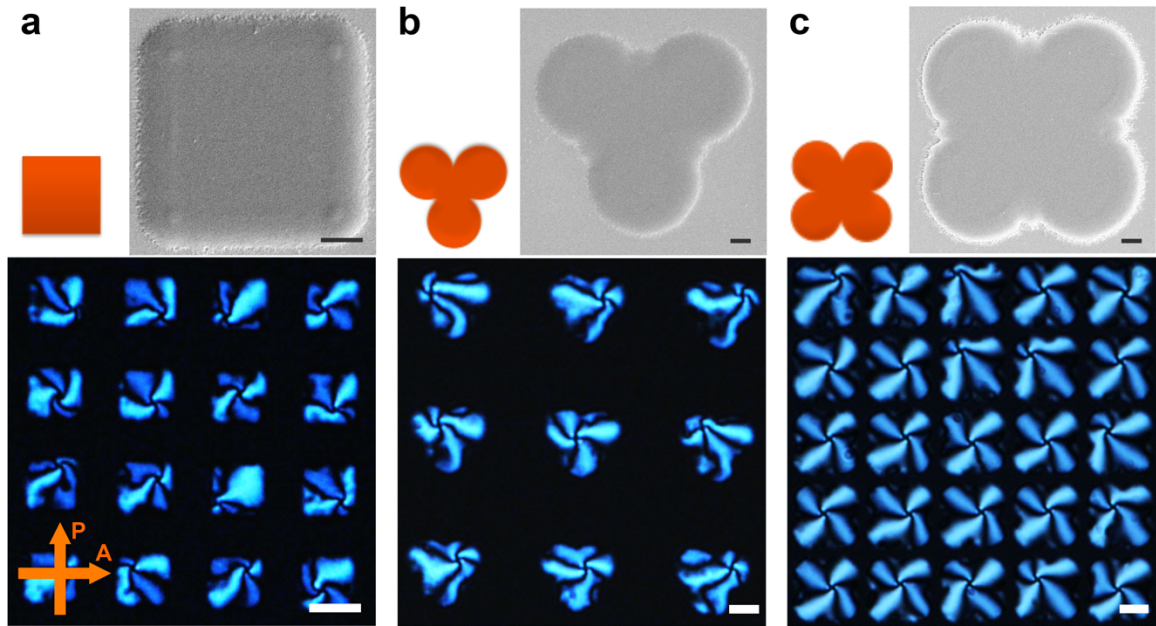


Figure 6.5 5CB on various chemical patterns. Top panels: designs and SEM images of the patterns. Bottom panels: POM images of 5CB on chemical patterns with shape of (a) square, (b) triplet of circles and (c) quadruplet of circles. Scale bars: top panels – 2 μm , bottom panels – 10 μm .

In another setting, we prepared patterns with connecting boundaries, including squared checkerboard and square array of connecting rings, to study LC anchoring and defect formation (see Figure 6.6). Interestingly, 5CB on checkerboard showed no apparent defect but uniform azimuthal orientation that most of the LC molecules aligned at 45° along with the pattern lattice (Figure 6.6a-b). The BF image further confirmed our observation of the non-defect LC alignment (Figure 6.6b inset). Recall that 5CB on an

isolated square pattern gave “+1” defect to accommodate boundary conditions (Figure 6.5a), where LC molecules energetically chose twist distortion across the homeotropic-planar boundary line. However, in the case of checkerboard with alternating homeotropic and planar anchoring domains, 5CB molecules adopted twist distortion at the side of the square, and splay/bend distortions at the two corners of the square to avoid the formation of topological defect. Similar results have been reported in literature^{38, 39}. Notably, the homeotropic domains in our sample displayed light transmittance under POM and colored pale red (Figure 6.6a), indicating LC molecules in this domain were no longer fully homeotropic but tilted from the easy axis. From Figure 6.6a-b we could determine the tilting direction of LC was also at 45° with the pattern lattice. However, such phenomenon was not observed from 5CB on the array of rings, as shown in Figure 6.6c-d. Confirmed by POM imaging, LCs on the homeotropic domains of the array of rings displayed negligible tilting behavior from the easy axis since no light transmittance was detectable under the cross polarizers. Moreover, topological defects were found on the array of rings. Such topological defects were corroborated by BF image (Figure 6.6d inset), and POM images (Figure 6.6c-d). As evident from Figure 6.6c-d, classical two-brush textures were observed under POM, suggesting “half-charge” defects. Noting that LC director field was mostly uniformly oriented in this sample, we proposed the LC alignment in Figure 6.6e. As shown in the illustration, the “-1/2” topological defect was constructed on the right side of the homeotropic domain while uniform LC orientation presented on the other side, consistent with the POM imaging. Indicated from the POM observation, 5CB molecules on the array of rings are energetically favored to form topological defects in order to avoid the expensive bend distortions on the rings. As one

can clearly see in Figure 6.6c-d, LC director field was mostly orientated parallel to the direction of the pattern lattice that involved with minor elastic distortion; therefore, the free energy penalty required to accommodate the curved boundary conditions is only centered near the defect area. Astonishingly, however, no such defect was formed on the left side of the homeotropic domain, despite the four-fold symmetry of the pattern. As illustrated in Figure 6.6e, uniform LC director field on the left side of the domain applied “splay” distortions at the borderline to accommodate the boundary constrains. This anchoring configuration was, to some extent, similar to the LC configuration on the squared checkerboard, where splay distortions were adopted at the corner of the squares to avoid defects. Therefore, unlike in the system of isolated patterns, LC anchoring and defect structures formed on connecting chemical patterns with alternating anchoring behaviors indeed are highly dependent on pattern geometry.

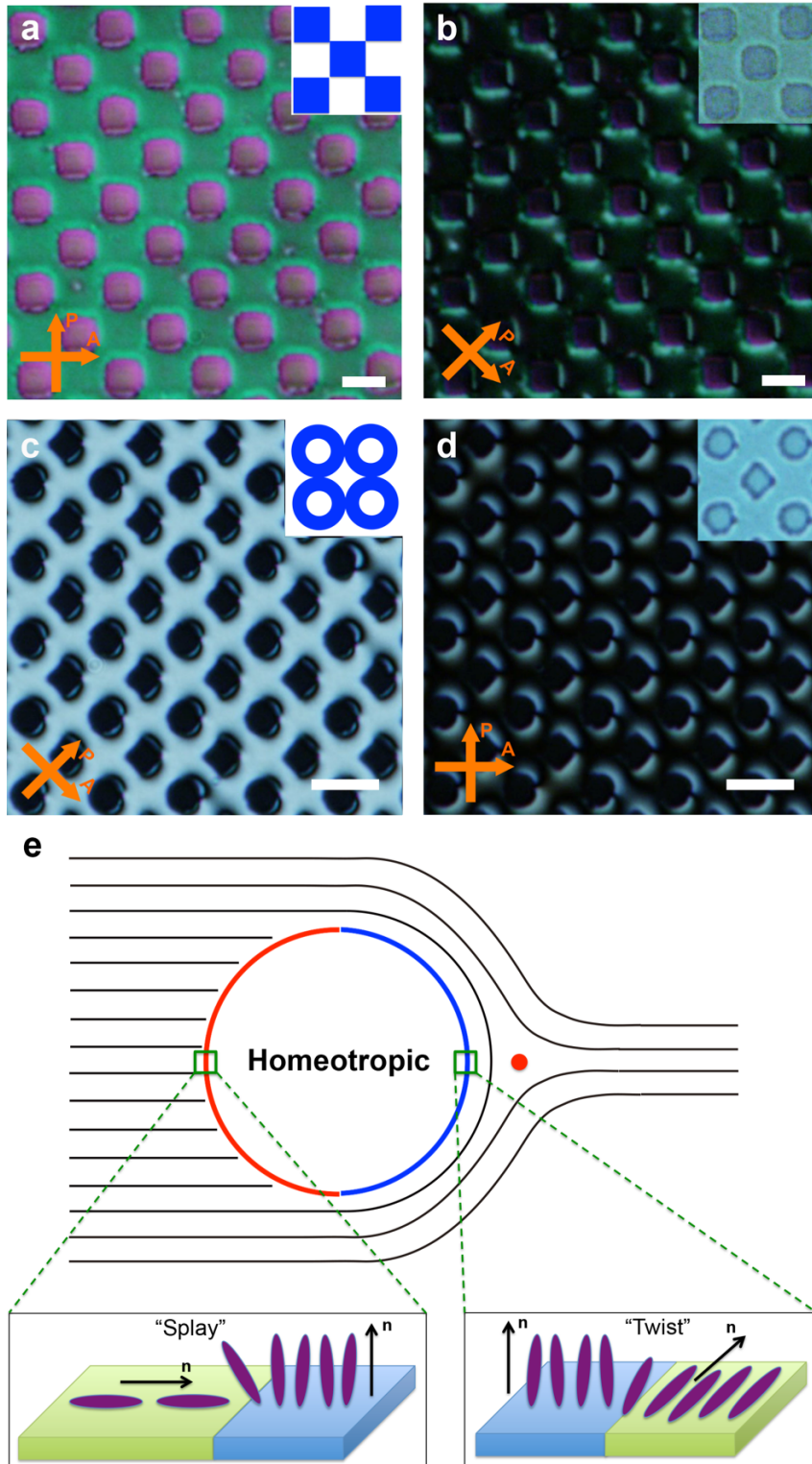


Figure 6.6 5CB on arrays of squared checkerboard and connecting rings. (a-b) POM images of 5CB on the squared checkerboard with 0° (a) and 45° (b) cross-polarizer

angles, respectively. (c-d) POM images of 5CB on the square array of connecting rings with 45° (c) and 0° (d) cross-polarizer angles, respectively. Insets in (a) & (c) show the schematic of the arrays. Insets in (b) & (d) show the BF images of 5CB with no apparent defects in (b) but tilted defects in (d) appeared as black dots. (e) Schematic illustration of the LC director field surrounding a homeotropic domain. The black lines represent LC director field, and the red dot shows the “ $-1/2$ ” defect. The red and blue curves at the boundary of the chemical pattern illustrate two different LC anchoring configurations: the splay distortion and twist distortion shown in the schematics below. Scale bars: (a-b) 10 μm ; (c-d) 40 μm .

6.5 Trapping microparticles within LC topological defects

With the ability to control LC alignment and defect structures using chemical patterns, we then studied the assembly of colloids within the topological defects. As a proof-of-concept, we used the circular square array to create “+1” defects to trap the untreated silica colloids (diameter of 1 μm), which has weak planar anchoring to 5CB. As shown in Figure 6.7, when silica colloids were dispersed into 5CB, they were readily trapped into the defects as indicated by the red arrows in Figure 6.7a. POM image (Figure 6.7b) suggested that LC director on the circular pattern surface was slightly distorted; the “+1” defects seemed to be partially diminished to relax the distorted director field into the bipolar configuration to accommodate the director distortion by the trapped silica colloids. Nevertheless, the four-brush textures could still be seen on some of the circular patterns. It is noted, however, that since the topological defects and most of the LC director distortions exist in the near field of the patterned surface, migration of microparticles towards the defect area has a smaller energetic potential, and thus takes longer time, comparing to those with bulk LC defects. Considering that creating stable and uniform bulk defects in NLC is somewhat challenging, we believe this work demonstrated here using smooth chemical patterns offers great potentials to generate

surface topological defects to facilitate colloid assemblies.

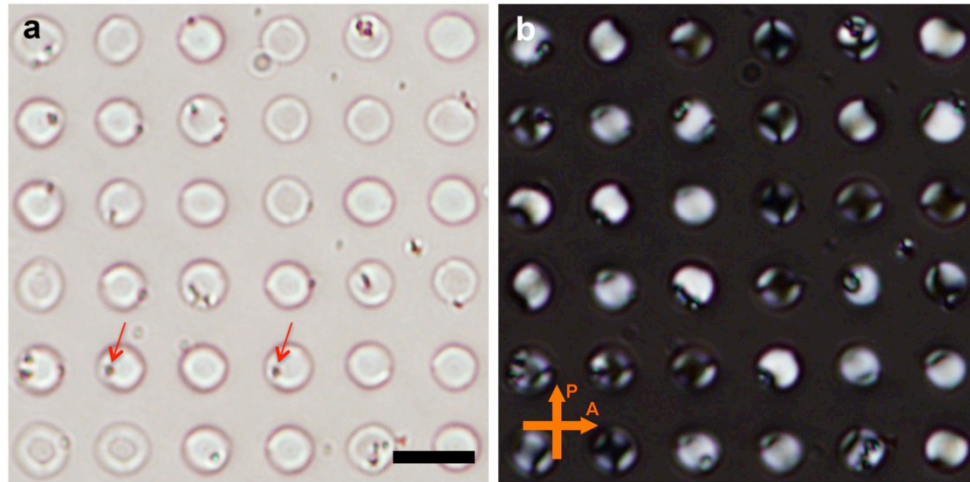


Figure 6.7 (a) BF and (b) POM images of the assembly of silica colloids (diameter of 1 μm) within the topological defects created by 5CB on the square array of circular patterns. The red arrows indicate the trapped colloids by the topological defects of 5CB. Scale bar: 20 μm .

6.6 Conclusions

In this work, we demonstrated a new approach to prepare chemically patterned surfaces for LC anchoring and defect formation through direct photo-patterning degenerated planar SU8 on glass. Taking advantage of different silane reaction kinetics with SU8 and glass, we optimized the treatment time (2min) of homeotropic DMOAP on patterned substrate to maximize the anchoring contrast of LCs on different regions of the SU8/glass patterned surface. We prepared several SU8 patterns with various pattern geometries to study LC anchoring under 2D boundary constrains. On the isolated patterns, such as circles, squares, triplet and quadruplet of circles, “+1” defects were formed regardless of the pattern geometry. On the connecting patterns, including squared

checkerboard and arrays of connecting rings, LC anchoring was highly dependent on the pattern geometry: no topological defect was observed on the checkerboard pattern while the “-1/2” defect array was observed on the array of rings. Finally, we demonstrated preliminary results of trapping silica particles by topological defects generated from the chemical pattern of circular array. Further studies will be carried out from silica colloids with different surface treatments and variable sizes.

The chemical patterning method we demonstrate here is simple yet highly robust for generating LC phase gratings with embedded topological defects. The ability to precisely control LC anchoring and defect structures will offer great potentials to advance applications of LC optical and electronic devices, *e.g.* wide-viewing angle LCDs, diffractive and refractive optical lenses, spectral dispersion and imaging elements. Meanwhile, the trapping and assembly of colloidal particles by topological defects on the chemically patterned surfaces can be extended to the patterning of functional nanoparticles (*e.g.* Au nanorods and quantum dots) for energy harvesting and novel display applications. Along with the ability of accurately patterning topological defects, our technique can be further applied to fabricate liquid crystal elastomers (LCEs) with complex LC director field of embedded topological defects, thereby allowing us to design sophisticated and monolithic LCE actuation from *origami* folding to *Kirigami* shape transformation from 2D to 3D.

6.7 Contributions

Y.X. and S.Y. conceived the idea and designed the experiments. H.N. K. performed with

the colloidal trapping study. G.X. W. helped with the water contact angle and AFM measurements.

6.8 References

1. Lu K, Lu L, & Suresh S (2009) Strengthening Materials by Engineering Coherent Internal Boundaries at the Nanoscale. *Science (New York, N.Y.)* 324(5925):349-352.
2. Sachet E, *et al.* (2015) Dysprosium-doped cadmium oxide as a gateway material for mid-infrared plasmonics. *Nat. Mater.* 14(4):414-420.
3. Weber CA, Bock C, & Frey E (2014) Defect-Mediated Phase Transitions in Active Soft Matter. *Phys. Rev. Lett.* 112(16):168301.
4. Alsayed AM, Islam MF, Zhang J, Collings PJ, & Yodh AG (2005) Premelting at Defects Within Bulk Colloidal Crystals. *Science (New York, N.Y.)* 309(5738):1207-1210.
5. Alden JS, *et al.* (2013) Strain solitons and topological defects in bilayer graphene. *Proc. Natl. Acad. Sci.* 110(28):11256-11260.
6. van der Zande AM, *et al.* (2013) Grains and grain boundaries in highly crystalline monolayer molybdenum disulphide. *Nat. Mater.* 12(6):554-561.
7. Ohm C, Brehmer M, & Zentel R (2010) Liquid Crystalline Elastomers as Actuators and Sensors. *Adv. Mater.* 22(31):3366-3387.
8. Zhao X, *et al.* (2010) Molecular self-assembly and applications of designer peptide amphiphiles. *Chem. Soc. Rev.* 39(9):3480-3498.
9. Chakrabarty R, Mukherjee PS, & Stang PJ (2011) Supramolecular Coordination: Self-Assembly of Finite Two- and Three-Dimensional Ensembles. *Chem. Rev.* 111(11):6810-6918.
10. Ware TH, McConney ME, Wie JJ, Tondiglia VP, & White TJ (2015) Voxelated liquid crystal elastomers. *Science (New York, N.Y.)* 347(6225):982-984.
11. McConney ME, *et al.* (2013) Topography from Topology: Photoinduced Surface Features Generated in Liquid Crystal Polymer Networks. *Adv. Mater.* 25(41):5880-5885.
12. de Haan LT, Sánchez-Somolinos C, Bastiaansen CMW, Schenning APHJ, & Broer DJ (2012) Engineering of Complex Order and the Macroscopic Deformation of Liquid Crystal Polymer Networks. *Angew. Chem.* 124(50):12637-12640.
13. Serra F, *et al.* (2013) Nematic Liquid Crystals Embedded in Cubic Microlattices: Memory Effects and Bistable Pixels. *Adv. Funct. Mater.* 23(32):3990-3994.
14. Musevic I & Zumer S (2011) Liquid crystals: Maximizing memory. *Nat. Mater.* 10(4):266-268.
15. Serra F, *et al.* (2011) Topological defects of nematic liquid crystals confined in porous networks. *Soft Matter* 7(22):10945-10950.
16. Cavallaro M, *et al.* (2013) Exploiting imperfections in the bulk to direct assembly of

- surface colloids. *Proc. Natl. Acad. Sci.* 110(47):18804-18808.
17. Muševič I, Škarabot M, Tkalec U, Ravnik M, & Žumer S (2006) Two-Dimensional Nematic Colloidal Crystals Self-Assembled by Topological Defects. *Science (New York, N.Y.)* 313(5789):954-958.
 18. Rahimi M, *et al.* (2015) Nanoparticle self-assembly at the interface of liquid crystal droplets. *Proc. Natl. Acad. Sci.* 112(17):5297-5302.
 19. Honglawan A, *et al.* (2015) Synergistic assembly of nanoparticles in smectic liquid crystals. *Soft Matter* 11(37):7367-7375.
 20. Rodarte AL, *et al.* (2015) Self-assembled nanoparticle micro-shells templated by liquid crystal sorting. *Soft Matter* 11(9):1701-1707.
 21. Milette J, *et al.* (2012) Reversible long-range patterning of gold nanoparticles by smectic liquid crystals. *Soft Matter* 8(24):6593-6598.
 22. Wang X, Miller DS, Bukusoglu E, de Pablo JJ, & Abbott NL (2016) Topological defects in liquid crystals as templates for molecular self-assembly. *Nat. Mater.* 15(1):106-112.
 23. Lapointe CP, Mason TG, & Smalyukh II (2009) Shape-Controlled Colloidal Interactions in Nematic Liquid Crystals. *Science (New York, N.Y.)* 326(5956):1083-1086.
 24. Poulin P, Stark H, Lubensky TC, & Weitz DA (1997) Novel Colloidal Interactions in Anisotropic Fluids. *Science (New York, N.Y.)* 275(5307):1770-1773.
 25. Senyuk B, *et al.* (2013) Topological colloids. *Nature* 493(7431):200-205.
 26. Berreman DW (1972) Solid Surface Shape and the Alignment of an Adjacent Nematic Liquid Crystal. *Phys. Rev. Lett.* 28(26):1683-1686.
 27. Abbott NL (1997) Surface effects on orientation of liquid crystals. *Curr. Opin. Colloid Interface Sci.* 2(1):76-82.
 28. Schadt M, Seiberle H, & Schuster A (1996) Optical patterning of multi-domain liquid-crystal displays with wide viewing angles. *Nature* 381(6579):212-215.
 29. Honma M, Nose T, Yanase S, Yamaguchi R, & Sato S (2009) Liquid-crystal variable-focus lenses with a spatially-distributed tilt angles. *Opt. Express* 17(13):10998-11006.
 30. Lee B-w & Clark NA (2001) Alignment of Liquid Crystals with Patterned Isotropic Surfaces. *Science (New York, N.Y.)* 291(5513):2576-2580.
 31. Gupta VK & Abbott NL (1997) Design of Surfaces for Patterned Alignment of Liquid Crystals on Planar and Curved Substrates. *Science (New York, N.Y.)* 276(5318):1533-1536.
 32. Son J-H, Zin W-C, Takezoe H, & Song J-K (2012) Alignment of Liquid Crystals Using a Molecular Layer with Patterned Molecular Density. *Adv. Mater.* 24(45):6105-6110.
 33. Park S, Padeste C, Schiff H, Gobrecht J, & Scharf T (2005) Chemical Nanopatterns via Nanoimprint Lithography for Simultaneous Control over Azimuthal and Polar Alignment of Liquid Crystals. *Adv. Mater.* 17(11):1398-1401.
 34. Scharf T, *et al.* (2005) Liquid Crystal Alignment on Chemical Nanopatterns: Control over Azimuthal and Polar Alignment. *Mol. Cryst. Liq. Cryst.* 438(1):55/[1619]-1665/[1629].

35. Drawhorn RA & Abbott NL (1995) Anchoring of Nematic Liquid Crystals on Self-Assembled Monolayers Formed from Alkanethiols on Semitransparent Films of Gold. *J. Phys. Chem.* 99(45):16511-16515.
36. Cheng YL, *et al.* (2000) Imaging of micropatterned self-assembled monolayers with adsorbed liquid crystals. *Liq. Cryst.* 27(10):1267-1275.
37. Anquetil-Deck C & Cleaver DJ (2010) Nematic liquid-crystal alignment on stripe-patterned substrates. *Phys. Rev. E* 82(3):031709.
38. Anquetil-Deck C, Cleaver DJ, & Atherton TJ (2012) Competing alignments of nematic liquid crystals on square-patterned substrates. *Phys. Rev. E* 86(4):041707.
39. Bramble JP, *et al.* (2007) Nematic liquid crystal alignment on chemical patterns. *Liq. Cryst.* 34(9):1059-1069.
40. Anquetil-Deck C, Cleaver DJ, Bramble JP, & Atherton TJ (2013) Independent control of polar and azimuthal anchoring. *Phys. Rev. E* 88(1):012501.

CHAPTER 7: Summary and Outlook

7.1 Summary

7.1.1 Control of molecular alignment and defect structures of small molecule liquid crystals for direct self-assembly of responsive materials

The alignment of small molecule LCs at boundaries is usually achieved by use of surface chemistry, topography, and topology. In the micro-pillar arrays, we demonstrate large-scale assembly of LC molecules into desired defect structures through surface chemistry and topography for dynamic tuning of surface plasmon resonance (SPR) of AuNRs. By imposing homeotropic anchoring condition on the surface of the micropillars, stable bulk disclinations can be formed in the nematic LC phase at precise locations encircling each pillar, and fine-tuned by varying the pillar dimension and the temperature of the system. When AuNRs are dispersed in the LC, they energetically favor to migrate to the LC defects and assemble. The assembly of the AuNRs and consequently the surface plasmonic resonance peaks can be dynamically and reversibly tuned by varying the dimensions of the disclination rings through heating and cooling of the entire system across the phase transitions. By comparing different surface treatments on the micropillar surface, we show that homeotropic anchoring of micropillars with an aspect ratio of 1.3 induces the largest local surface plasmon peak shifts that are up to ~ 100 nm and ~ 153 nm for transverse and longitudinal SPR, respectively. In comparison, the defects between micropillar arrays with planar anchoring are highly disordered and AuNRs in the planar anchoring micropillars show no apparent temperature dependent peak shift. Similarly, no plasmon resonance peak is present in the AuNRs/LC system in a flat LC cell with

homeotropic anchoring.

We further demonstrate nematic LC anchoring control and defect formation on chemically patterned surfaces. We prepare planar anchoring SU8 patterns on homeotropic DMOAP coated glass substrates to create micron-sized chemical patterns. By exploiting the geometry of the boundaries of the chemical patterns, combining with LC elastic anisotropy, we show that LC orientation can be precisely controlled and various topological defects can be formed. On the isolated SU8 patterns, such as circles, squares, triplet and quadruplet of circles, “+1” defects are formed regardless of the pattern geometry. On the continuous patterns, including squared checkerboard and arrays of touching rings, LC anchoring is highly dependent on the pattern geometry: no topological defect was observed on the checkerboard pattern while the “-1/2” defect array is observed on the array of rings. Furthermore, we demonstrate preliminary results of trapping silica colloid particles by topological defects generated from the chemical pattern of circular array. Further studies will be carried out from silica colloids with different surface treatments and variable sizes.

7.1.2 Control of molecular alignment and defect structures of liquid crystal monomers for nano-scale imaging and actuation

Different from the methods in controlling alignment of small molecule LCs, techniques used to date to align LCMs mainly rely on application of external fields, including mechanical force and magnetic field. Use of surface chemistry or topography to align LCMs has not been very effective for LCMs, especially in the nematic phase. We show that the origin of this problem is the stability of LCMs in the nematic phase that is related to the core energy of the LCMs. By design of stable nematic LCMs based on

strong intermolecular dipole-dipole interactions, we show that LCMs can achieve faithful anchoring at boundaries controlled through surface chemistry, surface topography and topology, analogous to the behaviors of small molecule LCs. When such LCMs are subsequently crosslinked via photopolymerization, we show that LC anchoring is not changed, while the orientational order of mesogens can be effectively locked, allowing for direct visualization of the LC director field and defect structures in the nanoscale (~100 nm resolution) by SEM in comparison to optical microscopy methods. We demonstrate that our method is effective to study LC anchoring in a variety of settings, including escaping LC configuration in 1D channels, pores and between micro-pillars, and more complex director field with topological defects and even metastable configurations. Further, SEM images allow us to calculate the extrapolation length of the LCM for planar and homeotropic anchoring, which is extremely difficult for unknown LC molecules.

Armed by the understanding of LCM alignment control, we investigate the self-assembly of LCMs in a confined geometry of micro-pore array. Landau-De Gennes numerical modeling is first employed to understand the surface chemistry cue in the system, which suggests that uniform vertical alignment of LCMs in the micro-pores can be achieved only in a PDMS mold of planar anchoring surface. To test the simulation, we coat the PDMS mold with a thin layer of hydrophilic poly(2-hydroxyethyl methacrylate) (PHEMA), switching LCM anchoring from homeotropic (on untreated PDMS) to planar anchoring. The resulting LCE pillars exhibit a large and reversible radial strain (~30%) upon heating above T_{NI} transition. In comparison, negligible strain is obtained from LCE pillars fabricated from untreated PDMS molds with polydomain LC alignment.

We further develop a new technique to direct LCM alignment on patterned 1D channels, and to program LCE actuation with complex LC director profiles. By exploiting the confinement of the topographical 1D channels, nematic LCMs can be faithfully oriented by the local channels. Strong anchoring at the surface can be achieved by optimizing the surface chemistry and surface topography of the channel. We demonstrate that epoxy 1D channels (planar anchoring surface chemistry) with a channel width 2 μm , pitch 4 μm , and depth 1.5 μm can provide faithful alignment of complex LCM director profile. Compared with photoalignment method to pre-program the LCM director profiles, our method affords simplicity, low cost, and easy access for the fabrication process. The LCE 2D sheets with pre-programmed topological defects show shape transformation to complex 3D objects through controllable bending and stretching. For example, the LCE sheet embedded with “+1” and “-1” defect array is transformed into a “cone” array and that with “+1/2” and “-1/2” defect array is curled into a 3D “wrinkle-like” structure upon heating above T_{NI} .

7.2 Outlook

The functionality of a LC material exquisitely relies on the molecular level organization of LC molecules that can be dictated by a variety of boundary conditions – surface chemistry, topography, and topology. The success of the \$100 billion LCD industry is one of the fine examples of directing LC orientation in a device. The ability to control topological defects has just become a powerful tool for templating and actuation of nano- and micro-objects¹⁻⁷. To further exploit the anisotropy of LC molecules for both scientific advancement of soft matter and technological applications, it is critically

important to improve our understanding and precisely control of LC orientation uniformly in a nano-/microstructures over a large area. Along the line, we need to develop new methods that can characterize LC director field and thus defect structures at the nanoscale.

In this thesis, we develop a series of new LC anchoring systems and methods to control LC anchoring and to apply them in responsive functional materials. The new LCM system with strong dipole-dipole interactions⁸ that we designed and synthesized offers a new concept of stable nematic phase to precise control of molecular anchoring and alignment on different boundary conditions. The molecular design strategy can be extended to other substituents (e.g. to induce hydrogen bonding) and bridging groups that connect the mesogen and epoxy group in order to fine-tune the mesomorphic properties. With faithful anchoring control, we expect the new LCMs can be applied in the design and fabrication of novel LCEs for actuators with complex director field for the application of artificial muscles and LC sensors, and LCPs for optics with convoluted light guiding properties. The stable LCMs can be used to prepare Kevlar-like high-strength fibers due to the strong ability of molecular aligning. Moreover, the newfound ability of mapping LC director field at nanoscale by using our new LCM provides us with new tools to enhance our understanding of anchoring, defects, and elasticity of nematics. In turn, it will equip us to further control the bulk structures *via* nanoscale patterning of the substrate and surface chemistry. We envision that by directly photopatterning a 2D sheet of NLC elastomer or glass with embedded topological defects and elasticity, followed by actuation by heat or light, we could pre-program the transform the folding of a 2D sheet into 3D.

The concept of using surface chemistry and topography to control LC anchoring is much simpler and, in some ways, more effective than the use of an external field or photoalignment to direct LC orientation, especially in the LC systems of complex geometry, such as porous membranes, channels, and 3D structures. The actuation of LCE micropillars realized by controlling surface chemistry can be extended to other LCE systems, e.g. light responsive LCEs, smectic, cholesteric and blue phase LCEs. Furthermore, tuning surface chemistry in soft lithography molds can be further applied to fabricate a variety of micro- and nano-structures with a rich library of LCE actuation that can be potentially employed in muscle-like actuators, sensors, displays, dry adhesion, photonic materials, and *origami* assembly. The use of patterned 1D channels to align LCMs would enable the creation of LCEs with complex LC director field with topological defects embedded within, thereby allowing to design sophisticated and monolithic LCE actuation from *origami* folding to *Kirigami* shape transformation from 2D to 3D. By carefully designing LC director field with gradient crosslinking density of the polymer network, 4D *origami* and *Kirigami* folding, in which shape transformation is dependent with time evolution, could be also expected in response to heat or light. Therefore, through precise control of the magnitude and directionality of local strain in combination with elaborate geometrical design, such LCEs can be envisioned to enable enhancement and miniaturization of novel soft robotics, aerospace and biomedical devices, optics and surface morphing structures⁹⁻¹².

The use of topological defects in nematic LC to trap functional AuNRs and thus tune their plasmon resonance properties is simple yet versatile to apply LC defects as scaffolds for trap and actuate functional nanomaterials. We envision to extend this method to other

particle systems, e.g. quantum dots and dots-on-a-rod, which may lead to novel optical applications from LC lasers to solar cells. The sensitivity and tunability of such LC/nanoparticle systems in response to external stimuli, including heat, light and electric or magnetic fields, could promote the possible applications in LC sensors, detectors and metamaterials. We could also employ the folding and unfolding of LCEs to control the interaction of functional nanoparticles embedded in the LCE sheet within a fine distance in 3-D, thus reversibly tuning surface plasmonic resonance. The coupling of nanoparticles within a LCE network could potentially be exploited for “geometry-independent” epsilon-near-zero (ENZ) structures¹³ for a full duplex of robust electromagnetic functions. Further, as shown in our paper¹⁴ and Abott *et al.*¹⁵, topological defects created by LC assemblies can be “melted” and replaced with larger molecules such as AuNRs and amphiphiles, leading to formation of real functional objects.

The chemical patterning method we demonstrate in this thesis is simple yet highly effective and robust for generating LC phase gratings with embedded topological defects. The ability to precisely control LC anchoring and defect structures will offer great potentials to advance applications of LC optical and electronic devices, e.g. wide-viewing angle LCDs, diffractive and refractive optical lenses, spectral dispersion and imaging elements. Meanwhile, the trapping and assembly of colloidal particles by topological defects on the chemically patterned surfaces can be extended to the patterning of functional nanoparticles (e.g. AuNRs and quantum dots) for energy harvesting and novel display applications. Our technique of precisely patterning topological defects can be further applied to fabricate liquid crystal elastomers (LCEs) with complex LC director field of embedded topological defects, thereby allowing us to design sophisticated and

monolithic LCE actuation from *origami* folding to *Kirigami* shape transformation from 2D to 3D.

The role of surface chemistry in aligning LC homeotropical, planar or tilted configuration has been examined by several theoretical and experimental studies¹⁵. However, the generalized molecular level mechanism at various boundaries has yet to be well-understood. Surface energy that has been considered as one of the most important properties of the interface that determines the alignment of LC molecules¹⁶, still faces numerous exceptions, especially in the case of aligning LCMs^{8, 17}. The typically surface anchoring materials, such as polyimide, PVA, and DMOAP, which have been successful to align small molecule LCs, remains questionable to robustly align LCMs at the interface^{8, 17}. Though surface anchoring mechanism of small molecule LCs on different surface/interfaces has been investigated by light scattering and AFM scanning¹⁵, it remains unexploited for reactive LCMs, due to the fact that LCMs, owing to their polar reactive functional groups, have distinctive intermolecular interactions and behave differently with non-reactive LCs. To reveal the anchoring mechanism of LCMs, it requires characterization of the physical properties for LCM, including refractive index, dielectric constant, viscosity, elastic constants, surface anchoring coefficients, and Landau constants using techniques, such as light scattering, neutron scattering, and AFM scanning. We believe that these efforts can help us to determine the easy axis of the LCM orientation on a surface, to quantitatively measure surface anchoring energy, and to compute or simulate the molecular level interaction between the alignment layer and LCM. Thus, it will further enhance our understanding of the role of surface chemistry in LCM anchoring.

Meanwhile, while the role of surface topology in aligning LCs and creating topological defects has been well-understood^{2, 18-20}, a comprehensive description of the LC anchoring process on complex topographical surfaces remains challenging²¹. Though a large scope of patterned surfaces with various surface topographies has been prepared to investigate LC anchoring^{1, 15, 21-23}, many of these systems, especially surfaces with nano-scale topography, rely on theoretical interpretation of experimental observations extensively. A major challenge is to directly and precisely determine LC orientation at nanoscale. Therefore, development of a direct characterization technique for molecular level LC alignment is urgent. The technique of using stable nematic LCMs we describe in this thesis is one of the promising candidates; however, detailed measurement and determination of the basic properties of our LCMs will be required to establish quantitative models for their anchoring at topographical surfaces. It should be noted that LC anchoring model established from one molecule does not necessarily represent the anchoring of others, as LC anchoring varies with LC molecular structure, e.g. the anchoring strength and behaviors of 5CB and RM257 are different. This is because LC anchoring control is dependent on not only the properties of the anchoring surface, but also LC itself.

7.3 References

1. Cavallaro M, *et al.* (2013) Exploiting imperfections in the bulk to direct assembly of surface colloids. *Proc. Natl. Acad. Sci.* 110(47):18804-18808.
2. Muševič I, Škarabot M, Tkalec U, Ravnik M, & Žumer S (2006) Two-Dimensional Nematic Colloidal Crystals Self-Assembled by Topological Defects. *Science (New York, N.Y.)* 313(5789):954-958.
3. Rahimi M, *et al.* (2015) Nanoparticle self-assembly at the interface of liquid crystal

- droplets. *Proc. Natl. Acad. Sci.* 112(17):5297-5302.
4. Honglawan A, *et al.* (2015) Synergistic assembly of nanoparticles in smectic liquid crystals. *Soft Matter* 11(37):7367-7375.
 5. Rodarte AL, *et al.* (2015) Self-assembled nanoparticle micro-shells templated by liquid crystal sorting. *Soft Matter* 11(9):1701-1707.
 6. Milette J, *et al.* (2012) Reversible long-range patterning of gold nanoparticles by smectic liquid crystals. *Soft Matter* 8(24):6593-6598.
 7. Wang X, Miller DS, Bukusoglu E, de Pablo JJ, & Abbott NL (2016) Topological defects in liquid crystals as templates for molecular self-assembly. *Nat. Mater.* 15(1):106-112.
 8. Xia Y, Serra F, Kamien RD, Stebe KJ, & Yang S (2015) Direct mapping of local director field of nematic liquid crystals at the nanoscale. *Proc. Natl. Acad. Sci.* 112(50):15291-15296.
 9. Liu C, Qin H, & Mather PT (2007) Review of progress in shape-memory polymers. *J. Mater. Chem.* 17(16):1543-1558.
 10. de Haan LT, Schenning APHJ, & Broer DJ (2014) Programmed morphing of liquid crystal networks. *Polymer* 55(23):5885-5896.
 11. De Gennes P-G, Hébert M, & Kant R (1997) Artificial muscles based on nematic gels. *Macromol. Symp.* 113(1):39-49.
 12. White TJ & Broer DJ (2015) Programmable and adaptive mechanics with liquid crystal polymer networks and elastomers. *Nat. Mater.* 14(11):1087-1098.
 13. Silveirinha M & Engheta N (2006) Tunneling of Electromagnetic Energy through Subwavelength Channels and Bends using ϵ -Near-Zero Materials. *Phys. Rev. Lett.* 97(15):157403.
 14. Lee E, *et al.* (2016) Fine Golden Rings: Tunable Surface Plasmon Resonance From Assembled Nanorods in Topological Defects of Liquid Crystals. *Adv. Mater.* *accepted*.
 15. Wang X, Miller DS, Bukusoglu E, de Pablo JJ, & Abbott NL (2016) Topological defects in liquid crystals as templates for molecular self-assembly. *Nat. Mater.* 15(1):106-112.
 16. Theo Rasing IM (2004) *Surfaces and Interfaces of Liquid Crystals* (Springer, Berlin).
 17. Warenghem M (1982) A Test for Surface Energy Anisotropy Sign Determination. *Mol. Cryst. Liq. Cryst.* 89(1-4):15-21.
 18. Ohm C, Brehmer M, & Zentel R (2010) Liquid Crystalline Elastomers as Actuators and Sensors. *Adv. Mater.* 22(31):3366-3387.
 19. Lapointe CP, Mason TG, & Smalyukh II (2009) Shape-Controlled Colloidal Interactions in Nematic Liquid Crystals. *Science (New York, N.Y.)* 326(5956):1083-1086.
 20. Poulin P, Stark H, Lubensky TC, & Weitz DA (1997) Novel Colloidal Interactions in Anisotropic Fluids. *Science (New York, N.Y.)* 275(5307):1770-1773.
 21. Senyuk B, *et al.* (2013) Topological colloids. *Nature* 493(7431):200-205.
 22. Cattaneo L, Zhang J, Zuiddam M, Savoini M, & Rasing T (2014) Gaining Control through Frustration: Two-Fold Approach for Liquid Crystal Three-Dimensional Command Layers. *Nano Lett.* 14(7):3903-3907.
 23. Abbott NL (1997) Surface effects on orientation of liquid crystals. *Curr. Opin.*

Colloid Interface Sci. 2(1):76-82.

24. Jeong H-C, *et al.* (2015) Homogeneous self-aligned liquid crystals on wrinkled-wall poly(dimethylsiloxane) via localised ion-beam irradiation. *Sci. Rep.* 5:8641.

APPENDIX: List of Publications

1. **Xia, Y.**, Serra, F., Kamien, R.D., Stebe, K.J. and Yang, S., “Direct Mapping of Local Director Field of Nematic Liquid Crystals at the Nanoscale”, *Proc. Natl. Acad. Sci.*, 2015, **112**, 15291-15296.
2. Lee, E.[†], **Xia, Y.**[†], Ferrier, R.C. Jr.[†], Kim, H.-N., Gharbi, M.A., Stebe, K.J., Kamien, R.D., Composto, R.J., and Yang, S., “Fine Golden Rings: Tunable Surface Plasmon Resonance From Assembled Nanorods in Topological Defects of Liquid Crystals”, *accepted* (2016). ([†]Equal contribution)
3. **Xia, Y.**, Lee, E., Hu, H., Gharbi, M.A., Beller, D.A., Fleischmann, E.-K., Kamien, R.D., Zentel, R., and Yang, S., “Better Actuation Through Chemistry: Using Surface Coatings to Create Uniform Director Fields in Nematic Liquid Crystal Elastomers”, *submitted* (2015).
4. **Xia, Y.**, Cedillo, G., and Yang, S., “Pre-programmed Folding of a 2D Nematic Liquid Crystal Elastomer Sheet into 3D by Directing Liquid Crystal Alignment in 1D Micro-channels”, manuscript in preparation.
5. **Xia, Y.**, Kim, H.-N., Wu, G.X., Deshpande, S., and Yang, S., “Alignment of Nematic Liquid Crystals on Chemically Patterned Surfaces: Precise Design of Topological Defects”, manuscript in preparation.
6. Gharbi, M.A., Liu, I.B., Luo, Y., Serra, F., Bade, N.D., Kim, H.-N., **Xia, Y.**, Kamien, R.D., Yang, S., and Stebe, K.J., “Smectic Gardening on Curved Landscapes”, *Langmuir*, 2015, **31**, 11135-11142.
7. Cao, B., Wu, G.X., **Xia, Y.**, and Yang, S., “Buckling into single-handed chiral

- structures from pH-sensitive hydrogel membranes”, *Extreme Mechanics Letters* (2016), accepted. doi:10.1016/j.eml.2015.12.011
8. Wu, G. X., **Xia. Y.**, and Yang, S., “Buckling, symmetry breaking, and cavitation in periodically micro-structured hydrogel membranes”, *Soft Matter*, 2014, **10**, 1392-1399.